The Pennsylvania State University

The Graduate School

College of Engineering

OPTIMIZATION OF COMPOSITE TILTROTOR WINGS WITH

EXTENSIONS AND WINGLETS

A Dissertation in

Aerospace Engineering

by

Sandilya Kambampati

Submitted in Partial Fulfillment

of the Requirements

for the Degree of

Doctor of Philosophy

August 2016

The dissertation of Sandilya Kambampati was reviewed and approved* by the following:

Edward C. Smith
Professor of Aerospace Engineering
Dissertation Advisor, Chair of Committee

Mark. D. Maughmer
Professor of Aerospace Engineering

Jose Palacios
Assistant Professor of Aerospace Engineering

Christopher D. Rahn
Professor of Mechanical Engineering

George A. Lesieutre
Professor of Aerospace Engineering
Head of the Department of Aerospace Engineering

*Signatures are on file in the Graduate School.

Abstract

Tiltrotors suffer from an aeroelastic instability during forward flight called whirl flutter. Whirl flutter is caused by the whirling motion of the rotor, characterized by highly coupled wing-rotor-pylon modes of vibration. Whirl flutter is a major obstacle for tiltrotors in achieving high-speed flight. The conventional approach to assure adequate whirl flutter stability margins for tiltrotors is to design the wings with high torsional stiffness, typically using 23% thickness-to-chord ratio wings. However, the large aerodynamic drag associated with these high thickness-to-chord ratio wings decreases aerodynamic efficiency and increases fuel consumption. Wing-tip devices such as wing extensions and winglets have the potential to increase the whirl flutter characteristics and the aerodynamic efficiency of a tiltrotor. However, wing-tip devices can add more weight to the aircraft.

In this study, multi-objective parametric and optimization methodologies for tiltrotor aircraft with wing extensions and winglets are investigated. The objectives are to maximize aircraft aerodynamic efficiency while minimizing weight penalty due to extensions and winglets, subject to whirl flutter constraints. An aeroelastic model that predicts the whirl flutter speed and a wing structural model that computes strength and weight of a composite wing are developed. An existing aerodynamic model (that predicts the aerodynamic efficiency) is merged with the developed structural and aeroelastic models for the purpose of conducting parametric and optimization studies. The variables of interest are the wing thickness and structural properties, and extension and winglet planform variables. The Bell XV-15 tiltrotor aircraft the chosen as the parent aircraft for this study.

Parametric studies reveal that a wing extension of span 25% of the inboard wing increases the whirl flutter speed by 10% and also increases the aircraft aerodynamic efficiency by 8%. Structurally tapering the wing of a tiltrotor equipped with an extension and a winglet can increase the whirl flutter speed by 15% while reducing the wing weight by 7.5%.

The baseline design for the optimization is the optimized wing with no extension or winglet. The optimization studies reveal that the optimum design for a cruise

speed of 250 knots has an increased aerodynamic efficiency of 7% over the baseline design for only a weight penalty of 3% – thus a better transport range of 5.5% more than the baseline. The optimal design for a cruise speed of 300 knots has an increased aerodynamic efficiency of 5%, a weight penalty of 2.5%, and a better transport range of 3.5% more than the baseline.

Table of Contents

List of Figures

List of Tables

List of Symbols

A area, ft^2

a airfoil lift-curve slope $/rad$

c chord, ft

c_d drag coefficient

c_l lift coefficient

C_{M_x} yawing moment coefficient, $\frac{M_x}{\rho A(\Omega R)^2 R}$

C_{M_y} pitching moment coefficient, $\frac{M_y}{\rho A(\Omega R)^2 R}$

e chordwise distance from the aerodynamic center of the airfoil to the elastic axis, ft

EI bending stiffness, $lb - ft^2$

EI_b beamwise bending stiffness, $lb - ft^2$

EI_c chordwise bending stiffness, $lb - ft^2$

GJ torsional stiffness, $lb - ft^2$

H rotor axial force, lb

h mast height of rotor, ft

I_b rotor blade flap inertia, $slug - ft^2$

I_0 rotor speed perturbation inertia, $slug - ft^2$

I_β blade cyclic flap inertia, $slug - ft^2$

K_P rotor kinematic pitch-flap coupling

K_{bt} beamwise bending-torsion coupling, $EI_b - ft^2$

K_{ct} chordwise bending-torsion coupling, $EI_c - ft^2$

L lift, lb ; wing element length, ft

m elemental mass, $slug$

M Mach number; Bending moment, $lb - ft$

M_b blade mass, slug

M_b^* non-dimensional blade mass, $M_b^* = \frac{M_b R^2}{I_b}$

$M_{F_0}^*$ rotor collective moment in non-rotating frame, $lb - ft$

$M_{F_{1C}}^*$ rotor pitch moment in non-rotating frame, $lb - ft$

$M_{F_{1S}}^*$ rotor yaw moment in non-rotating frame, $lb - ft$

M_x rotor yaw moment, $lb - ft$

M_x rotor pitch moment, $lb - ft$

M_β rotor blade aerodynamic flap moment, $lb - ft^2$

Q rotor torque, $lb - ft$

R rotor radius, ft

r rotor blade radial coordinate, ft

S_α rotor pitch moment, $lb - ft$

T rotor thrust, lb

U resultant velocity, ft/sec

U_p perpendicular (axial) velocity, ft/sec

U_r radial velocity, ft/sec

U_t tangential velocity, ft/sec

V	freestream velocity, ft/sec
Y	rotor side force, lb
x	coordinate of the wing along the chord, in
y	coordinate of the wing along the perpendicular direction of x, in
α	angle of attack, rad
α_x	pylon yaw degree of freedom, rad
α_y	pylon pitch degree of freedom, rad
β_0	rotor coning angle, rad
β_p	rotor precone angle, rad
γ	Lock number
Λ	wing sweep angle, rad
μ	advance ratio
ν_β	rotor blade rotating natural frequency
θ_0	rotor blade root collective pitch angle, rad
ρ	freestream density, $slug/ft^3$
σ	stress, lb/in^2; blade geometric solidity
ω_θ	rotor blade torsion frequency, per rev
Ω	rotor rotation speed, rad/sec
ψ	azimuth angle, rad
ζ	rotor blade lag degree of freedom, rad; damping ratio
$\dot{(\,)}$	first derivative with respect to time
$\dot{(\,)}$	first derivative with respect to time
$\ddot{(\,)}$	second derivative with respect to time
$\overset{*}{(\,)}$	first derivative of with respect to azimuth, ψ
$\overset{**}{(\,)}$	second derivative with respect to azimuth, ψ

Acknowledgments

I would like to sincerely thank Dr. Ed Smith for the support and guidance I received over the past three years. Thanks are also due to the members of my doctoral committee: Dr. Rahn, Dr. Palacios, and Dr. Maughmer, for the time they spent reviewing my research and for their helpful comments.

I must acknowledge my fellow Penn State Rotorcraft Center and Aerospace Engineering graduate students for all the help I received over the years.

Finally, I would like to thank Mr. Wally Acree at NASA Ames for the technical discussions and for carefully reviewing my research.

Chapter 1

Introduction

Tiltrotor aircraft are a class of compound helicopters which have the hovering capabilities of a helicopter, and the speed and range of a fixed-wing aircraft. The aircraft is characterized by rotors mounted at the wing-tips which can be tilted by 90 degrees for conversion from hovering flight to forward flight. The Bell XV-15, the Bell/Boeing V-22, and the Agusta Westland AW-609 (Fig. 1.1, from Refs. 1 and 2) are examples of successful manned tiltrotor aircraft. Nearly sixty years of development and extensive research efforts have established the feasibility of different tiltrotor configurations for meeting civil and military requirements.

Tiltrotors suffer from an aeroelastic instability called whirl flutter. Whirl flutter is an instability caused by the whirling motion of the rotor, characterized by highly coupled wing-rotor-pylon modes of vibration. The damping ratios of the coupled vibration modes are dependent on forward speed. At high speeds, the damping ratios can become negative due to destabilizing aerodynamic forces on the rotor - leading to a catastrophe. Therefore, whirl flutter is a major obstacle for tiltrotors in achieving high-speed flight.

One approach to assure adequate whirl flutter stability margins for tiltrotors is to design the wings with high torsional stiffness [3]. The high torsional stiffness requirement leads to thick wing sections – the XV-15 and the V-22 are designed with 23% thickness-to-chord ratio wings [4, 5]. The large aerodynamic drag associated with these high thickness-to-chord ratio wings decreases the aerodynamic efficiency and increases fuel consumption.

The aerodynamic efficiency of tiltrotors can be increased by the use of wing-tip devices such as wing extensions and winglets [6]. Wing-tip devices also have the potential to increase the whirl flutter characteristics of a tiltrotor [7]. However,

(a) Bell/Boeing V-22

(b) AW 609

(c) Bell XV-15

Figure 1.1: Examples of successful manned tiltrotor aircraft (from Refs. 1 and 2).

wing-tip devices redistribute the aerodynamic loads on the wing, increase the bending moment at the root, eventually increasing the wing weight [8]. Therefore, the pros and cons associated with wing-tip devices motivates an optimization study aimed at increasing the aerodynamic efficiency and reducing the wing weight, while keeping the whirl flutter stability in check.

This chapter discusses an overview of the literature on analytical and experimental research on whirl flutter and tiltrotor wing design. The overview includes survey on the effects of winglets on aerodynamics and aeroelastic stability of tiltrotors. The literature on various structural and aerodynamic optimization studies are also presented. This chapter concludes with the objectives of this dissertation.

1.1 Initial Efforts to Understand Whirl Flutter

Whirl flutter was first identified by Taylor and Browne [9] as a possible instability involving the yawing and pitching motion of a propeller-nacelle combination. The nacelle pitching motions in high-speed flight produce aerodynamic yawing moments, while the nacelle yawing motions produce aerodynamic pitching moments. These aerodynamic moments, at certain frequencies, may result in an unstable whirling motion opposite to the direction of propeller. Whirl flutter first occurred in 1959 – breaking up a turboprop powered Lockheed Electra aircraft (Fig. 1.2) in mid-air. Thorough analytical investigation and studies at NASA Langley Research Center confirmed that whirl flutter was the reason for the catastrophe [10]. This incident with the Electra sparked further research to understand whirl flutter.

Houbolt and Reed at the NASA Langley Research Center isolated the parameters that were strongly linked with whirl flutter [11]. The pylon pitch and yaw stiffness, and damping were found to be the important parameters. By independently varying stiffness in pitch and yaw direction, the divergence and flutter boundaries were plotted. The role of gyroscopic coupling which affects the overall stiffness of the system was explained. The results showed that when stiffness in pitch and yaw were unequal, then it was beneficial to have greater damping in the direction of minimum stiffness. A few of these results were validated with wind tunnel tests on a model consisting of a windmilling propeller attached to a rod that had pitch and yaw degrees of freedom.

Figure 1.2: Lockheed Electra turboprop airliner (from Ref. 1).

Figure 1.3: The Bell XV-3 (from Ref. 1).

The Bell XV-3 tiltrotor research aircraft (Fig. 1.3) was the first tiltrotor to have experienced whirl flutter problems – resulting in a crash that injured the pilot. The XV-3 was redesigned with a new 2-bladed stiff in-plane teetering rotor system along with external struts to stiffen the wings. The changes helped the XV-3 perform first full conversion from hover to airplane mode. However, the airplane mode flight tests revealed that there were problems with transient blade flapping.

The XV-3 was then tested in the 40-by-80 foot wind tunnel at NASA Ames Research Center to investigate the effects of the kinematic pitch-flap coupling parameter, δ_3, on transient flapping response. δ_3 is the angle between the line joining the pitch horn and the hub, and the line joining the pitch bearing and the hub (Fig. 1.4). δ_3 kinematically couples the flapping and pitching motion of the blade. During this course of testing, a rotor/pylon instability similar to the propeller/nacelle whirl flutter, where the rotor and pylon were precessing in the opposite direction of the rotor rotation, was observed. This experimental data provided researchers valuable information to gain understanding of the fundamentals of whirl flutter, and to develop rotor/pylon stability analyses.

A four degree of freedom (DOF) model consisting of pylon pitch and yaw, and rotor lateral and longitudinal flapping was developed by Hall [13]. Hall, with the help of this 4DOF model, showed that the principal destabilizing forces were the in-plane rotor forces generated due to the gyroscopic precession of the rotor. Edenborough [14] extended the 4DOF model by including the vertical displacement of the pylon, which was driven by the wing vertical bending displacement. The analysis, followed by experimental results, showed that increasing the flapping

4
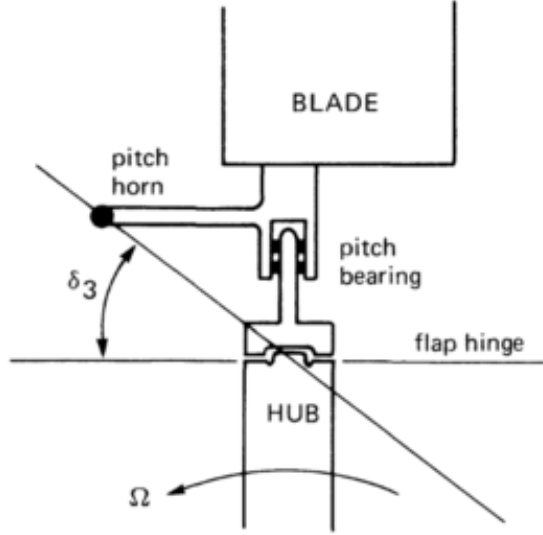
Figure 1.4: A schematic of the kinematic pitch-flap coupling parameter, δ_3 (from Ref. 12).

restraint and δ_3 was stabilizing to whirl flutter. Gaffey [15] investigated the effects of δ_3 on flapping stability and whirl flutter. The XV-3 was designed with a positive δ_3 (flap-up pitch-down coupling), to reduce the transient flapping response. Gaffey showed that a positive δ_3 ultimately lead to a flap-lag instability. Negative δ_3, on the other hand, also decreased the flapping response for teetering rotors such as the XV-3 rotor, and eliminated the flap-lag instability.

The experience gained from the design of the XV-3 motivated NASA to award new contracts to Bell and Boeing to develop a new tiltrotor research aircraft. The Bell design (Bell Model 301) featured a stiff in-plane gimballed hub, while the Boeing design (Boeing Model 222) featured a hingeless soft in-plane design. Full scale tests were conducted on these rotors in the NASA Ames 40-by-80 foot wind tunnel (Fig. 1.5). These tests provided substantial data on performance, loads, and vibration as well as the aeroelastic stability. The Bell Model 301 was selected by NASA and got subsequently designated as Bell XV-15 [16].

Johnson established a method to predict the dynamic behavior of a tiltrotor in forward flight [17]. The results of this method were validated using the wind tunnel tests at NASA Ames. The analysis started with a 6DOF model for a three bladed rotor with a flap and a lag DOF each for the blades. A 3DOF model for a cantilever wing was developed and was coupled to the 6DOF model for the rotor, resulting

(a) Bell Model 301 rotor.   (b) Boeing Model 22 rotor.
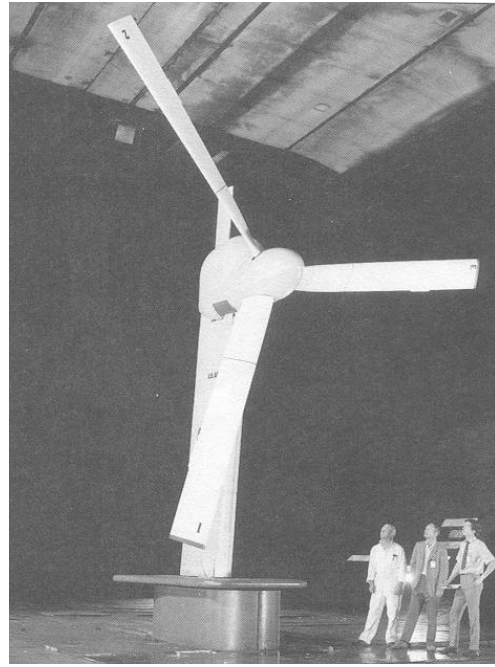
Figure 1.5: The Bell 301 and Boeing Model 301 rotors in the Ames 40-by-80-ft wind tunnel (from Ref. 16).

in a 9DOF model. This analysis was extended by including coupled flap, lag, and torsion degrees of freedom for the rotor. The influence of the blade rigid pitch and elastic torsion degrees of freedom on whirl flutter was thoroughly examined by Johnson in Ref. 18. The rigid pitch motion blade, arising due to a non-rigid control system, when combined with the precone angle, introduced an effective pitch-flap coupling in the model. This pitch-flap coupling was destabilizing to whirl flutter. The analysis developed in these models formed the basis for the tiltrotor modeling in CAMRAD [19], a comprehensive rotorcraft analysis code developed by Johnson.

1.2 Parametric Studies on Whirl Flutter

The research described in the previous section was focused on understanding the physics behind whirl flutter. This section summarizes the various parametric studies conducted on whirl flutter.

1.2.1 Analytical Studies

The key design parameters that influence whirl flutter stability were identified by Nixon [20]. It was shown that an improved stability boundary can be obtained by setting the rotor flap and lag frequencies to an optimum value. It was also shown that these stability improvements arise due to the coalescence of certain rotor frequencies with wing frequencies. The parametric study on the wing frequencies showed that the flutter speed was more dependent on the placement of the wing frequencies relative to each other than the placement of the wing frequencies relative to rotor frequencies. Specifically, the frequency separation between the beam and torsion frequencies had a greater importance on the flutter stability.

Nixon [20] showed that wing sweep introduced additional coupling between the beam and torsion modes of the wing. This coupling increased the required frequency separation between the wing beam and torsion modes. A parametric study of wing sweep on whirl flutter for the XV-15 is shown in Fig. 1.6, where the non-dimensional whirl flutter speed ($V_F^* = V_F/V_T$, V_F is the whirl flutter speed and V_T is the rotor blade tip speed) is plotted against wing sweep angle. The stability boundary of the beam and the chord modes reduced with increasing the sweep angle. The stability boundary of the torsion mode decreased for small sweep angles and increased for larger sweep angles.
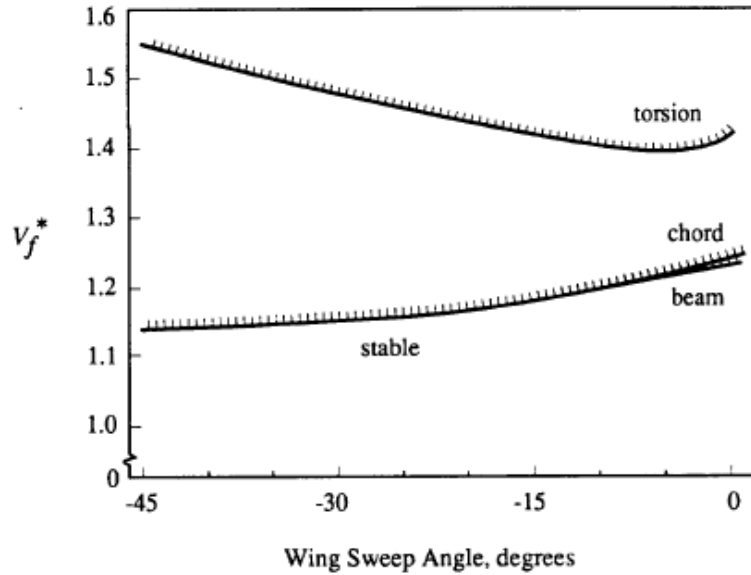
Figure 1.6: Parametric study of wing sweep for the XV-15 (from Ref. 20).
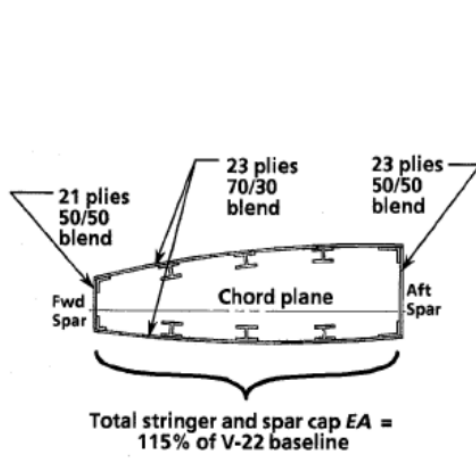
(a) Schematic of the 18% wing torque box.
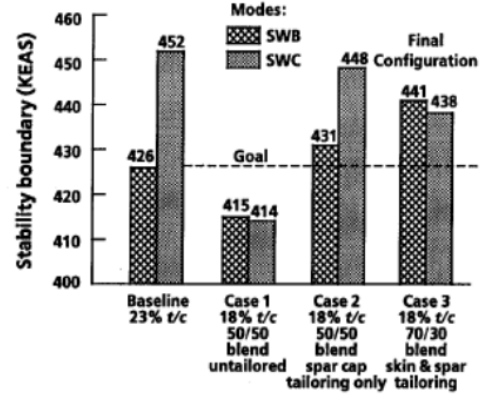
(b) Results showing the 70/30 blend ratio maximizing beam mode stability (SWB) and 50/50 blend ratio maximizing chord mode stability (SWC).

Figure 1.7: Results from a composite tailoring study on the V-22 wing (from Ref. 5).

A parametric study of wing thickness and composite tailoring on the whirl-flutter stability boundary of the V-22 tiltrotor was presented by Popelka et al. in Ref. 5. The thin wing had a thickness of 18% while the baseline V-22 had a 23% thick wing (Fig. 1.7a). Reducing the stiffness of the wing to 18% decreased the airframe drag by 10%, but it also decreased the stability boundary by 38 knots due to loss in stiffness. This stability boundary could be recovered by adding more stiffness at the cost of increasing the wing weight. This additional weight penalty could be avoided by using composite tailoring. The laminate blend ratio, defined as the ratio between the number of -45 degree plies to the number of +45 degree plies, was the key parameter that introduces bending/torsion coupling in the wing. It was found that a blend ratio of 70/30 maximized the beam mode stability, while a 50/50 blend ratio maximized the chord mode stability (Fig. 1.7b).

The authors of Ref. 5 also investigated the effects of stringer and spar cap areas. The loss in stiffness due to composite tailoring of the skin could be regained by redistributing the spar cap area directly to the spars with no net increase in weight. It was shown that the chord mode stability boundary increases by 6 knots for redistributing a 50% spar cap area to the spar. The final results showed that the 18% thick wing, which was tailored using composites and had a redistributed spar cap and spar area, was 1.2% heavier but had a stability boundary of 12 knots than the baseline 23% wing.

Parametric studies on rotor design to improve whirl flutter stability margins were explored in Ref. 4. Although the study was related to changes in the rotor, a thin composite wing representative of a high speed tiltrotor was also investigated. The thin wing offered a better aerodynamic performance, but it also had a lower stiffness, which reduced the whirl flutter stability. The wing was assumed to have the same geometry as the XV-15, except that the thickness was reduced from 23% to 15%. The weight distribution of the 23% and 15% wings is tabulated in Table 1.1. The torque box was assumed to be the primary load carrying structure, and was made of T300/5208 graphite-epoxy material. The ply angles were assumed to be combinations of 0,$\pm$45,90 degree plies. The wing structure was sized based on strength to meet 2-g jump take off and 4-g symmetric pull-up loads. The whirl flutter speed of the thick wing was 330 knots and weighed 946 lbs. The whirl flutter speed of the thin wing was 275 knots, and it weighed 579 lbs. The thin wing was redesigned by adding more plies to match the flutter speed of the thick wing, which was 330 knots, but it weighed 1062 lbs, which is 12% heavier than the thick wing.

Table 1.1: Wing structural weight (lbs) comparison between XV-15 wing and a the conceptual 15% t/c wing used in Ref. 4.

	XV-15 wing (23% t/c)	Conceptual wing (15% t/c)
Torque box	567	260
Spars	52	34
Control surfaces	97	77
Fairings	108	86
Fittings other	122	122
Total wing	946	579

1.2.2 Wind-Tunnel Studies

The analytical studies on wing thickness and composite tailoring presented by Popelka et al. in Ref. 5 were tested experimentally in Ref. 21. A 1/5-size Froude-scaled aeroelastic model of the V-22 (Fig. 1.8a) was tested using the Wing and Rotor Aeroelastic Test System (WRATS) as the test bed. The first test of the

(a) A 1/5-size Froude-scaled model of the V-22.

(b) The 23% and the 18% wing cross sections.
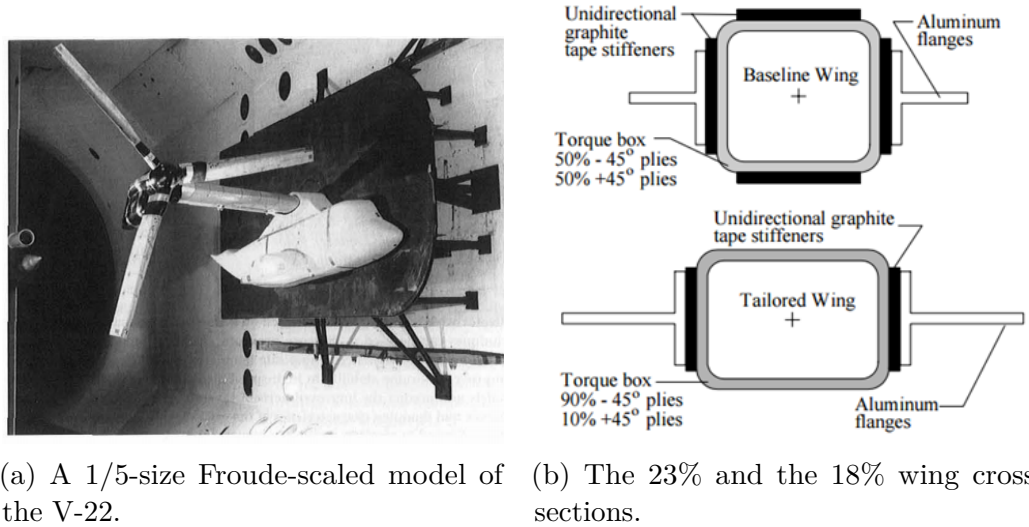
Figure 1.8: Results from a composite tailoring study by Corso et al. [21].

WRATS model established baseline aeroelastic stability boundaries for a tiltrotor with an untailored and 23% thick wing. The next test was to measure the aeroelastic stability of an 18% thick composite tailored wing. The 23% and the 18% wings were designed around a central spar which acted as the primary load carrying member (Fig. 1.8b). Additional aluminum T-section flanges provided additional chordwise stiffness to the desired target values. The baseline wing spar had ±45 degree plies forming a composite box beam with a constant rectangular cross section. The tailored wing spar, on the other hand, had 90% -45 degree plies and 10% 45 degree plies.

The bending mode stability correlation plot for the 1/5-scale tailored wing is shown in Fig. 1.9a. An agreement between the predictions and the experiments was achieved for the 1/5-scale tailored wing. The stability boundary of the 23% wing (baseline) and the tailored 18% wing for different rotor speeds is shown in Fig. 1.9b. The tailored wing had a stability boundary greater than the baseline wing by approximately 30 knots for the all the rotor speeds considered in Ref. 21.

An experimental parametric investigation of the wind tunnel stability boundaries of a 0.2-scaled semi-span tiltrotor was studied by Piatak et. al. [22]. The parameters of interest were mainly rotor design variables such as control system stiffness, offset coning hinge hub, pitch-flap coupling, and compressibility effects. A downstop spring is used to simulate the stiffness of the pylon conversion actuator in the locked and

(a) Bending mode stability correlation for the 1/5-scale tailored wing .

(b) Stability boundary of the baseline and tailored wings
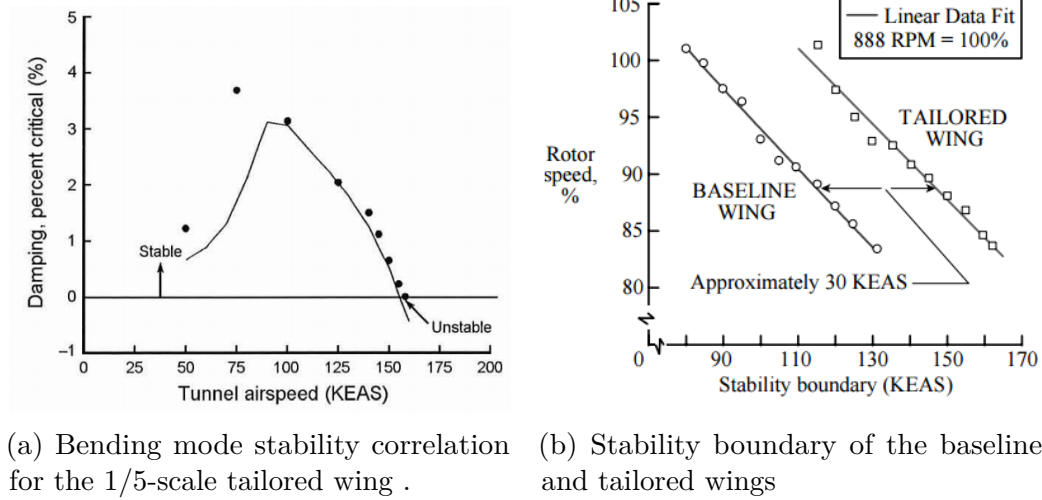
Figure 1.9: Results from a composite tailoring study by Corso et al. [21].

unlocked configurations, which are referred to as the on-downstop and off-downstop configurations, respectively. The baseline wing did not have any bending-torsion couplings. This model was found to have a beam mode instability at 88 knots for 888 RPM, and 142 knots at 742 RPM for the off-downstop configuration. For the on-downstop configuration, the beam mode instability occurred at 155 knots for 888 RPM and 187 knots for 777 RPM. The on-downstop configuration represented a much stiffer pylon compared to the on-downstop configuration. This resulted in an increased separation between the wing beam and torsion frequencies for the on-downstop configuration, and hence the increase in the stability boundary. The chord mode remained stable in the test regime for both 742 RPM and 888 RPM. The effects of compressibility was investigated by using a heavy gas medium in the wind tunnel. The airfoil lift curve slope increased with mach number, resulting in higher aerodynamic forces, which had a destabilizing effect on whirl flutter. The stability boundary in the heavy gas was found to be 12 knots and 25 knots lower than the stability boundary in air, respectively, for 770 RPM and 888 RPM. The effects of the pitch-flap coupling, via δ_3, on a flexured-hub were also investigated in Ref 22. The results confirmed the destabilizing nature of the pitch-flap coupling. However, when compared to the rigid hub, the destabilizing nature of the pitch-flap coupling was reduced due to the flexured-hub.

The experimental results also showed that the control system flexibility does not have a significant impact on the wing beam mode damping, for both on-downstop

and off-downstop configurations. These results were contrary to the previous studies reported by Johnson in Ref. 18.

Wind-Tunnel studies of a four-bladed semi-articulated soft-in-plane rotor system (SASIP) on WRATS were presented by Nixon et al. in Ref. 23. Several experiments were conducted on SASIP including the effects of pitch-flap coupling, pitch-lag coupling, and drive-train dynamics on whirl flutter. The results were compared to the three-bladed WRATS tiltrotor model (the 1/5-size Froude-scaled aeroelastic model of the V-22 discussed in Ref. 21). To investigate the effects of drive-train dynamics, experiments were conducted for two operating rotor modes - the windmilling mode where the rotor is unpowered and disconnected from the drive train, and the powered mode where the rotor is connected to the drive train. The results showed that the damping of the beam mode of the stiff-inplane rotor system was significantly increased for the powered case (Fig. 1.10a). For the soft-inplane rotor system, both the stability boundary and the damping of the beam mode increased significantly for the powered case (Fig. 1.10b). The results in Fig. 1.11 show that the drive train provides additional damping to the the beam-mode stability .

Wind tunnel test results for a 0.2 scaled stiff in-plane tiltrotor model were presented in Ref. 24. Previous analyses showed that a pitch-flap coupling of -15 degrees was a good balance of whirl flutter stability, blade flap-lag stability, and

(a) Stiff-inplane rotor system.   (b) Soft-inplane rotor system
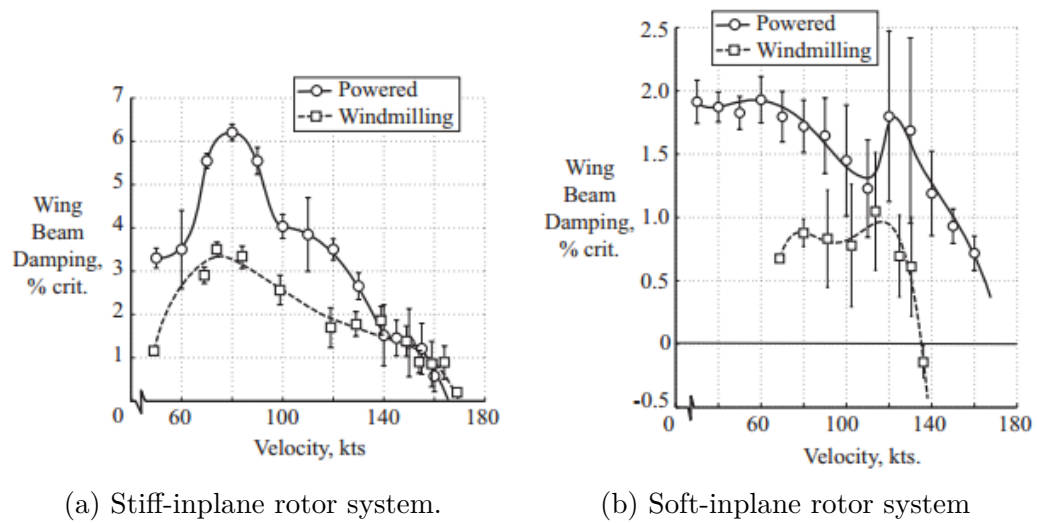
Figure 1.10: Comparison of wing beam mode damping between the windmilling and powered conditions (from Ref. 23).

12

(a) Conventional control layout would result in an interference between the pitch horn and the adjacent blade.

(b) Components of the 4-bladed stepover control mechanism
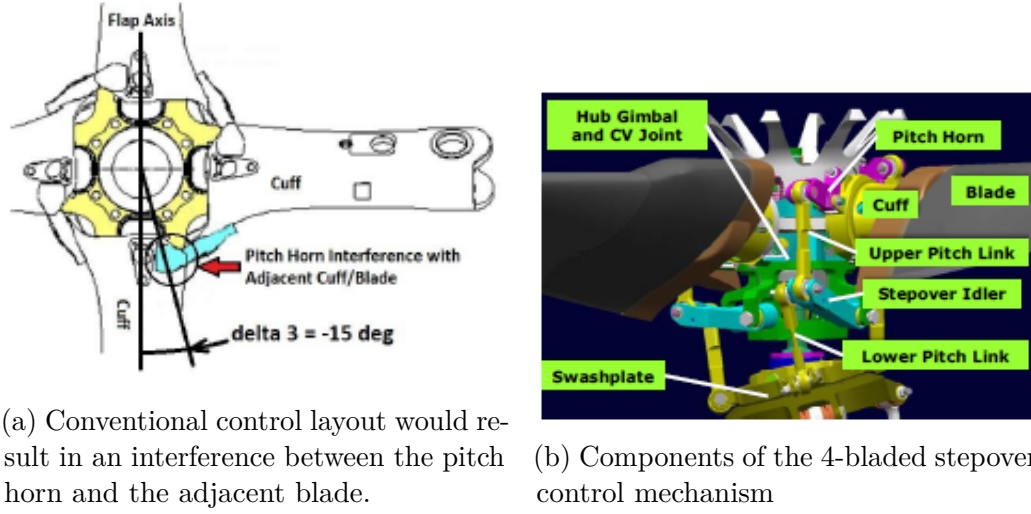
Figure 1.11: Schematics of the conventional and the stepover control layouts (from Ref. 24).

rotor flapping reduction. The geometric space required to achieve this pitch-flap coupling was easily available in a 3-bladed rotor. However, for a 4-bladed rotor, a conventional control layout cannot provide a δ_3 angle of greater than -40 degrees. A -15-degree δ_3 angle would result in an interference between the pitch horn and the adjacent blade (Fig. 1.11a). To overcome this problem, a novel stepover control mechanism was used to achieve the required pitch-flap coupling of -15 degrees within the restricted space (Fig. 1.11b). We can see from Fig. 1.11b that stepover idler, helps the upper pitch link to avoid interference with the adjacent blade. The results of this study showed that the stepover mechanism provided more stability to the 4-bladed rotor. The results also showed that, for the 4-bladed rotor, the stepover configuration ($\delta_3 = -15$ degrees) was stable for speeds up to 200 knots, while the conventions configuration ($\delta_3 = -40$ degrees) was unstable at 133 knots.

1.3 Aerodynamic and Aeroelastic Effects of Wing-Tip Devices

Wing-tip devices such as wing extension and winglets (Fig. 1.12) are often used in fixed-wing aircraft to reduce induced-drag and to increase fuel efficiency [26]. Modern tiltrotor wing designs use wing extensions to reduce the induced drag
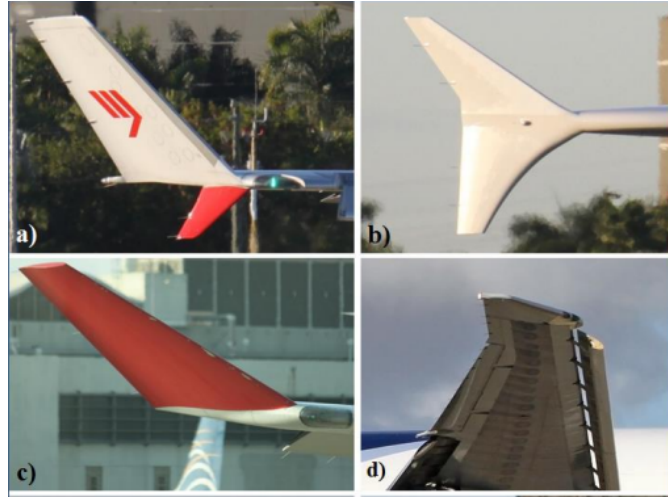
Figure 1.12: Different types of winglets on different fixed-wing aircraft a) Whitcomb Winglet (McDonnellDouglas MD-11), b) Wingtip Fence (Airbus A380), c) Canted Winglet (Airbus A330), d) Raked Wingtip (Boeing 777F)(from Ref. 25).

on the aircraft (Large Civil Tiltrotor 2 [27]). Cole et al. [6] showed that wing extensions and winglets can potentially reduce the induced drag on tiltrotor wings, as they operate at relatively high lift coefficients.

Winglets have a negative impact structurally on fixed-wing aircraft since they increase the bending moment at the root, leading to the need of reinforcements which also add weight. Another setback is the reduction in dynamic stability of the wing. Experimental results showed that the addition of a winglet reduced the wing-flutter dynamic pressure by 12 percent [28]. This reduction in flutter speed was primarily due to the aerodynamic forces on the winglet rather than the winglet interference effects on the wing or winglet mass. It was also noted that for some cases, the chordwise bending mode, which was usually stable and decoupled from bending and torsion modes, had significant bending-torsion components and was the critical mode [29].

In another study presented in Ref. 30, flutter tests were conducted experimentally at Mach numbers from 0.6 to 0.95, on models with a wing-tip, a tip with a winglet, and a normal-shaped ballast to simulate the winglet mass properties. The results showed that the addition of the winglet and tip ballast reduced the wing flutter speed by 7% and 5%, respectively. Hence, they concluded that the winglet effect on flutter was equally a mass effect as well as an aerodynamic effect. The results showed that the effect of winglet stiffness on flutter speed was negligible, and the

aerodynamic and inertial effects were major contributors to flutter. For subsonic inflow, the winglet addition resulted in a degradation of flutter characteristics, and the winglet aerodynamics was the major contributor, and the flutter speed reduced by about 15 percent.

The multi-fidelity design of an aeroelastic wing-tip was discussed in Ref. 31, where the extension was aeroelastically tailored to alleviate the extra load. The structure of the device was made sufficiently flexible for a favorable lift distribution that could reduce structural loads. Two designs of the wing-tip were proposed. The wing-tip was attached to the wing by a flexible torque tube and its torsional stiffness was tuned to provide a nose down deflection of the extension, thus shifting the aerodynamic load towards the root in the first design. Such devices were proposed by Miller [32] (Fig. 1.13), and its effectiveness was confirmed by numerical simulations as well as experiments. However, for low values of this torsional stiffness, the extension introduced unstable modes at low speed by combining with wing bending and torsion modes in low flight. An optimization was also performed to reduce the mass of the extension and the design variables were the bending and torsional stiffness of the attachment, while imposing a constraint on the flutter speed. The second design design used composite materials, where bending and torsion modes were structurally coupled.
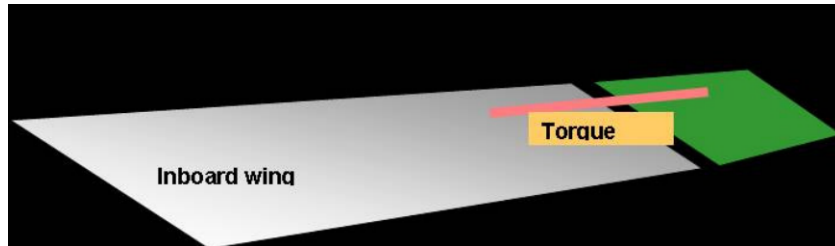
Figure 1.13: Load alleviation device proposed by Miller [32].

1.4 Optimization Studies on Tiltrotors

A survey of the literature reveals several optimization studies on tiltrotors aimed at improving the aeroelastic stability and aerodynamic efficiency, while reducing the weight of the tiltrotor.

1.4.1 Aeroelastic Optimization

Active and passive methods of optimization to improve the whirl flutter speed of tiltrotors were explored by Hathaway in Ref. 1. A whirl flutter model which used a basic rigid blade model for the rotor was developed. Such basic models can be useful in optimization studies as they were computationally cheap. Passive optimization studies revealed that when only minor changes were allowed on the design variables, the pitch-flap and pitch-lag coupling parameters were the key parameters in increasing the stability of the aircraft. If large changes in the design variables were permitted, the destabilizing effects of δ_3 can be reversed by adjusting other rotor parameters, and this gave the designer flexibility to select δ_3 that satisfies other design requirements. The wing parameters which had the greatest influence in the optimum design were vertical bending and torsional stiffness. They influence the nacelle plunging and pitching motions and were often the critical modes of flutter in tiltrotors. The damping of the baseline design and the damping of the optimized design is shown in Fig. 1.14. In the baseline design (Fig. 1.17a) beam mode (labeled b) is stable for speeds up to 310 knots and the chord mode is stable for speeds up to 350 knots. In the optimized design (Fig. 1.17b), both the beam and chord modes are stable for speeds up to 450 knots. The optimization study, thus, yielded a 130 knot increase in flutter speed.

(a) Damping of baseline design.   (b) Damping of optimized design.
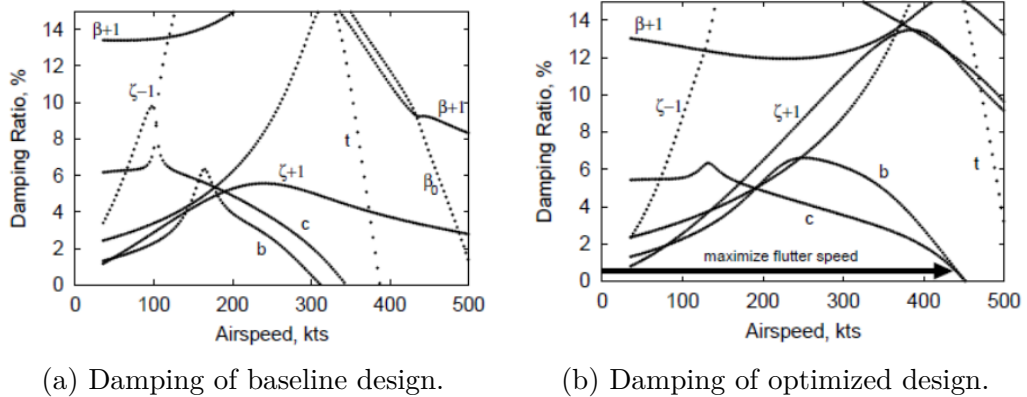
Figure 1.14: Optimization results presented by Hathaway [1].

The influence of rotor and wing parameters on the whirl flutter stability of a soft in-plane tiltrotor was investigated by Paik in Ref. 33. Soft in-plane tiltrotors were generally characterized with low damping in the wing vertical bending mode. Formal

gradient based optimization algorithms were used to identify the combinations of the rotor and wing parameters that would maximize the flutter speed. Results showed that a concurrent optimization of rotor/wing design variables increased the flutter speed from 390 to 425 knots and also improved the sub-critical beam mode damping significantly, relative to the baseline configuration.

The investigation of the design and optimization of a thin composite wing box structure for a tilt-rotor aircraft was presented by Clements and Rais-Rohani in Ref. 34. The study was focused on the structural design, and hence the wing shape and rotor pylon system were held fixed. The airfoil section was an 18% thick scaled down version of the V-22 airfoil. The optimization problem was formulated as a wing weight minimization problem subject to strength, stiffness and dynamic constraints. The design variables were sizing parameters of the composite skin plies, stringers, spars, and ribs. A global-local procedure was used in this study. First, the global model of the wing was optimized based on strength and dynamic constraints. The local methods involved examining the skin panels and spar webs for local failure (buckling) using a panel failure code. If the local method predicts failure, then the thickness of the panel was optimized locally for minimum weight subject to the failure criterion. This optimal thickness was used in the global method for any constraint violation. If a particular constraint was violated, the iteration was repeated until the constraints were satisfied. The placement of the wing natural frequencies were used as dynamic constraints. The wing beamwise bending frequency must be less than 80% of the wing chordwise bending frequency. The wing chordwise bending frequency must be approximately 0.85/rev. The wing torsion frequency must be at least 1.15/rev. The lower bound on the bending frequency was the active constraint in this study. Thus, the wing stiffness required to avoid whirl flutter was higher than the stiffness required to avoid 2-g failure loads. The optimization scheme converged to a minimum weight in 23 iterations (Fig. 1.15).

1.4.2 Aerodynamic Optimization

Performance optimization of a tiltrotor with composite blades was reported by Soykasap and Hodges in Ref. 35. Since the difference in hover and forward-flight modes of tiltrotors caused a change in the blade centrifugal force, the extension-
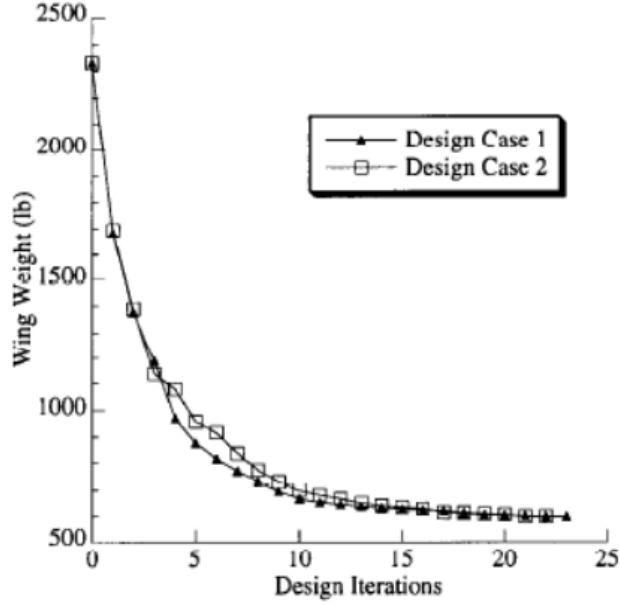
Figure 1.15: Optimization converges after 23 iterations for the two design cases considered (from Ref. 34).

twist structural coupling could be optimized for better performance. The study revealed that built-in twist and extension-twist coupling played a key role in the optimum design. The results showed significant improvements in performance when optimizing only extension-twist coupling. Previous studies (Ref. 20) showed that the amount of twist deformation caused by the coupling could be increased by the addition of a tip-mass, but it was detrimental to whirl flutter. The study showed that the required twist can be optimized by choosing the appropriate lay-up without the addition of a tip mass.

An inverse method for optimization of tiltrotor rotor blades was developed in Ref. 36. In this method, the rotor blade stiffness distributions were treated as design variables. The objective function used was maximizing the axial efficiency and figure of merit in hover with equal weighting ratios. Constraints were placed on the positive definiteness of the stiffness matrix, non-rotating natural frequencies of the blade, and material failure. Subsequently, geometric properties of the cross-section and ply orientation angles were determined which can produce the optimum stiffness.

A passive optimization study of extension-twist coupling in tiltrotor rotor blades was presented in Ref. 37. The blade control design referred to as The Sliding

Mass Concept (SMC), was developed for performance improvement. The SMC concept took advantage of non-structural masses in the blade, such as the leading edge balancing mass, and allowed it to slide with respect to the blade frame, thus having the control to change the centrifugal force, and hence the blade twist, when required.

Performance optimization and analysis on a Large Civil Tiltrotor 2 (LCTR2) (Fig. 1.16) was presented by Acree et al. in Ref. 38, Ref. 39, and Ref. 27. Rotor blade twist, taper, and solidity optimizations including rotor/wing interference calculations were presented in Ref. 38. Hover/cruise performance trade-offs for different cruise tip speeds were also analyzed in Ref. 38. In Ref. 39, this optimization was extended to vehicle sizing. The optimization was performed by making use of a coupled design process of the LCTR2, where the rotor/wing interference was included explicitly in the aeromechanics analysis. Four different designs of the LCTR2 including practical considerations with tilting/non-tilting nacelles, with and without extensions, were presented in Ref. 27. The study showed that an extension improves the L/D by 6%. However, the wing weight had to be increased by 21% to handle the extension loads.
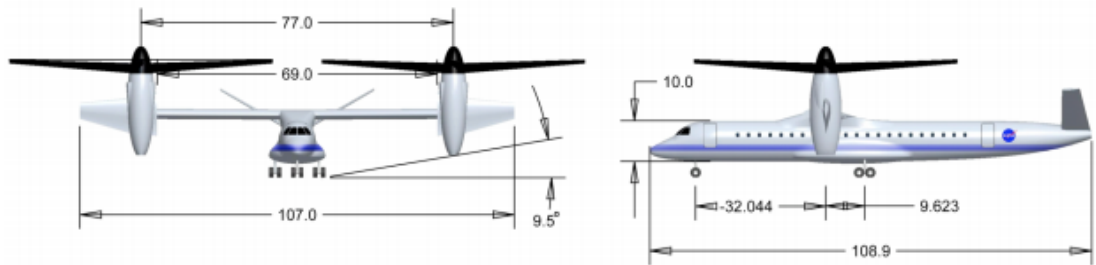
Figure 1.16: Schematic of the LCTR2 (dimensions in feet, from Ref. 27).

1.4.3 Multidisciplinary Optimization

A multidisciplinary optimization procedure was developed in Ref. 40 to investigate the trade-offs associated with the performance of a high speed tiltrotor aircraft. The objectives considered were to maximize the hover figure of merit and cruise propulsive efficiency in forward flight while minimizing wing weight. The design variables were the rotor and wing planform variables, and the wall thicknesses in the wing. Constraints were placed on natural frequencies on rotor and wing,

autorotational inertia and weight of the rotor, and whirl flutter speed of the tiltrotor. The rotor analysis was performed using CAMRAD, which calculates the loads using the blade element approach. The wing was modeled as a cantilevered box-beam with a rectangular cross-section with tip masses. The dynamic analysis was performed for the wing using a finite element analysis, and the mode-shapes and frequencies were used as inputs to CAMRAD. A lifting line theory based on quasi-steady aerodynamic assumptions was used to calculate the loads and perturbation forces on the wing. The optimum design had an increased hover figure of merit by about 2.3 percent, while having a reduced weight of about 10 percent compared to the baseline configuration (Fig. 1.17).

Multidisciplinary optimization can be computationally intensive especially in aircraft design where the design variables are usually large. Multi-level decomposition methods, where the multi-objective problem is divided into sub-problems, are used to reduce the computational effort involved. Such multi-level decomposition based optimization procedure was developed by Chattopadhyay and McCarthy in Ref. 41 for aerodynamic and structural design of tiltrotors. The design space was not continuous, and hence a simulated annealing based technique was used for optimization. The figure of merit was increased by 6.6 percent and the cruise propulsive efficiency was increased by 3.2 percent compared to the baseline rotor. The optimum wall ply-orientation angles were ±30degree plies, which represent a

(a) Aerodynamic variables.   (b) Weight distribution.
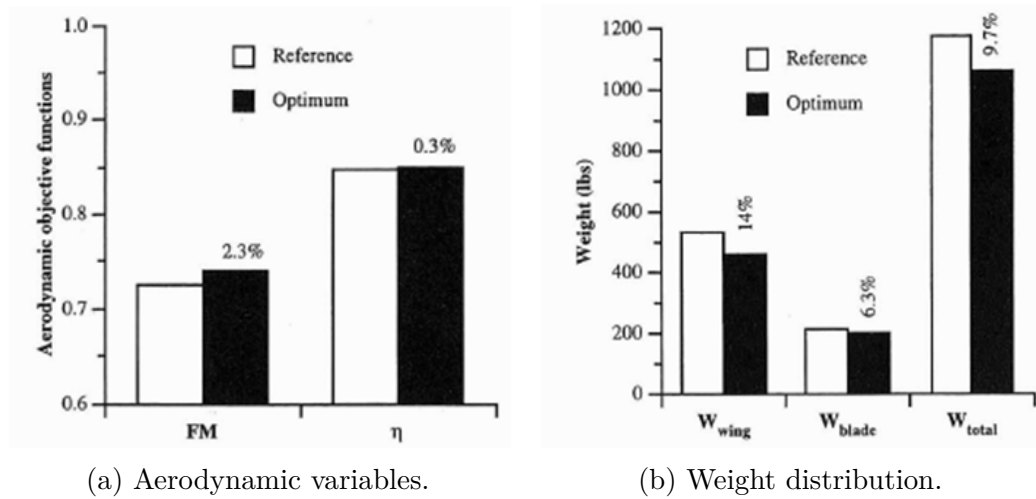
Figure 1.17: Reference and optimized hover efficiency (FM), cruise efficiency (η), and weight (from Ref. 40).

compromise between elastic twist and bending.
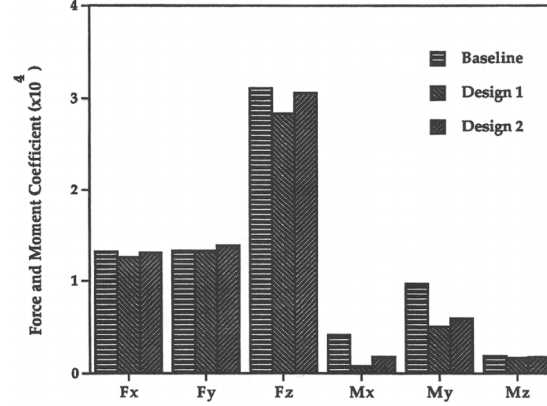
Figure 1.18: Optimized results showing decrease in 4/rev pitching and rolling moments (M_x and M_y) [42].

Multidisciplinary optimization involves blending of analysis models from different disciplines into one model. Design sensitivity computations are computed based on the blended model to reduce computational time. A blended rotor aeroelastic model obtained by combining blade structural dynamics and aerodynamics was developed in Ref. 42 for a multidisciplinary rotor blade optimization study. Finite elements were used for structurally modeling the blade, which included three rectilinear and three rotational degree of freedoms at each end. These degrees of freedom affected the relative airflow by changing the local angle of attack and relative velocity at a given point along the span, and the air-loads were computed based on the affected airflow. The calculated results from this model were verified by comparing with measured data of SA349/2 helicopter. Using this method, an optimization study was performed for minimizing vibratory hub loads and power required in hover and forward flight. The optimized design had an improved rotor performance (2.4% less power) as compared to the baseline rotor. Results also showed that about 65% and 52% decrease in amplitude for 4/rev vibratory pitch and roll moments, respectively, in the optimum design (Fig. 1.18). This new model, where design sensitivity computations were calculated using the combined structural and aerodynamic model, saved more than 80% of the CPU time.
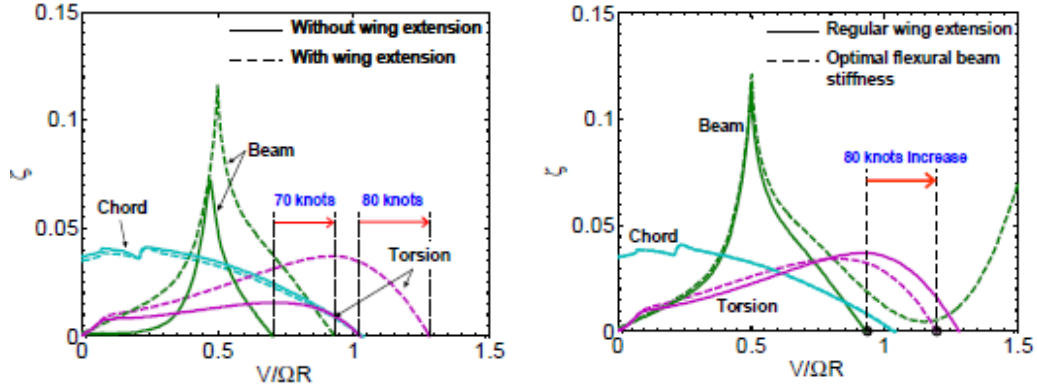
(a) Damping ratios of beam, chord and torsion modes, with and without extension.

(b) Damping ratios of beam, chord and torsion modes, for the regular and the optimal wing extension.

Figure 1.19: Influence of wing extension on whirl-flutter stability (from Ref. 43).

1.5 Recent Studies on Tiltrotors at Penn State

A 9DOF aeroelastic model that takes into account the coupled motions of the rotor, pylon, wing, wing extension, and winglet to compute the whirl flutter speed of a tiltrotor, was developed by Zhang and Smith [7, 43]. It was shown that the wing extension can significantly improve the whirl flutter speed. A wing extension could improve the damping of the beam and torsion modes by 70 knots and 80 knots, respectively (shown in Fig. 1.19a). Tuning the stiffness of the the wing extension resulted in an 80 knot increase in whirl flutter speed (shown in Fig. 1.19b). Parametric studies conducted on the winglet indicated that lowering the cant angle of the winglet improved the the beam and torsion mode stability boundaries.

The studies on the design, fabrication, and testing of low-cost, small, semi-span, sub-scale tiltrotor wind tunnel models were presented by Johnson in Ref. 44 and Costa in Ref. 2. Three generations of models were developed for the wind-tunnel tests. The first-generation model consisted of a hollow, rapid-prototyped ABS-plastic wing (Fig. 1.20a), with a three-bladed rotor consisting of constant-chord wooden blades . The Gen-1 model exhibited a whirl-flutter instability at tunnel speed of 115 ft/s. The second-generation model used the same wing, but featured composite rotor blades instead of wooden blades. The second-generation model exhibited whirl flutter at a tunnel speed of 113 ft/s. The third-generation model consisted of a composite wing, with an integrated wing spar that acted as a flexure,

(a) The hollow ABS-plastic Gen-1 wing.   (b) The composite Gen-3 wing.
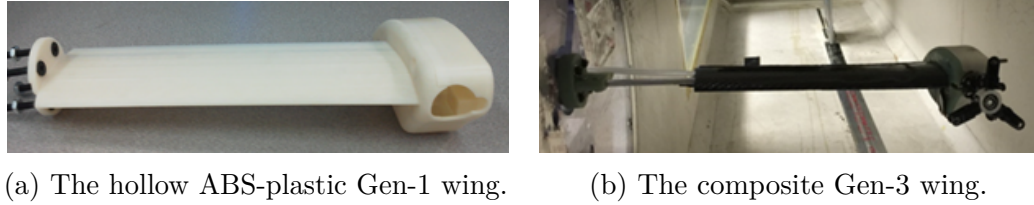
Figure 1.20: The Gen-1 and Gen-3 wings (from Refs. 2, 44)

and featured composite rotor blades. A schematic of the third-generation wing assembly is shown in Fig. 1.20b. The third-generation model, Gen-3a, exhibited whirl flutter within the test facility, at tunnel speeds of 101 and 95 ft/s, for untwisted and twisted blades, respectively.

Cole et al. [6] investigated the potential aerodynamic benefits of a adding a wing extension and a winglet to the LCTR2. A free-wake method to model the complex interaction between the wing and rotor inferences was implemented. The rotor-wing interference was shown to have a beneficial effect on the aerodynamic efficiency by lowering the induced drag. The total performance of the LCTR2 was not taken in account as the analysis methodology did not include changes in structural and aeroelastic properties of the LCTR2. The results showed that the winglet significantly improves span efficiency. The increase in span efficiency due to winglets with rotor-wing interference was approximately 6% as compared to 5% without rotor-wing interference.

Hoover [45] investigated the cruise performance optimization of the LCTR2 and the Military Heavy Tiltrotor (MHTR). The design variables were the wing extension and winglet planform variables. The objective function was the Range Specific Transport Efficiency (RSTE), which is the payload-fuel efficiency of the tiltrotor. RSTE captures both the aerodynamic and structural characteristics associated with wing extensions and winglets. The optimization results showed that the RSTE can be improved by 5.4% for the LCTR2 and 8.0% for the MHTR.

1.6 Summary

A survey of literature on tiltrotor whirl flutter reveals considerable analytical and experimental research over the years. The research reveals the causes for this instability, which are the gyroscopic precession of the rotor and the destabilizing

aerodynamic forces acting on the hub. Several tiltrotor comprehensive analysis codes have been developed which can accurately predict the stability boundaries.

Several methodologies were investigated which affect tiltrotor whirl flutter stability through analyses and experiments. One such methodology is the use of wing-tip devices such as wing extensions and winglets. The wing tip devices also improve the aerodynamic efficiency of a tiltrotor by increasing the span and reducing the induced drag. Several research studies are available in literature which investigate ways to improve the aerodynamic efficiency by using wing-tip devices on aircraft. However, the combined effects of wing-tip devices on whirl flutter and aerodynamic efficiency are not investigated yet. Wing-tip devices can also increase the weight of the aircraft. Therefore, a combined optimization study of the aeroelastic, structural, and aerodynamic effects of wing-tip devices would help tiltrotors in achieving high speeds with minimum fuel consumption.

1.7 Objectives of the Research

The main objective of this research is to improve the performance of a tiltrotor using the help of wing extensions and winglets, considering wing loading, stress, buckling, and whirl flutter constraints. The research tasks which help in achieving the main objective are:

- To develop an aeroelastic model to compute the whirl-flutter speed of a tiltrotor by including the coupled vibrations of rotor, pylon, wing, and wing-tip devices (discussed in Chapter-2).

- To conduct parametric studies aiming at improving the whirl flutter speed. The wing and wing extension parameters are stiffness, composite coupling, and structural taper (discussed in Chapter-3).

- To develop a wing structural model – to compute the wing stiffness, strength, and weight for a given wing geometry, planform variables, material properties, and torque box dimensions (discussed in Chapter-4).

- Use an aerodynamic model to conduct parametric studies on improving the lift-to-drag ratio (discussed in Chapter-5).

- Merge the wing aerodynamic analysis model into the developed aeroelastic and structural models in order to perform multi-disciplinary optimization studies. The optimization is aimed at minimizing weight penalty due to extensions and winglets, while maximizing lift-to-drag ratio, subject to strength, buckling, wing loading, and whirl flutter constraints (discussed in Chapter-6).

Chapter 2
Aeroelastic Model and Validation

An aeroelastic model consisting of a three-bladed gimballed rotor and pylon mounted on a cantilevered wing with extension and winglet is developed in this chapter. The rotor blades undergo flap (β), lag (ζ), and torsion (p) motions. The pylon has three translational degrees of freedom (x_P, y_P, z_P) and three rotational degrees of freedom $(\alpha_x, \alpha_y, \alpha_z)$, which are coupled with the wing bending and torsion motions (w, v, ϕ). In other words, the wing motion affects the rotor motion, and the resulting rotor aerodynamic and inertial forces influence the wing motion. The details of this derivation are discussed here. This model is built based on the model presented by Zhang and Smith in Ref. 7. However, Zhang and Smith did not include the rotor blade torsion DOF in their analysis. The rotor blade torsion DOF is included in the present analysis.

2.1 Rotor and Pylon Model

Consider a three-bladed rotor on a rigid pylon as illustrated in Fig. 2.1. The pylon motion at the pivot point is assumed to have six degrees of freedom – three translational and three rotational. The translational degrees of freedom of the pylon are x_P, y_P, and z_P, which are the vertical, lateral, and longitudinal motions, respectively, and the rotational degrees of freedom of the pylon are α_x, α_y, and α_z, which represent the pylon yaw, pitch, and roll motions, respectively.
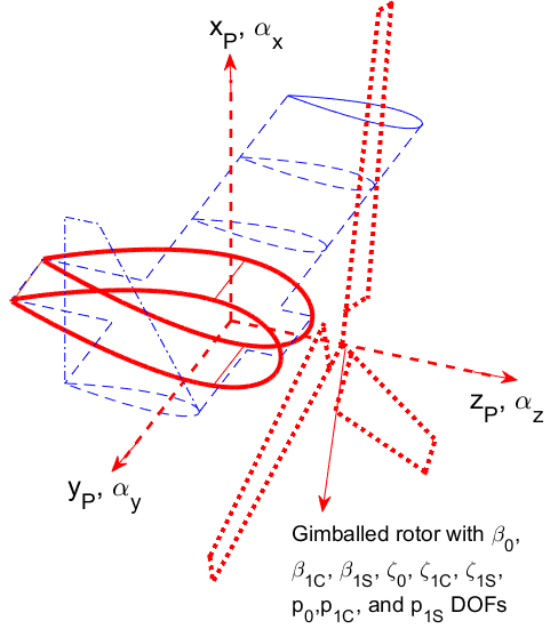
Figure 2.1: Rotor and pylon model.

2.1.1 Governing Equations

The equations of motion for the rotor flap and lag motions, along with the pylon motions included are (from Ref. 1):

$$I^*_{\beta_0}(\overset{**}{\beta_0} + \nu^2_{\beta_0}\beta_0) + S^*_{\beta_0}\overset{**}{z}_P = \frac{\gamma M_{F_0}}{ac} \tag{2.1}$$

$$I^*_\beta(\overset{**}{\beta_{1C}} + 2\overset{*}{\beta_{1S}} + (\nu^2_\beta - 1)\beta_{1C}) + I^*_{\beta\alpha}(-\overset{**}{\alpha}_y + 2\overset{*}{\alpha}_x) = \frac{\gamma M_{F_{1C}}}{ac} \tag{2.2}$$

$$I^*_\beta(\overset{**}{\beta_{1S}} - 2\overset{*}{\beta_{1C}} + (\nu^2_\beta - 1)\beta_{1S}) + I^*_{\beta\alpha}(\overset{**}{\alpha}_x + 2\overset{*}{\alpha}_y) = \frac{\gamma M_{F_{1S}}}{ac} \tag{2.3}$$

$$I^*_{\zeta 0}(\overset{**}{\zeta} + \nu^2_{\zeta 0}\zeta_0) - I^*_{\zeta 0\alpha}\overset{**}{\alpha}_z = \frac{\gamma M_{L_0}}{ac} \tag{2.4}$$

$$I_\zeta(\overset{**}{\zeta_{1C}} + 2\overset{*}{\zeta_{1S}} + (\nu^2_\zeta - 1)\zeta_{1C}) + S^*_\zeta(-\overset{**}{y}_P + h\overset{**}{\alpha}_x) = \frac{\gamma M_{L_{1C}}}{ac} \tag{2.5}$$

$$I_\zeta(\overset{**}{\zeta_{1S}} - 2\overset{*}{\zeta_{1C}} + (\nu_\zeta^2 - 1)\zeta_{1S}) + S_\zeta^*(\overset{**}{x_P} + h\overset{**}{\alpha_y}) = \frac{\gamma M_{L_{1S}}}{ac} \tag{2.6}$$

where β_p and β_t are the precone angle and the trim flapping angle, respectively. The superscripts $*$ and $**$ are the non-dimensional time derivatives. For example,

$$\overset{*}{\beta} = \frac{1}{\Omega}\frac{d\beta}{dt} \quad ; \quad \overset{**}{\beta} = \frac{1}{\Omega^2}\frac{d^2\beta}{dt^2} \tag{2.7}$$

where Ω is the rotor angular speed, and t time.

The equations governing the pitching motion (p) of a rotor blade in the rotating frame for the mth blade is given by ([12]):

$$I_p^*(\overset{**}{p} + (\omega_\theta^2 + 1)p) = M_t \tag{2.8}$$

where $M_t = -(\gamma M_0 - \beta_p - \beta_t)\zeta$. Eq. (2.8) is in the rotating frame, and is converted into the fixed frame by using the following transformations:

$$p_0 = \frac{1}{3}\sum_1^3 p^{(m)} \tag{2.9}$$

$$p_{1C} = \frac{2}{3}\sum_1^3 p^{(m)}\cos\psi_m \tag{2.10}$$

$$p_{1S} = \frac{2}{3}\sum_1^3 p^{(m)}\sin\psi_m \tag{2.11}$$

The above transformation yields the following equations for the blade pitching motion in the fixed frame:

$$I_p^*(\overset{**}{p_0} + (\omega_\theta^2 + 1)p_0) + (\gamma M_0 - \beta_p - \beta_t)\zeta_0 = 0 \tag{2.12}$$

$$I_p^*(\overset{**}{p_{1C}} - p_{1C} + 2\overset{*}{p_{1S}} + (\omega_\theta^2 + 1)p_{1C}) + (\gamma M_0 - \beta_p - \beta_t)\zeta_{1C} = 0 \tag{2.13}$$

$$I_p^*(\overset{**}{p_{1S}} - p_{1S} - 2\overset{*}{p_{1C}} + (\omega_\theta^2 + 1)p_{1S}) + (\gamma M_0 - \beta_p - \beta_t)\zeta_{1S} = 0 \tag{2.14}$$

The Equations (2.1 -2.6) and Equations (2.12 - 2.14) are the governing equations of the coupled pylon-rotor motion. The coefficients of rotor and wing DOFs appearing on the left-hand side of these equations are the inertial and frequency parameters, and are non-dimensionalized by the blade rigid flap inertia, for example

$I_\beta^* = I_\beta/I_b$. The inertia parameters are defined in terms of blade section mass and modeshapes as follows:

$$I_b = \int_0^R r^2 m\, dr \tag{2.15}$$

$$I_\beta = \int_0^R \eta_\beta^2 m\, dr \tag{2.16}$$

$$I_{\beta\alpha} = \int_0^R \eta_\beta r m\, dr \tag{2.17}$$

$$S_\beta = \int_0^R \eta_\beta m\, dr \tag{2.18}$$

$$I_\zeta = \int_0^R \eta_\zeta^2 m\, dr \tag{2.19}$$

$$I_{\zeta\alpha} = \int_0^R \eta_\zeta m r\, dr \tag{2.20}$$

$$S_\zeta = \int_0^R \eta_\zeta m\, dr \tag{2.21}$$

$$\eta_\beta = r \tag{2.22}$$

$$\eta_\zeta = r \tag{2.23}$$

where m is mass per length of the blade, and R is the length of the blade.

Certain frequencies and inertial parameters in the fixed frame are different from the parameters in the rotating frame. This is because the boundary conditions at the root vary for a gimballed rotor system based on the rotor mode involved. The collective flapping mode and the cyclic lag modes the blade acts as if it were cantilevered, while in the cyclic flap modes the blade acts as if it were hinged at root. For a windmilling rotor, the blades freely rotate about the shaft so that

$$\nu_{\zeta 0} = 0 \tag{2.24}$$

$$I_{\zeta 0}^* = 1 \tag{2.25}$$

$$I_{\zeta 0\alpha}^* = 1 \tag{2.26}$$

The terms appearing on the right hand side of Equations (2.1 -2.6), M_{F_0}, $M_{F_{1C}}$, $M_{F_{1S}}$, M_{L_0}, $M_{L_{1C}}$, $M_{L_{1S}}$, are the aerodynamic perturbation moments and are dependent on the rotor and pylon DOFs (derived in the next section).

2.1.2 Rotor Aerodynamic Perturbation Model

The rotor aerodynamics are based on linear strip theory (a detailed derivation can be found in Ref. 17). The section lift and drag, L and D, are defined as:

$$L = \frac{1}{2}\rho c(U^2)c_l \tag{2.27}$$

$$D = \frac{1}{2}\rho c(U^2)c_d \tag{2.28}$$

where c_l is the coefficient of lift, c_d is the coefficient of drag, and U is the velocity of the air relative to the blade. The velocity, U, has three components (shown in Fig. 2.2, from Ref. 20) – a tangential component (u_T), a perpendicular component (u_P), and a radial component (u_R), which are given by

$$u_T = \Omega r + \delta u_T \tag{2.29}$$

$$u_P = V + \delta u_P \tag{2.30}$$

$$u_R = 0 + \delta u_R \tag{2.31}$$
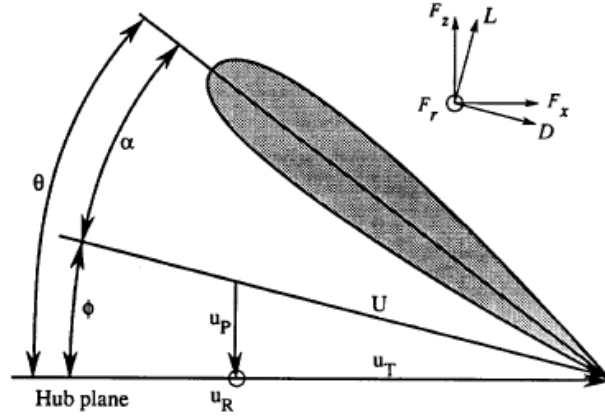
Figure 2.2: Velocity and force components of a blade section [20].

where $\delta u_T, \delta u_P$, and δu_R are the perturbation parts of the velocity components,

due to hub and rotor motions. The expressions for the perturbations are given by

$$\delta u_T = r(\overset{*}{\alpha}_z - \overset{*}{\zeta}) - h(\overset{*}{\alpha}_y)\sin\psi_m + \overset{*}{\alpha}_x\cos\psi_m + \tag{2.32}$$
$$V(\alpha_y\sin\psi_m + \alpha_x\cos\psi_m) + \overset{*}{y}_P\cos\psi_m - \overset{*}{x}_P\sin\psi_m$$

$$\delta u_p = r(\overset{*}{\beta} - \overset{*}{\alpha}_y\cos\psi_m + \overset{*}{\alpha}_x\sin\psi_m) + \overset{*}{z}_P \tag{2.33}$$

$$\delta u_R = h(-\overset{*}{\alpha}_y\cos\psi_m - \overset{*}{\alpha}_x\sin\psi_m) - \overset{*}{y}_P\sin\psi_m - \overset{*}{x}_P\cos\psi_m \tag{2.34}$$

The tangential and perpendicular velocity perturbation components are written as

$$\delta u_T = r\delta u_{T_A} + \delta u_{T_B} \tag{2.35}$$

$$\delta u_P = r\delta u_{P_B} + \delta u_{P_A} \tag{2.36}$$

such that the terms $\delta u_{T_A}, \delta u_{T_B}, \delta u_{P_A}$, and δu_{P_B} do not depend on the radial location. The perturbations of the lift and drag coefficients are

$$\delta c_l = c_{l\alpha}\delta\alpha + c_{lM}\delta M \tag{2.37}$$

$$\delta c_d = c_{d\alpha}\delta\alpha + c_{dM}\delta M \tag{2.38}$$

where following expressions are used for unstalled lift and drag perturbation parameters:

$$\frac{c_{l\alpha}}{2a} = \frac{1}{2}(1 - M^2)^{-1/2} \tag{2.39}$$

$$\frac{c_l}{2a} = \frac{\alpha}{2}(1 - M^2)^{-1/2} \tag{2.40}$$

$$\frac{c_l}{2a} + \frac{Mc_{lM}}{2a} = \frac{\alpha}{2}(1 - M^2)^{-3/2} \tag{2.41}$$

$$c_d = 0.0065 - 0.0216\alpha + 0.4\alpha^2 + \Delta c_d \tag{2.42}$$

$$\Delta c_d = 0.43(M + |\alpha|/0.26 - 0.9) \text{for} |\alpha| > \alpha_d \tag{2.43}$$

$$\Delta c_d = 0 |\alpha| < \alpha_d \tag{2.44}$$

For stalled flow, the following expressions are used

$$c_l = sgn(\alpha) \tag{2.45}$$

$$c_{l\alpha} = 0 \tag{2.46}$$

$$c_d = 2\sin^2\alpha \tag{2.47}$$

$$c_{d\alpha} = 4\sin\alpha\cos\alpha \tag{2.48}$$

$$c_{dM} = 0 \tag{2.49}$$

The other aerodynamic parameter perturbations in terms of the above perturbations are given by

$$\delta\theta = \theta - K_P\beta \tag{2.50}$$

$$\delta U = \frac{u_T\delta u_T - u_P\delta u_P}{U} \tag{2.51}$$

$$\delta M = M\delta U \tag{2.52}$$

$$\delta\alpha = \delta\theta - \frac{u_T\delta u_P - u_P\delta u_T}{U^2} \tag{2.53}$$

Resolving the section lift and drag forces into the hub-plane coordinates ($\{x, y, r\}$) yields the following equations:

$$\frac{F_z}{ac} = U\left(u_T\frac{cl}{2a} - u_P\frac{c_d}{2a}\right) \tag{2.54}$$

$$\frac{F_x}{ac} = U\left(u_P\frac{cl}{2a} + u_T\frac{c_d}{2a}\right) \tag{2.55}$$

$$\frac{F_r}{ac} = Uu_R\frac{cd}{2a} - \beta\frac{F_z}{2a} \tag{2.56}$$

The coefficients appearing on the right-hand side of Equations (2.1-2.6), ($\{M_{F_0},\ M_{F_{1C}},\ M_{F_{1S}},\ M_{L_0},\ M_{L_{1C}},\ M_{L_{1S}}\}$) are the aerodynamic perturbation moments. The expressions for these terms are:

$$M_{F_0} = \frac{1}{3}\sum_1^3\int_0^R F_z r\ dr$$

$$= M_0 + M_{\overset{*}{\zeta}}(\overset{*}{\alpha}_z - \overset{*}{\zeta}_0) + M_{\overset{*}{\beta}}\overset{*}{\beta}_0 +$$
$$M_\lambda \overset{*}{z}_P + M_\theta(\theta_0 - K_P\beta_0) \tag{2.57}$$

$$M_{F_{1C}} = \frac{2}{3}\sum_1^3 \int_0^R F_z r \cos\psi_m \; dr$$

$$= M_\mu(-h\overset{*}{\alpha}_x + V\alpha_x + \overset{*}{y}_P) +$$
$$M_{\overset{*}{\zeta}}(\overset{*}{\zeta}_{1C} - \overset{*}{\zeta}_{1S}) + M_{\overset{*}{\beta}}(\overset{*}{\beta}_{1C} + \beta_{1S} - \overset{*}{\alpha}_y) +$$
$$M_\theta(\theta_{1C} - K_P\beta_{1C}) \tag{2.58}$$

$$M_{F_{1S}} = \frac{2}{3}\sum_1^3 \int_0^R F_z r \sin\psi_m \; dr$$

$$= M_\mu(-h\overset{*}{\alpha}_y + V\alpha_y - \overset{*}{x}_P) +$$
$$M_{\overset{*}{\zeta}}(\overset{*}{\zeta}_{1C} - \overset{*}{\zeta}_{1S}) + M_{\overset{*}{\beta}}(\overset{*}{\beta}_{1S} - \beta_{1C} + \overset{*}{\alpha}_x) +$$
$$M_\theta(\theta_{1S} - K_P\beta_{1S}) \tag{2.59}$$

$$M_{L_0} = \frac{1}{3}\sum_1^3 \int_0^R F_x r \; dr$$

$$= Q_0 + Q_{\overset{*}{\zeta}}(\overset{*}{\alpha}_z - \overset{*}{\zeta}_0) + Q_{\overset{*}{\beta}}\overset{*}{\beta}_0 +$$
$$Q_\lambda \overset{*}{z}_P + Q_\theta(\theta_0 - K_P\beta_0) \tag{2.60}$$

$$M_{L_{1C}} = \frac{2}{3}\sum_1^3 \int_0^R F_x r \cos\psi_m \; dr$$

$$= Q_\mu(-h\overset{*}{\alpha}_x + V\alpha_x + \overset{*}{y}_P) +$$
$$Q_{\overset{*}{\zeta}}(\overset{*}{\zeta}_{1C} - \overset{*}{\zeta}_{1S}) + Q_{\overset{*}{\beta}}(\overset{*}{\beta}_{1C} + \beta_{1S} - \overset{*}{\alpha}_y) +$$
$$Q_\theta(\theta_{1C} - K_P\beta_{1C}) \tag{2.61}$$

33

$$M_{L_{1S}} = \frac{2}{3} \sum_1^3 \int_0^R F_x r \sin\psi_m \ dr$$

$$= Q_\mu(-h\overset{*}{\alpha}_y + V\alpha_y - \overset{*}{x}_P) +$$
$$Q_{\overset{*}{\zeta}}(\overset{*}{\zeta}_{1C} - \overset{*}{\zeta}_{1S}) + Q_{\overset{*}{\beta}}(\overset{*}{\beta}_{1S} - \beta_{1C} + \overset{*}{\alpha}_x) +$$
$$Q_\theta(\theta_{1S} - K_P\beta_{1S}) \qquad (2.62)$$

The hub forces are also dependent on the rotor perturbation terms. The expressions for the hub forces in the non-dimensional form is given by:

$$\frac{C_T}{\sigma\alpha} = \frac{1}{3} \sum_m \int_0^1 \frac{F_z}{ac} dr$$

$$= T_0 + T_{\overset{*}{\zeta}}(\overset{*}{\alpha}_z - \overset{*}{\zeta}_0) + T_{\overset{*}{\beta}}\overset{*}{\beta}_0 +$$
$$T_\lambda \overset{*}{z}_P + T_\theta(\theta_0 - K_P\beta_0) \qquad (2.63)$$

$$\frac{2C_H}{\sigma\alpha} = \frac{2}{3} \sum_m \int_0^1 (\frac{F_r}{ac} \cos\psi_m + \frac{F_x}{ac} \sin\psi_m) dr$$

$$= (H_\mu + R_\mu)(-h\overset{*}{\alpha}_y + V\alpha_y - \overset{*}{x}_P) +$$
$$H_{\overset{*}{\zeta}}(\overset{*}{\zeta}_{1C} - \overset{*}{\zeta}_{1S}) + H_{\overset{*}{\beta}}(\overset{*}{\beta}_{1S} - \beta_{1C} + \overset{*}{\alpha}_x) +$$
$$H_\theta(\theta_{1S} - K_P\beta_{1S}) \qquad (2.64)$$

$$\frac{2C_Y}{\sigma\alpha} = \frac{2}{3} \sum_m \int_0^1 (\frac{F_r}{ac} \sin\psi_m - \frac{F_x}{ac} \cos\psi_m) dr$$

$$= -((H_\mu + R_\mu))(-h\overset{*}{\alpha}_x + V\alpha_x + \overset{*}{y}_P) -$$
$$H_{\overset{*}{\zeta}}(\overset{*}{\zeta}_{1C} - \overset{*}{\zeta}_{1S}) - H_{\overset{*}{\beta}}(\overset{*}{\beta}_{1S} + \beta_{1C} + \overset{*}{\alpha}_y) +$$
$$H_\theta(\theta_{1C} - K_P\beta_{1C}) \qquad (2.65)$$

34

$$\frac{C_Q}{\sigma\alpha} = \frac{1}{3}\sum_m \int_0^1 \frac{F_x}{ac}dr$$

$$= Q_0 + Q_{*\zeta}(\overset{*}{\alpha}_z - \overset{*}{\zeta}_0) + Q_{*\beta}\overset{*}{\beta}_0 +$$
$$Q_\lambda \overset{*}{z}_P + Q_\theta(\theta_0 - K_P\beta_0) \tag{2.66}$$

Inertial contributions to the hub forces must be added to the above aerodynamic contributions:

$$\left(\frac{C_T}{\sigma\alpha}\right)_{int} = -\frac{S_{\beta_0}^*}{\gamma}\overset{**}{\beta}_0 - \frac{M_b^*}{\gamma}\overset{**}{z}_P \tag{2.67}$$

$$\left(\frac{2C_H}{\sigma\alpha}\right)_{int} = -\frac{S_\zeta^*}{\gamma}\overset{**}{\zeta}_{1S} - \frac{2M_b^*}{\gamma}(\overset{**}{x}_P + h\overset{**}{\alpha}_y) \tag{2.68}$$

$$\left(\frac{2C_Y}{\sigma\alpha}\right)_{int} = -\frac{S_\zeta^*}{\gamma}\overset{**}{\zeta}_{1C} - \frac{2M_b^*}{\gamma}(\overset{**}{y}_P + h\overset{**}{\alpha}_x) \tag{2.69}$$

$$\left(\frac{C_Q}{\sigma\alpha}\right)_{int} = -\frac{I_{\zeta_0\alpha}^*}{\gamma}\overset{**}{\zeta}_0 - \frac{I_0^*}{\gamma}\overset{**}{\alpha}_z \tag{2.70}$$

The the hub moment coefficients, C_{M_x} and C_{M_y} can be expressed as

$$\frac{2C_{M_x}}{\sigma\alpha} = -\frac{I_\beta^*}{\gamma}(\nu_\beta^2 - 1)\beta_{1S} \tag{2.71}$$

$$\frac{2C_{M_y}}{\sigma\alpha} = -\frac{I_\beta^*}{\gamma}(\nu_\beta^2 - 1)\beta_{1C} \tag{2.72}$$

The aerodynamic coefficients $M, H, T, Q,$ and R represent flap moment, in-plane drag force, thrust, torque, and blade radial force, respectively. The terms such as H_μ represent the perturbation coefficients of the forces and moments. The subscripts of these perturbation coefficients designate the source of the perturbation: 0 is the trim value, μ is hub inplane velocity, $\overset{*}{\zeta}$ is blade rotational velocity, $\overset{*}{\beta}$ is flap velocity, λ is hub inflow velocity, and θ is blade pitch. The expressions for the aerodynamic perturbation coefficients are listed below. The derivation of these expressions can be found in Ref. 17.

$$T_0 = \int_0^1 U\left[\frac{rc_l}{2a} - \frac{Vc_d}{2a}\right]dr \tag{2.73}$$

$$T_\theta = \int_0^1 U \left[\frac{r c_{l\alpha}}{2a} - \frac{V c_{d\alpha}}{2a} \right] dr \qquad (2.74)$$

$$T_\mu = \int_0^1 \left[\frac{c_l}{2a} U + (\frac{c_l}{2a} + \frac{M c_{lM}}{2a}) \frac{r^2}{U} - (\frac{c_d}{2a} + \frac{M c_{dM}}{2\alpha}) \frac{rV}{U} + \right.$$
$$\left. (\frac{r c_{l\alpha}}{2a} - \frac{V c_{d\alpha}}{2a}) \frac{V}{U} \right] dr \qquad (2.75)$$

$$T_{\overset{*}{\zeta}} = \int_0^1 r \left[\frac{c_l}{2a} U + (\frac{c_l}{2a} + \frac{M c_{lM}}{2a}) \frac{r^2}{U} - (\frac{c_d}{2a} + \frac{M c_{dM}}{2\alpha}) \frac{rV}{U} + \right.$$
$$\left. (\frac{r c_{l\alpha}}{2a} - \frac{V c_{d\alpha}}{2a}) \frac{V}{U} \right] dr \qquad (2.76)$$

$$T_{\overset{*}{\beta}} = \int_0^1 r \left[-\frac{c_d}{2a} U + (\frac{c_l}{2a} + \frac{M c_{lM}}{2a}) \frac{rV}{U} - (\frac{c_d}{2a} + \frac{M c_{dM}}{2a}) \frac{V^2}{U} - \right.$$
$$\left. (\frac{r c_{l\alpha}}{2a} - \frac{V c_{d\alpha}}{2a}) \frac{r}{U} \right] dr \qquad (2.77)$$

$$T_\lambda = \int_0^1 \left[-\frac{c_d}{2a} U + (\frac{c_l}{2a} + \frac{M c_{lM}}{2a}) \frac{rV}{U} - (\frac{c_d}{2a} + \frac{M c_{dM}}{2a}) \frac{V^2}{U} - \right.$$
$$\left. (\frac{r c_{l\alpha}}{2a} - \frac{V c_{d\alpha}}{2a}) \frac{r}{U} \right] dr \qquad (2.78)$$

$$M_0 = \int_0^1 rU \left[\frac{r c_l}{2a} - \frac{V c_d}{2a} \right] dr \qquad (2.79)$$

$$M_\theta = \int_0^1 rU \left[\frac{r c_{l\alpha}}{2a} - \frac{V c_{d\alpha}}{2a} \right] dr \qquad (2.80)$$

$$M_\mu = \int_0^1 r \left[\frac{c_l}{2a} U + (\frac{c_l}{2a} + \frac{M c_{lM}}{2a}) \frac{r^2}{U} - (\frac{c_d}{2a} + \frac{M c_{dM}}{2\alpha}) \frac{rV}{U} + \right.$$

$$\left(\frac{rc_{l\alpha}}{2a} - \frac{Vc_{d\alpha}}{2a}\right)\frac{V}{U}\right]dr \qquad (2.81)$$

$$M_{\zeta}^* = \int_0^1 r^2\left[\frac{c_l}{2a}U + \left(\frac{c_l}{2a} + \frac{Mc_{lM}}{2a}\right)\frac{r^2}{U} - \left(\frac{c_d}{2a} + \frac{Mc_{dM}}{2\alpha}\right)\frac{rV}{U} + \right.$$
$$\left.\left(\frac{rc_{l\alpha}}{2a} - \frac{Vc_{d\alpha}}{2a}\right)\frac{V}{U}\right]dr \qquad (2.82)$$

$$M_{\beta}^* = \int_0^1 r^2\left[-\frac{c_d}{2a}U + \left(\frac{c_l}{2a} + \frac{Mc_{lM}}{2a}\right)\frac{rV}{U} - \left(\frac{c_d}{2a} + \frac{Mc_{dM}}{2a}\right)\frac{V^2}{U} - \right.$$
$$\left.\left(\frac{rc_{l\alpha}}{2a} - \frac{Vc_{d\alpha}}{2a}\right)\frac{r}{U}\right]dr \qquad (2.83)$$

$$M_{\lambda} = \int_0^1 r\left[-\frac{c_d}{2a}U + \left(\frac{c_l}{2a} + \frac{Mc_{lM}}{2a}\right)\frac{rV}{U} - \left(\frac{c_d}{2a} + \frac{Mc_{dM}}{2a}\right)\frac{V^2}{U} - \right.$$
$$\left.\left(\frac{rc_{l\alpha}}{2a} - \frac{Vc_{d\alpha}}{2a}\right)\frac{r}{U}\right]dr \qquad (2.84)$$

$$H_0 == \int_0^1 U\left[\frac{Vc_l}{2a} + \frac{rc_d}{2a}\right]dr \qquad (2.85)$$

$$H_{\theta} = \int_0^1 U\left[\frac{Vc_{l\alpha}}{2a} + \frac{rc_{d\alpha}}{2a}\right]dr \qquad (2.86)$$

$$H_{\mu} = \int_0^1\left[\frac{c_d}{2a}U + \left(\frac{c_l}{2a} + \frac{Mc_{lM}}{2a}\right)\frac{rV}{U} + \left(\frac{c_d}{2a} + \frac{Mc_{dM}}{2a}\right)\frac{r^2}{U} + \right.$$
$$\left.\left(\frac{Vc_{l\alpha}}{2a} + \frac{Vc_{d\alpha}}{2a}\right)\frac{r}{U}\right]dr \qquad (2.87)$$

$$H_{\zeta}^* = \int_0^1 r\left[\frac{c_d}{2a}U + \left(\frac{c_l}{2a} + \frac{Mc_{lM}}{2a}\right)\frac{rV}{U} + \left(\frac{c_d}{2a} + \frac{Mc_{dM}}{2a}\right)\frac{r^2}{U} + \right.$$

$$\left(\frac{Vc_{l\alpha}}{2a} + \frac{Vc_{d\alpha}}{2a}\right)\frac{r}{U}\Bigg] dr \qquad (2.88)$$

$$H_{\underset{\beta}{*}} = \int_0^1 r\left[\frac{c_l}{2a}U + \left(\frac{c_l}{2a} + \frac{Mc_{lM}}{2a}\right)\frac{V^2}{U} + \left(\frac{c_d}{2a} + \frac{Mc_{dM}}{2a}\right)\frac{rV}{U} - \right.$$
$$\left. \left(\frac{Vc_{l\alpha}}{2a} + \frac{Vc_{d\alpha}}{2a}\right)\frac{r}{U}\right] dr \qquad (2.89)$$

$$H_{\lambda} = \int_0^1 \left[\frac{c_l}{2a}U + \left(\frac{c_l}{2a} + \frac{Mc_{lM}}{2a}\right)\frac{V^2}{U} + \left(\frac{c_d}{2a} + \frac{Mc_{dM}}{2a}\right)\frac{rV}{U} - \right.$$
$$\left. \left(\frac{Vc_{l\alpha}}{2a} + \frac{Vc_{d\alpha}}{2a}\right)\frac{r}{U}\right] dr \qquad (2.90)$$

$$Q_0 = = \int_0^1 rU\left[\frac{Vc_l}{2a} + \frac{rc_d}{2a}\right] dr \qquad (2.91)$$

$$Q_\theta = \int_0^1 rU\left[\frac{Vc_{l\alpha}}{2a} + \frac{rc_{d\alpha}}{2a}\right] dr \qquad (2.92)$$

$$Q_\mu = \int_0^1 r\left[\frac{c_d}{2a}U + \left(\frac{c_l}{2a} + \frac{Mc_{lM}}{2a}\right)\frac{rV}{U} + \left(\frac{c_d}{2a} + \frac{Mc_{dM}}{2a}\right)\frac{r^2}{U} + \right.$$
$$\left. \left(\frac{Vc_{l\alpha}}{2a} + \frac{Vc_{d\alpha}}{2a}\right)\frac{r}{U}\right] dr \qquad (2.93)$$

$$Q_{\underset{\zeta}{*}} = \int_0^1 r^2\left[\frac{c_d}{2a}U + \left(\frac{c_l}{2a} + \frac{Mc_{lM}}{2a}\right)\frac{rV}{U} + \left(\frac{c_d}{2a} + \frac{Mc_{dM}}{2a}\right)\frac{r^2}{U} + \right.$$
$$\left. \left(\frac{Vc_{l\alpha}}{2a} + \frac{Vc_{d\alpha}}{2a}\right)\frac{r}{U}\right] dr \qquad (2.94)$$

$$Q_{\underset{\beta}{*}} = \int_0^1 r^2\left[\frac{c_l}{2a}U + \left(\frac{c_l}{2a} + \frac{Mc_{lM}}{2a}\right)\frac{V^2}{U} + \left(\frac{c_d}{2a} + \frac{Mc_{dM}}{2a}\right)\frac{rV}{U} - \right.$$

$$\left(\frac{Vc_{l\alpha}}{2a} + \frac{Vc_{d\alpha}}{2a}\right)\frac{r}{U}\Bigg]dr \qquad (2.95)$$

$$Q_\lambda = \int_0^1 r\Bigg[\frac{c_l}{2a}U + \left(\frac{c_l}{2a} + \frac{Mc_{lM}}{2a}\right)\frac{V^2}{U} + \left(\frac{c_d}{2a} + \frac{Mc_{dM}}{2a}\right)\frac{rV}{U} - \left(\frac{Vc_{l\alpha}}{2a} + \frac{Vc_{d\alpha}}{2a}\right)\frac{r}{U}\Bigg]dr \qquad (2.96)$$

The above force and moment derivatives are computed numerically using the Gauss-Legendre quadrature. The rotor is trimmed by adjusting the collective pitch (θ_0) such that the rotor torque ($Q_0 = 0$).

2.2 Wing and Extension Model

The wing structural model is based on a finite element formulation, where the wing is discretized into several elements, and Hamilton's principle is applied for each element on the total energy of the system. The wing is assumed to undergo a vertical bending motion ($w(x)$), a chordwise bending motion ($v(x)$), and torsional motion ($\phi(x)$). For a single element, $v(x), w(x)$, and $\phi(x)$ can be written as a linear combinations of shape functions such that

$$\hat{u} = [w \ v \ \phi]^T = [H][q] \qquad (2.97)$$

where

$$[q]^T = [w_1 \ v_1 \ \phi_1 \ v_1' \ w_1' \ w_2 \ v_2 \ \phi_2 \ v_2' \ w_2'] \qquad (2.98)$$

are the discretized DOFs, and $[H]$ is given by:

$$[H] = \begin{bmatrix} H_b^1 & 0 & 0 & 0 & H_b^2 & H_b^3 & 0 & 0 & 0 & H_b^4 \\ 0 & H_b^1 & 0 & H_b^2 & 0 & 0 & H_b^3 & 0 & H_b^4 & 0 \\ 0 & 0 & H_\theta^1 & 0 & 0 & 0 & 0 & H_\theta^2 & 0 & 0 \end{bmatrix} \qquad (2.99)$$

where H_b^i, $i = 1, 2, 3, 4$ are the standard cubic Hermitian shape functions, and H_θ^i, $i = 1, 2$ are the standard linear Hermitian shape functions. A schematic of the finite element discretization of the wing is shown in Fig. 2.3.
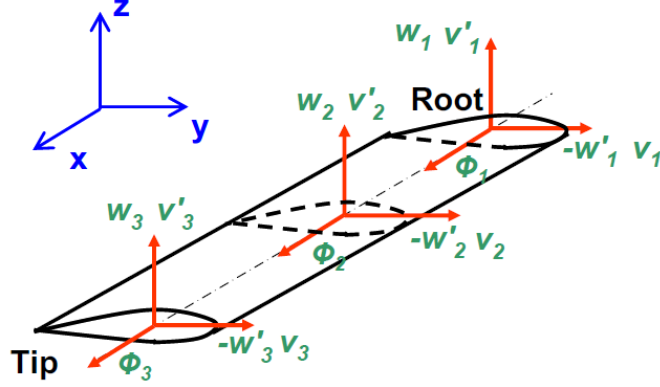
Figure 2.3: A schematic of the finite element model of the wing [7].

The strain energy V for a single element of the wing is given by:

$$V = \frac{1}{2} \int_0^L [w'' \ v'' \ \phi'][K_s][w'' \ v'' \ \phi']^T dx \tag{2.100}$$

where

$$[K_s] = \begin{bmatrix} EI_b & 0 & K_{bt} \\ 0 & EI_c & K_{ct} \\ K_{bt} & K_{ct} & GJ \end{bmatrix} \tag{2.101}$$

where EI_b is the beamwise bending stiffness, EI_c is the chordwise bending stiffness, GJ is the torsional stiffness, K_{bt} is the beamwise bending-torsion coupling parameter, K_{ct} is the chordwise bending-torsion coupling parameter, and L is the length of the element. The notations v' and v'' represent dv/dx and d^2v/dx^2, respectively. The strain energy can be written in terms of the discrete DOFs as

$$V = \frac{1}{2}[q]^T[K_S][q] \tag{2.102}$$

where

$$[K_S] = \int_0^L [H'']^T[K_s][H''] \ dx \tag{2.103}$$

The kinetic energy of the wing element can be written as

$$T = \int_0^L \frac{1}{2}\rho(\dot{u}_x{}^2 + \dot{u}_y{}^2 + \dot{u}_z{}^2) \ dV = \dot{q}^T[M_S]\dot{q} \tag{2.104}$$

40

where

$$\dot{u}_x = 0 \tag{2.105}$$

$$\dot{u}_y = \dot{v} \tag{2.106}$$

$$\dot{u}_z = \dot{w} + y\dot{\phi} \tag{2.107}$$

$$[M_S] = \int_0^L [H]^T [M_s][H] \ dx$$

$$= \begin{bmatrix} m & 0 & S_\alpha \\ 0 & m & 0 \\ S_\alpha & 0 & I_\theta \end{bmatrix} = \int\int_A \rho \begin{bmatrix} 1 & 0 & y \\ 0 & 1 & 0 \\ y & 0 & y^2 \end{bmatrix} dA \tag{2.108}$$

The notation $\dot{u}$ represents du/dt. The expressions for kinetic and strain energies computed here will be used in the coming sections when applying the Hamilton's principle.

The wing and extension are modeled with sweep Λ. The extension is modeled with an offset d_{ex} (see Fig. 2.4). The quasi-steady lift approximation can now be written as

$$\alpha = \alpha_0 + \phi \cos\Lambda - \frac{\dot{w}}{U} + \frac{\dot{\phi}}{U}(d_{ex} + x\sin\Lambda - e) - w'\sin\Lambda \tag{2.109}$$

where w, w', and ϕ are the continuous degrees of freedom of the wing. These degrees of freedom can be written as a linear combination of the discretized DOFs as:

$$[\hat{u}^A] = [H_A][q] \tag{2.110}$$

where

$$[\hat{u_A}] = [w \ v \ \phi \ v' \ w' \ ]^T \tag{2.111}$$

$$[H_A] = \begin{bmatrix} H_b^1 & 0 & 0 & 0 & H_b^2 & H_b^3 & 0 & 0 & 0 & H_b^4 \\ 0 & H_b^1 & 0 & H_b^2 & 0 & 0 & H_b^3 & 0 & H_b^4 & 0 \\ 0 & 0 & H_\theta^1 & 0 & 0 & 0 & 0 & H_\theta^2 & 0 & 0 \\ 0 & (H_b^1)' & 0 & (H_b^2)' & 0 & 0 & (H_b^3)' & 0 & (H_b^4)' & 0 \\ (H_b^1)' & 0 & 0 & 0 & (H_b^2)' & (H_b^3)' & 0 & 0 & 0 & (H_b^4)' \end{bmatrix}$$
$$\tag{2.112}$$

$$q = [w_1 \ v_1 \ \phi_1 \ v_1' \ w_1' \ w_2 \ v_2 \ \phi_2 \ v_2' \ w_2']^T \tag{2.113}$$

41
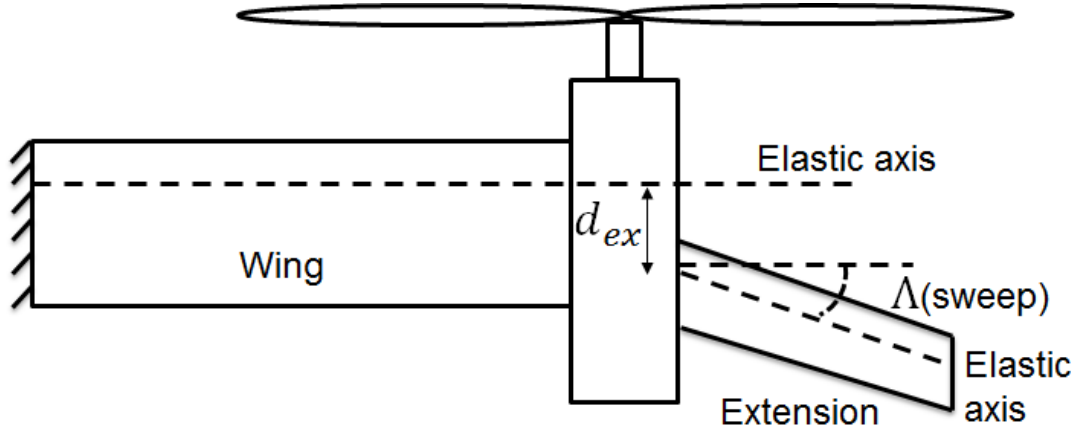
Figure 2.4: A schematic of a swept extension with an offset.

The aerodynamic forces and moments are

$$L = qcc_{l\alpha}\alpha \tag{2.114}$$

$$M = Le_1 \tag{2.115}$$

where $e_1 = -(d_{ex} + x\sin\Lambda - e)$ In matrix form, the forces and moments can be written as

$$[L] = \begin{bmatrix} L_w \\ L_v \\ M_\phi \\ M_x \\ M_y \end{bmatrix} = [A_4] \begin{bmatrix} w \\ v \\ \phi \\ v' \\ w' \end{bmatrix} + [A_5] \begin{bmatrix} \dot{w} \\ \dot{v} \\ \dot{\phi} \\ \dot{v}' \\ \dot{w}' \end{bmatrix} \tag{2.116}$$

where $[A_4]$ and $[A_5]$ are given by

$$[A_4] = \begin{bmatrix} 0 & 0 & qcc_{l\alpha}\cos\Lambda & 0 & qcc_{l\alpha}\sin\Lambda \\ 0 & 0 & 0 & 0 & 0 \\ 0 & 0 & e_1 qcc_{l\alpha}\cos\Lambda & 0 & e_1 qcc_{l\alpha}\sin\Lambda \\ 0 & 0 & 0 & 0 & 0 \\ 0 & 0 & 0 & 0 & 0 \end{bmatrix} \tag{2.117}$$

$$[A_5] = \begin{bmatrix} -qcc_{l\alpha}/U & 0 & -qcc_{l\alpha}/Ue_1 & 0 & 0 \\ 0 & 0 & 0 & 0 & 0 \\ -qcc_{l\alpha}/Ue_1 & 0 & -qcc_{l\alpha}/Ue_1^2 & 0 & 0 \\ 0 & 0 & 0 & 0 & 0 \\ 0 & 0 & 0 & 0 & 0 \end{bmatrix} \qquad (2.118)$$

The work done by the conservative forces and moments can now be expressed as:

$$W = [q]^T \int_0^1 [H_A]^T [A_4][H_A] \, dx [q] \qquad (2.119)$$

The non-conservative forces (due to aerodynamic damping, F_D) can be written as

$$F_D = \int_0^1 [H_A]^T [A_5][H_A] \, dx [\dot{q}] \qquad (2.120)$$

Applying the Euler-Lagrange equations for strain energy, V (Eq. 2.102), the kinetic energy T (Eq. 2.104), the external work done W (Eq. 2.119), and the non-conservative force F_D (Eq. 2.120), we get

$$\frac{\partial Lg}{\partial q} - \frac{d}{dt}\frac{\partial Lg}{\partial \dot{q}} = F_D \qquad (2.121)$$

where Lg is the lagrangian of the wing element, given by

$$Lg = T - V + W \qquad (2.122)$$

Applying the Euler-Lagrange equations for the strain and kinetic energies of the wing yields the following set of equations for each element:

$$\mathbf{M}_W \ddot{X}_W + \mathbf{C}_W \dot{X}_W + \mathbf{K}_W X_W = F_W \qquad (2.123)$$

where $X_W = [w_1 \ v_1 \ \phi_1 \ v_1' \ w_1' \ w_2 \ v_2 \ \phi_2 \ v_2' \ w_2']$ is the vector containing the DOFs corresponding to the wing, and $\mathbf{M}_W$, $\mathbf{C}_W$, and $\mathbf{K}_W$ are the mass, damping, and stiffness matrices of the wing, respectively. The detailed derivation of the wing modeling, and the expressions for $\mathbf{M}_W$, $\mathbf{C}_W$, $\mathbf{K}_W$ can be found in the Appendix-A.

2.3 Winglet Model

The winglet is assumed to be rigid, and is connected to the wing extension tip. The winglet is swept by an angle θ_s and canted by an angle θ_c as shown in Fig. 2.5 (from Ref. 7 and Ref. 45). The detailed derivation of the winglet model can be found in Ref. 7.

(a) Winglet sweep.　　　　(b) Winglet cant angle.
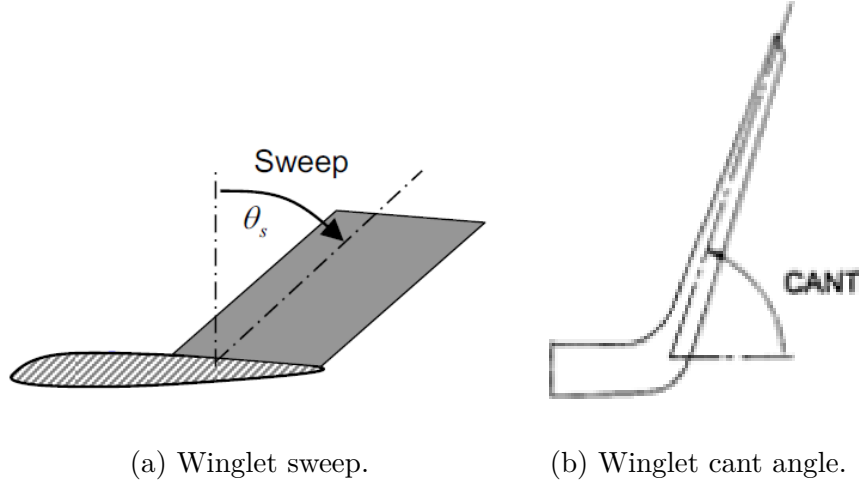
Figure 2.5: A schematic showing winglet sweep and cant angles (from Ref. 7).

The wing motion causes a perturbation in the angle of attack as seen by the winglet. The effective angle of attack can be written as

$$\alpha_{eff} = \phi_{wl} \cos \theta_s - \dot{w}_{wl}/V \tag{2.124}$$

where $\dot{w}_{wl}$ is the velocity of the wind as seen by the winglet, and ϕ_{wl} is the twist additional wing twist as seen by the winglet. The expressions for $\dot{w}_{wl}$ and ϕ_{wl}

$$\dot{w}_{wl} = \dot{w}_2 \cos \theta_c + \dot{w}_2' x \cos \theta_s - (\dot{\phi}_2 \cos \theta_c + \dot{v}_2 \sin \theta_c) x \sin \theta_s \tag{2.125}$$

$$\phi_{wl} = \phi_2 \cos \theta_c + v_2' \sin \theta_c \tag{2.126}$$

and the subscript 2 indicated the DOF of the node at which the winglet is added to the wing extension.

The sectional lift generated by the winglet due the effective angle of attack is

given by

$$L_{wl} = \frac{1}{2}\rho V^2 c c_{l\alpha} \alpha_{eff} \tag{2.127}$$

The generalized forces due this lift are given by

$$L_w = \int_0^L L_{wl} \cos\theta_c x \ dz \tag{2.128}$$

$$L_v = 0 \tag{2.129}$$

$$M_\phi = -\int_0^L L_{wl} \cos\theta_c (d + x \sin\theta_s) \ dz \tag{2.130}$$

$$M_x = -\int_0^L L_{wl} \sin\theta_c (d + x \sin\theta_s) \ dz \tag{2.131}$$

$$M_y = -\int_0^L L_{wl} \cos\theta_c x \ dz \tag{2.132}$$

These generalized forces are computed numerically and must be added to the finite element model of the wing at the nodes where the wing extension is attached to the winglet.

2.4 Coupling of the Wing and Rotor Systems

The wing is coupled to the rotor through the degrees of freedom at the wing-tip. There are two ways in which the coupling occurs:

1. The rotor system DOFs at the pylon pivot point are kinematically related to the degrees of wing DOFs.

2. The rotor hub forces, which are functions of the rotor perturbation parameters, force the motion of the wing.

The relationship between the pylon DOFs at the pivot point and the wing DOFs are

$$x_P = w_2 \tag{2.133}$$

$$y_P = v_2 \sin\Lambda \tag{2.134}$$

$$z_P = v_2 \cos\Lambda \tag{2.135}$$

$$\alpha_x = v_2' \tag{2.136}$$

$$\alpha_y = \phi_2 \cos \Lambda - w_2' \sin \Lambda \tag{2.137}$$

$$\alpha_z = -\phi_2 \sin \Lambda - w_2' \cos \Lambda \tag{2.138}$$

The subscript 2 indicated the DOF with the node at the wing-tip of the the beam element. These relationships are substituted in the rotor system equations and the net hub force equations. The expressions for the generalized rotor hub forces are

$$F_R = \left(\frac{3\gamma I_b \Omega^2}{\sigma \alpha}\right) \begin{bmatrix} C_H \\ C_T \cos \Lambda + C_Y \sin \Lambda \\ (C_{M_y} + \bar{h}C_H)\cos \Lambda + C_Q \sin \Lambda \\ C_{M_x} - \bar{h}C_Y \\ -C_Q \cos \Lambda + C_{M_y} + \bar{h}C_H)\sin \Lambda \end{bmatrix} \tag{2.139}$$

The generalized rotor hub forces must be added to the finite element model of the wing at the point where the pylon is attached to the rotor. These generalized rotor hub forces are aerodynamic forces acting at the hub in the fixed frame, and are *not* the internal nodal forces the aerodynamic forces acting at the rotor hub.

After assembly, the equations for the rotor/wing coupling system can be written in the following matrix form:

$$\mathbf{M}_R \ddot{X}_R + \Omega \mathbf{C}_R \ddot{X}_R + \Omega^2 \mathbf{K}_R X_W = F_R \tag{2.140}$$

where X_W is the vector containing the DOFs of the rotor and pylon, and

$$X_R = [w_2 \ v_2 \ \phi_2 \ v_2' \ w_2' \ \beta_0 \ \beta_{1C} \ \beta_{1S} \ \zeta_0 \ \zeta_{1C} \ \zeta_{1S} \ p_0 \ p_{1C} \ p_{1S}]^T \tag{2.141}$$

The expressions for $\mathbf{M}_R$, $\mathbf{C}_R$, and $\mathbf{K}_R$ can be found in the Appendix-A.

The independent DOFs obtained after coupling the wing and rotor DOFs are:

$$X = [w_1 \ v_1 \ \phi_1 \ v_1' \ w_1' \ w_2 \ v_2 \ \phi_2 \ v_2' \ w_2'$$
$$w_3 \ v_3 \ \phi_3 \ v_3' \ w_3' \ w_4 \ v_4 \ \phi_4 \ v_4' \ w_4'$$
$$w_5 \ v_5 \ \phi_5 \ v_5' \ w_5' \ w_6 v_6 \ \phi_6 \ v_6' \ w_6'$$
$$\beta_0 \ \beta_{1C} \ \beta_{1S} \ \zeta_0 \ \zeta_{1C} \ \zeta_{1S} \ p_0 \ p_{1C} \ p_{1S}] \tag{2.142}$$

where DOFS such as w_1 and w_2 correspond to node 1 and node 2, respectively. Node 1, node 2, node 3 correspond to the wing, nodes 3 and 4 correspond to the nacelle, nodes 4 and 5 correspond to the extension, and nodes 5 and 6 correspond to the winglet. The other DOFs such as β_0, β_{1C}, etc., correspond to the rotor.

2.5 Eigenvalues

After assembling the equations using standard finite-element techniques, the equations of motion can be written as

$$M\ddot{X} + C\dot{X} + KX = 0 \tag{2.143}$$

where X is vector containing all the degrees of freedom, M, C, and K are the mass, damping and stiffness matrices, respectively. The frequency and damping characteristics of the system can be calculated from the eigenvalues (λ_i) of Eq. 2.143. The frequency (ω_i) and damping (ζ_i) are given by

$$\omega_i = Im(\lambda_i) \tag{2.144}$$

$$\zeta_i = \frac{Re(\lambda_i)}{|\lambda_i|} \tag{2.145}$$

A particular mode becomes unstable becomes unstable when the damping of that particular mode goes to zero. The lowest forward speed at which the damping of any of the modes is zero, is defined as the whirl flutter speed.

2.6 Validation

The present analysis is validated with experimental data from two semi-span tiltrotor tests: (a) semi-span tests for the XV-15 in the NASA Ames 40 x 80 ft wind tunnel (Ref. 17), (b) semi-span tests on an in-house small scale wind tunnel model (Ref. 2).

2.6.1 XV-15

Validation results are presented in this section for a full-scale Bell XV-15 rotor, tested in a semi-span configuration in the NASA Ames 40 x 80 ft wind tunnel. The important model parameters of the Bell XV-15 rotor and wing are tabulated in Tables 2.1 and 2.2. The damping of the wing beamwise bending mode as a function of airspeed is shown in Fig. 2.6 for an elastic blade analysis by Johnson [18], a rigid blade analysis by Hathaway [1], the present analysis, and test data (from Ref. 17). All three analyses predict the stability boundary at around 330 knots. Figures 2.7 and 2.8 show the same comparisons for wing chordwise bending and wing torsion modes, respectively. Only two data points are available for the chordwise bending, and the data points for the torsion have significant scatter. From Figures 2.6, 2.7, and 2.8 we conclude that the present analysis provides stability predictions comparable to the test data and is in close agreement with the analysis presented by Johnson and Hathaway.

Table 2.1: XV-15 Rotor properties (from Ref. 17).

Number of blades, N	3
Radius, R	12.5 ft
Lock number, γ	3.83
Solidity, σ	0.089
Lift curve slope, $c_{l\alpha}$	5.7
Rotor speed, Ω	458 RPM
Pitch-flap coupling, K_P	-0.268
Blade inertias	
I_b	105 $slug - ft^2$
I_β^*	1.0
$I_{\beta 0}^*$	0.779
I_ζ^*	0.670
$I_{\zeta 0}^*$	1
I_0^*	1.0
$I_{\beta\alpha}^*$	1.0
$I_{\zeta 0\alpha}^*$	1
S_ζ^*	1.035
$S_{\beta 0}^*$	1.212
M_b^*	6.160
Blade frequencies	
ν_β	$\left[1 + 0.0355\left(\frac{600}{\Omega R}\right)\right]^{1/2}$
$\nu_{\beta 0}$	1.85

Table 2.2: XV-15 wing properties (from Ref. 20).

Element Number	#1 (root)	#2	#3	#4 (pylon)
Element length, $L(ft)$	4.55	4.55	4.55	3
I_θ $(slug - ft^2)$	1.0	1.0	1.0	$63.3\cos^2\Lambda$
S_α $(slug - ft^2)$	0.05	0.05	0.05	$9.09\cos\Lambda$
m $(slug/ft)$	1.0	1.0	1.0	14.54
EI_b $(lb - ft^2)$	3.13e7	3.13e7	3.13e7	3.13e7
EI_c $(lb - ft^2)$	8.48e7	8.48e7	8.48e7	8.48e7
GJ $(slug - ft^2)$	1.62e7	1.62e7	1.62e7	1.62e7
K_{bt} $(slug - ft^2)$	0	0	0	0
K_{ct} $(slug - ft^2)$	0	0	0	0
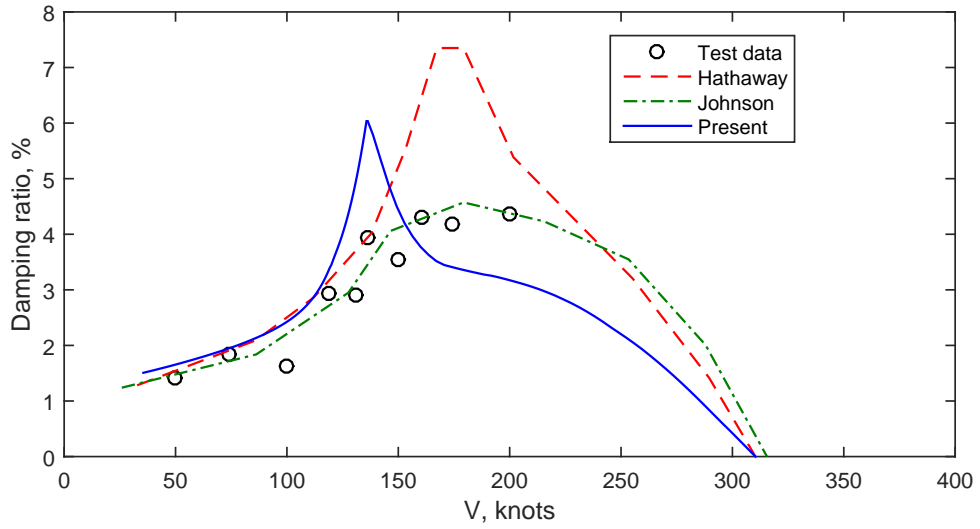
Figure 2.6: Semi-span XV-15 – Damping of wing beamwise bending mode vs airspeed.
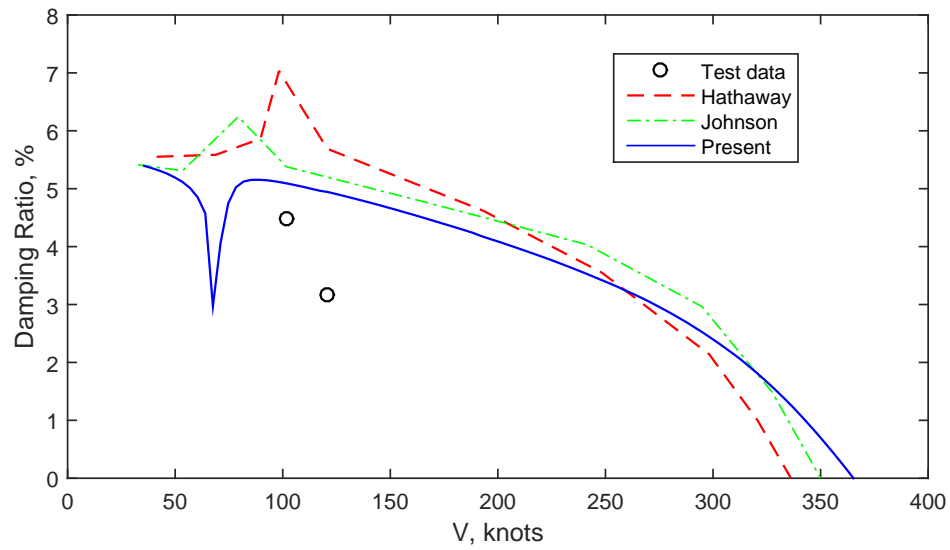
Figure 2.7: Semi-span XV-15 – Damping of wing chordwise bending mode vs airspeed.
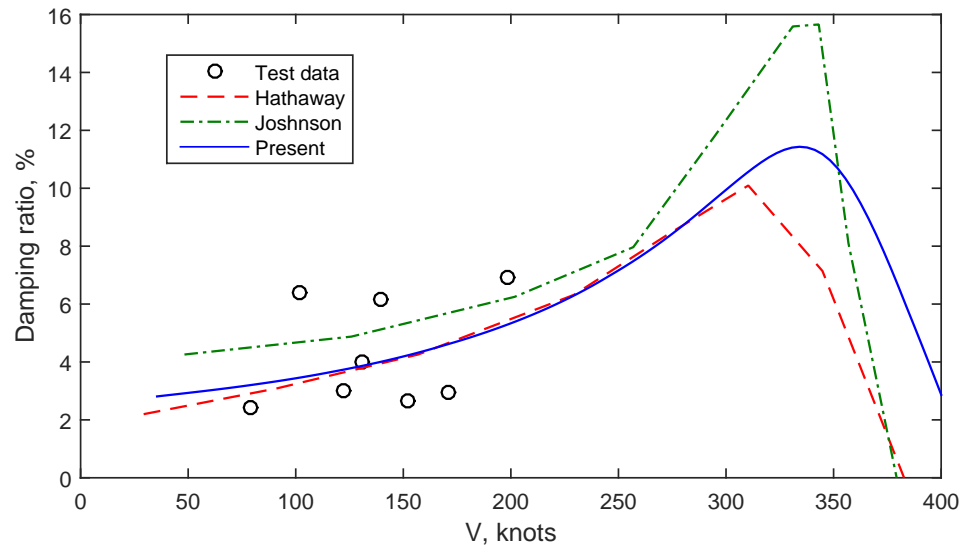
Figure 2.8: Semi-span XV-15 – Damping of wing torsion mode vs airspeed.

2.6.2 In-House Small-Scale Wind Tunnel Model

A semi-span wind tunnel tiltrotor whirl flutter model is designed and tested in the Penn State Hammond Low-Speed Wind Tunnel (Ref. 2), for validating the present analysis. The properties of the wing and rotor for two particular configurations titled Gen-3a and Gen-3b are tabulated in Tables 2.3 and 2.4. The damping of the wing modes for Gen-3a and Gen-3b is shown in Fig. 2.9. We can see from Fig. 2.9 that the predictions match well with the experiments.

Table 2.3: Rotor properties of Gen-3a and Gen-3b.

Item	Gen-3a	Gen-3b
Number of blades, N	3	3
Radius, R	8.05 in	8.55 in
Lock number, γ	3.22	3.70
Solidity, σ	0.102	0.096
Lift curve slope, $c_{l\alpha}$	5.7	5.7
Rotor speed, Ω	2000 RPM	2000 RPM
Pitch-flap coupling, K_P	-1.09	-1.09
Blade inertias		
I_b	8.9E-05 $slug-ft^2$	22.3E-05 $slug-ft^2$
I_β^*	1.0	1.0
$I_{\beta 0}^*$	0.779	1.0
I_ζ^*	0.670	1.0
$I_{\zeta 0}^*$	1	1.0
I_0^*	1.0	1.0
$I_{\beta\alpha}^*$	1.0	1.0
$I_{\zeta 0\alpha}^*$	1	1.0
S_ζ^*	1.035	1.0
$S_{\beta 0}^*$	1.212	1.0
M_b^*	6.160	6.160
Blade frequencies		
ν_β	$\left[1 + 0.0355\left(\frac{600}{\Omega R}\right)\right]^{1/2}$	$\left[1 + 0.0355\left(\frac{600}{\Omega R}\right)\right]^{1/2}$
$\nu_{\beta 0}$	3.60	3.72

Table 2.4: Wing properties of Gen-3a and Gen-3b.

|		
Semispan (in)	14.35	14.35
ω_b (Hz)	5.316	5.316
ω_c (Hz)	7.526	7.526
ω_t (Hz)	26.49	26.49

2.7 Summary

The equations governing the motion of a rotor/pylon system, are listed in (2.1 -2.6; 2.12 - 2.14). The coefficients of the DOFs appearing on the left-hand side of these equations are inertial properties of the rotor, and the terms appearing on the right-hand side of these equations are the aerodynamic forcing terms, which are dependent on the DOFs. A perturbational aerodynamic analysis is used to compute these forcing terms.

The wing is modeled using the finite element analysis. Cubic hermite polynomials are used for modeling the beamwise bending and chordwise bending, and the linear hermite polynomials are used for modeling torsion. The rotor hub forces and the aerodynamic forces by the winglet must be applied as generalized forcing terms in the finite element analysis.

The equations of motion are then assembled, resulting in a set of linear second-order set of differential equations. An eigenvalue analysis is performed on these equations to get the frequencies and damping of various modes.

The aeroelastic model is validated with experimental data from (a) semi-span tests for the XV-15 in the NASA Ames 40 x 80 ft wind tunnel, (b) semi-span tests on an in-house small scale wind tunnel model. The validation studies show that the aeroelastic model predictions are an agreement with the experimental data.
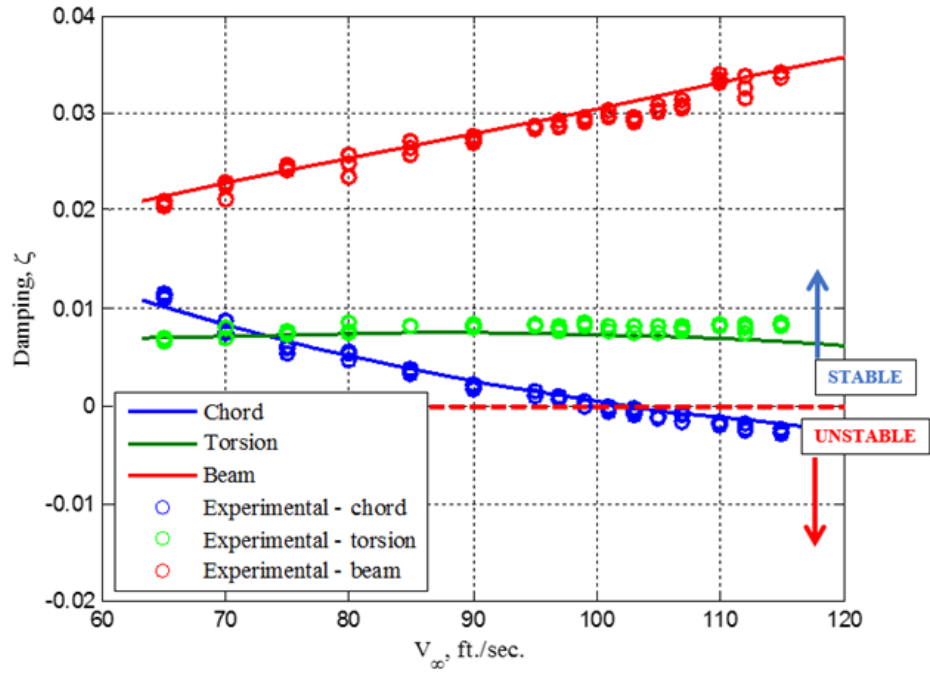
(a) Gen-3a.
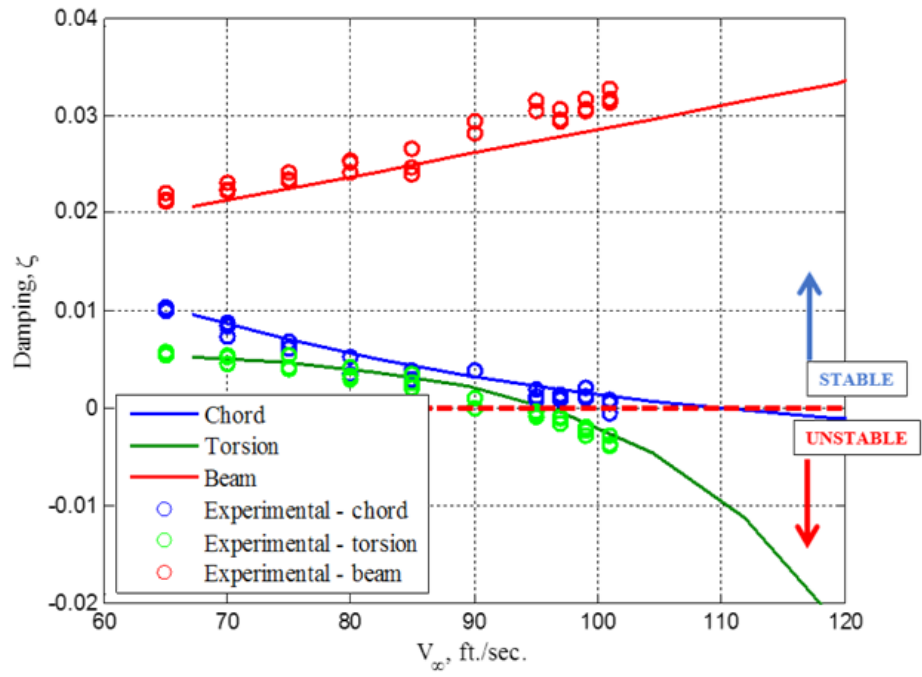
(b) Gen 3-b.

Figure 2.9: predicted and measured damping versus tunnel speed.

Chapter 3 |
Aeroelastic Parametric Studies and Aeroelastic Optimization

In this chapter, parametric studies are conducted on the influence of rotor blade torsion DOF, structural taper, composite couplings, wing spar twist, wing extension stiffness, and winglet planform variables on whirl flutter, using the aeroelastic model described in the previous chapter. The parametric studies are followed by an optimization study aiming at improving the whirl flutter speed. The design variables are wing parameters (stiffness, composite coupling, and taper), wing extension parameters (stiffness), and winglet parameters (toe, cant and sweep angles). Genetic algorithm (GA), a non-gradient based search method, is used for the optimization. The optimization study is validated using a comprehensive analysis code (Rotorcraft Comprehensive Analysis System, RCAS).

3.1 Parametric Studies

The baseline model for our study is the Bell XV-15 rotor on a soft torsion wing [7] with an extension and a winglet. The important rotor, wing, extension, and winglet parameters of the baseline model are tabulated in Tables 3.1 and 3.2. The inputs for the finite element analysis of the wing are given in Table 3.3, where L_e is the element length, S_α and I_{cg} are the first and second mass moments of inertia, respectively, m is the mass per length, Λ is the wing forward sweep angle and e is the distance of wing elastic axis from the aerodynamic center.

3.1.1 Rotor Blade Torsion DOF

The frequency of the blade torsion motion (ω_θ), in combination with the blade precone angle (β_p), can be destabilizing to whirl flutter. The influence of β_p on the damping of wing modes is shown in Fig. 3.1a, for $\beta_p = 0^o$ and 2.5^o (baseline). From Fig. 3.1a, we can see the destabilizing effect on wing damping for higher precone values. The influence of ω_θ on the damping of wing modes is shown in Fig. 3.1b for $\omega_\theta = 4.8$/rev (baseline) and no torsion ($\omega_\theta = \infty$). Results from the Figures 3.1a and 3.1b, which show the destabilizing nature of β_p and ω_θ, are consistent with previous studies (Ref. 18).

3.1.2 Structural Taper

Structural taper and wing extension are design features in the NASA LCTR2 [46]. The beam mode damping is increased from 4.5% to 6% when the taper ratio is changed from 1 to 0.1. This result has motivated us to investigate the effects of structural taper upon our model. In Fig. 3.2a, the wing modes damping is plotted for an untapered and a tapered wing, without the wing-tip devices. The whirl flutter speed is increased slightly, by about 10 knots, for the case with the tapered wing. With the wing wing-tip devices on, the whirl flutter speed is increased by 45 knots (Fig. 3.2b) for the tapered wing case, when compared to the untapered wing.

Structural taper increases the tip deflection. The efficiency of the wing extensions in improving the beam mode damping increases with tip deflection. The mode shapes with and without taper (normalized by the root bending curvature) are plotted in Fig. 3.3, where we can see that the tapered wing has a higher tip deflection than the untapered wing. Thus we can conclude that structural taper, when combined with wing-tip devices, can help increase the beam mode damping.

3.1.3 Composite Coupling

Composite tailoring of wing can introduce coupling between bending and torsional modes. ϵ_{bt} and ϵ_{ct} are the non-dimensional values of the bending torsion coupling of beam and chord modes, respectively, defined by

$$\epsilon_{bt} = \frac{K_{bt}}{\sqrt{EI_b GJ}} \quad ; \quad \epsilon_{ct} = \frac{K_{ct}}{\sqrt{EI_c GJ}} \tag{3.1}$$

Fig. 3.4 shows the effect of beamwise bending torsion coupling on the bending and torsion modes. Positive values of ϵ_{bt} bring the frequencies of beam and torsion modes closer, and stabilize the beam mode while destabilizing the torsion mode.

Fig. 3.5 shows the effect of chordwise bending torsion coupling. Positive values of ϵ_{ct} separates the frequencies of chord and torsion modes, and stabilize the chord mode while destabilizing the torsion mode. These results are that of a structurally untapered wing, and are consistent with previous studies (Ref. 7 and Ref. 47).

The effect of tapering the wing combined with composite tailoring are shown in Fig. 3.6. From Fig. 3.6, we can see that stability boundary of the beam and chord modes is increased by an exchanged damping between between torsion modes and beam/chord modes.

3.1.4 Twisted Wing Spar

Twisting the wing spar introduces an elastic coupling between beam and chord modes. The moment-curvature relationship of a wing spar twisted by an angle θ_1 is given by:

$$
\begin{bmatrix} M_x \\ M_y \\ M_z \end{bmatrix} = \begin{bmatrix} EI_b \cos^2 \theta_1 + EI_c \sin^2 \theta_1 & (EI_c - EI_b) \cos \theta_1 \sin \theta_1 & 0 \\ (EI_c - EI_b) \cos \theta_1 \sin \theta_1 & EI_c \cos^2 \theta_1 + EI_b \sin^2 \theta_1 & 0 \\ 0 & 0 & GJ \end{bmatrix} \begin{bmatrix} w''(z) \\ v''(z) \\ \phi'(z) \end{bmatrix} \quad (3.2)
$$

where the term $(EI_c - EI_b) \cos \theta_1 \sin \theta_1$ couples the beam and chord modes. Fig. 3.7 shows this coupling effect on an untapered wing. Positive values of θ_1 stabilizes the chord mode while destabilizing the beam mode, and vice-versa. Thus we can tailor the wing taper and twist to get the optimum flutter speed.

3.1.5 Influence of a Soft Wing Extension

Reducing the stiffness of the wing extension significantly (0.2% of its baseline value) can stabilize the beam mode. Fig. 3.8a shows the damping of the beam mode for the baseline case (unstable at 285 kts) and the soft wing extension case (stable mode). The mode shapes of this beam mode for the baseline and soft wing extension case are shown in Fig. 3.8b, where the non-dimensional vertical deflection (w) is plotted against span. The softer wing extension has a higher value of vertical

deflection when compared to the baseline value, and hence provides the additional damping required to stabilize the beam mode.

3.1.6 Parametric Study of Extension Sweep Angle and Aft Offset

The wing extension with an aft offset (d_{ex}) and sweep (Λ) (schematic shown in Fig. 3.9) can couple the beam and torsion modes, and has a significant influence on stability. The potential benefits of a swept extension with an aft offset are discussed in [27].

The damping of the beam and torsion modes are plotted in Fig. 3.10 for different offset values. Introducing an aft offset ($d_{ex} = 1$ ft) stabilizes the torsion mode while destabilizing the beam mode. This is because the beam mode shape has a flap-up nose-up type coupling – which implies that the extension, when located aft of the wing, creates a perturbation force in the direction of the wing vertical deflection – thus destabilizing the beam mode. Introducing a fore-offset ($d_{1ex} = -1$ ft, impractical for tiltrotors) can stabilize the beam mode, as it creates a perturbation force opposing the motion of the wing.

Similar results can be obtained for extension sweep (see Fig. 3.11), where having a swept back extension (sweep $= 30^o$) creates a perturbation force in the direction of the wing deflection, due to the flap-up nose-up type coupling, thus destabilizing the beam mode. Having a swept forward extension (sweep $= -30^o$, impractical for tiltrotors) creates a perturbation force opposing the deflection – thus stabilizing the beam mode.

3.1.7 Parametric Study of Winglet Cant Angle

The effects of winglet cant angle on whirl flutter are studied here (shown in Fig 3.12). Decreasing the cant angle increases the wing span, which provides additional damping to the wing – increasing the stability of the beam and torsion modes. The chord mode, on the other hand is not affected by the cant angle.

Table 3.1: Rotor and wing properties.

Rotor	
Number of blades	3
Radius (R) (ft)	12.5
Lock number	3.83
Solidity	0.089
Blade flapping inertia (slug-ft^2)	105
Lift curve slope	5.7
Pitch-flap coupling	-0.268
Tip speed (ft/sec.)	600
Rotational speed (Ω) (rad/sec.)	48

Wing (Semi-span)	
Span (L/R)	1.333
Chord (c/R)	0.413
Mast height (h/R)	0.342

Table 3.2: Wing extension and winglet properties.

Wing Extension	
Length	4.55 (ft) (27% of wing span)
Chord	5.16 (ft) (100% wing chord)
Stiffness	50% of wing
Inertia	50% of wing

Winglet	
Length	4.55 (ft) = 27% of wing span
Chord	2.58 (ft) = 50% wing chord
Cant angle	45°
Sweep angle	45°
Toe	0°
Inertia	25% of wing
Stiffness	25% of wing

Table 3.3: Wing properties used for FEA.

| Element Number	#1 (root)	#2	#3	#4 (pylon)
$L_e(ft)$	4.55	4.55	4.55	3
$I_{cg}\ (slug - ft^2)$	1.0	1.0	1.0	$63.3\cos^2\Lambda$
$S_\alpha\ (slug - ft^2)$	0.05	0.05	0.05	$9.09\cos\Lambda$
$m\ (slug/ft)$	1.0	1.0	1.0	14.54
$EI_b^0\ (lb - ft^2)$	3.13e7	3.13e7	3.13e7	3.13e7
$EI_c^0\ (lb - ft^2)$	8.48e7	8.48e7	8.48e7	8.48e7
$GJ^0\ (slug - ft^2)$	0.81e7	0.81e7	0.81e7	0.81e7
e/c	0.051	0.051	0.051	0.0
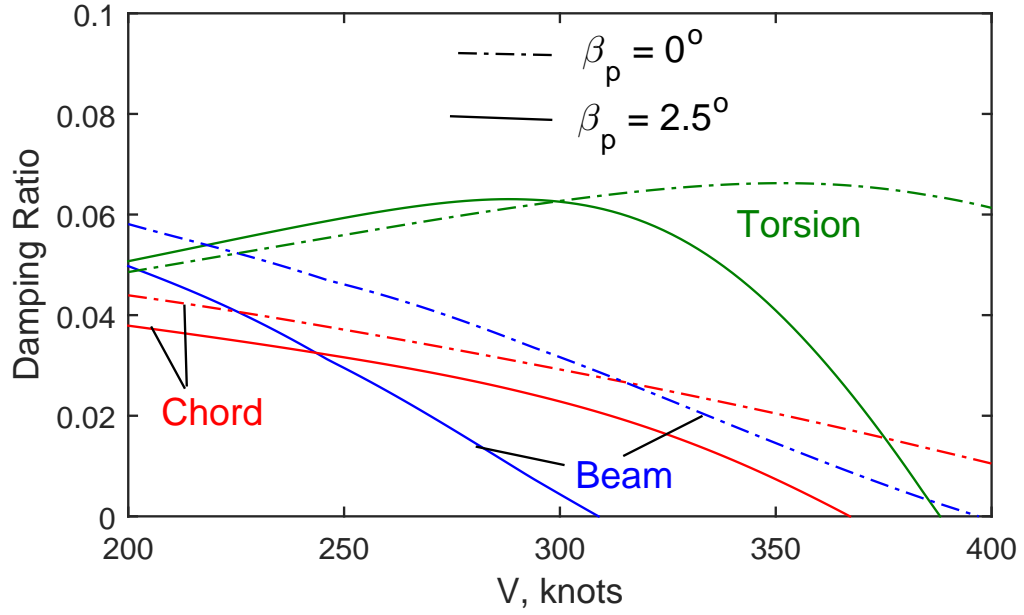
(a) Effect of rotor precone (β_p).
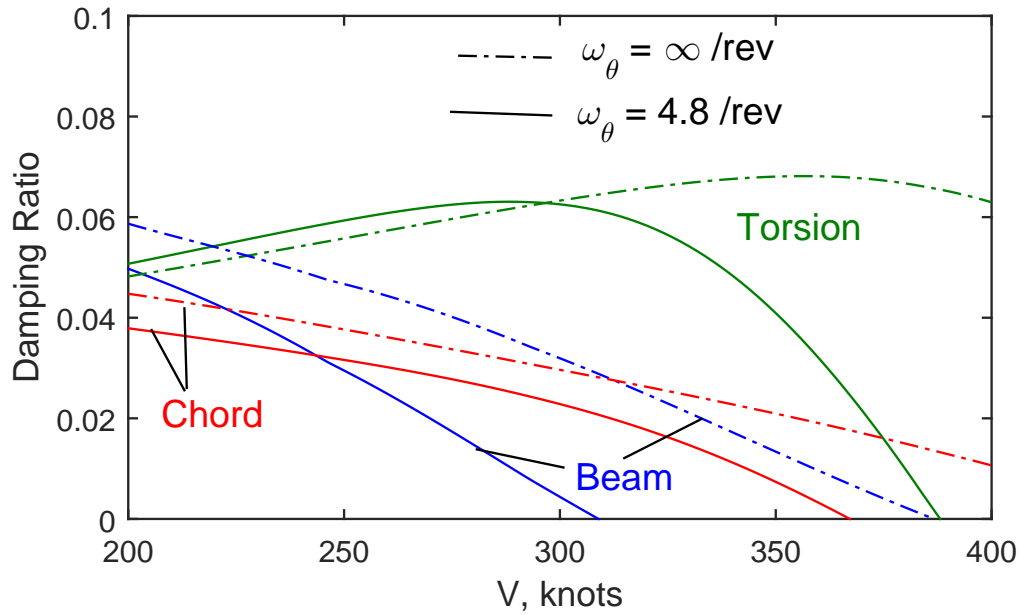
(b) Effect of control system stiffness (ω_t).

Figure 3.1: Damping of wing modes for different values of β_p and ω_θ.
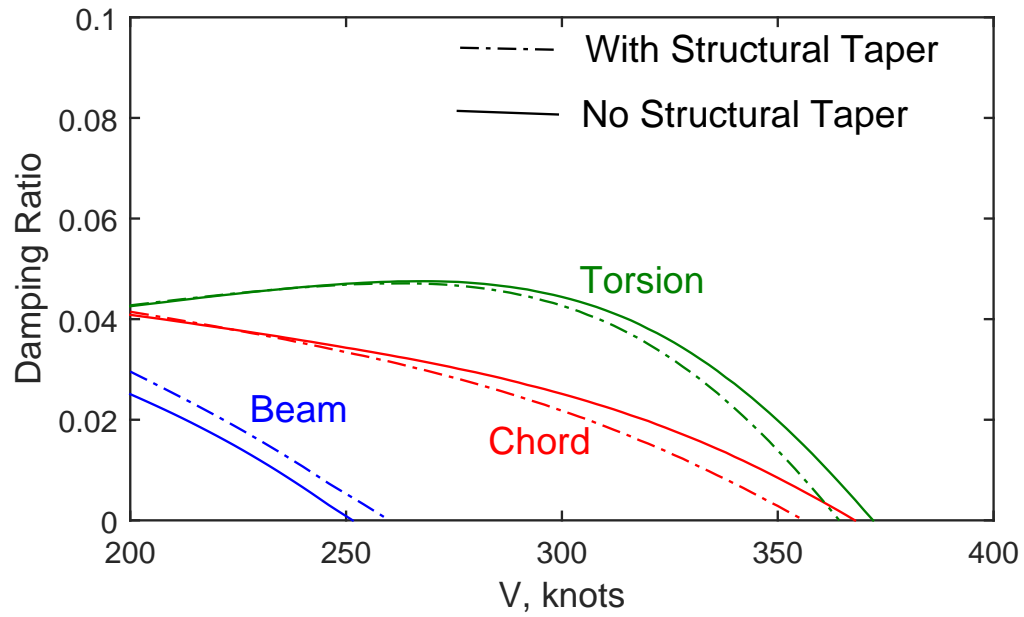
(a) Without wing extension and winglet.
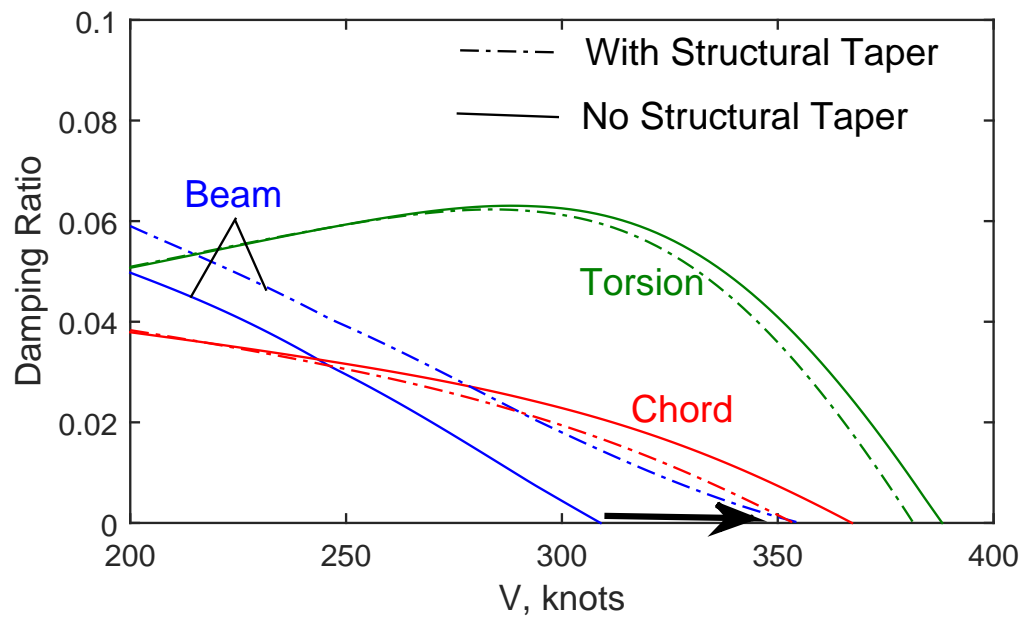
(b) With wing extension and winglet.

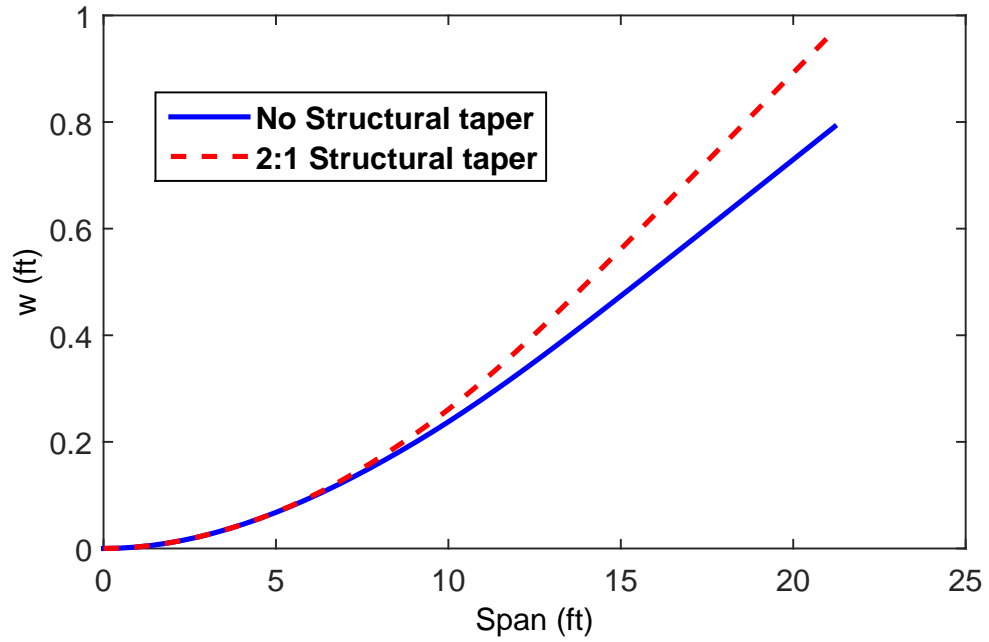Figure 3.2: Effects of structural taper on wing modes damping.

Figure 3.3: Mode shapes with and without structural taper.

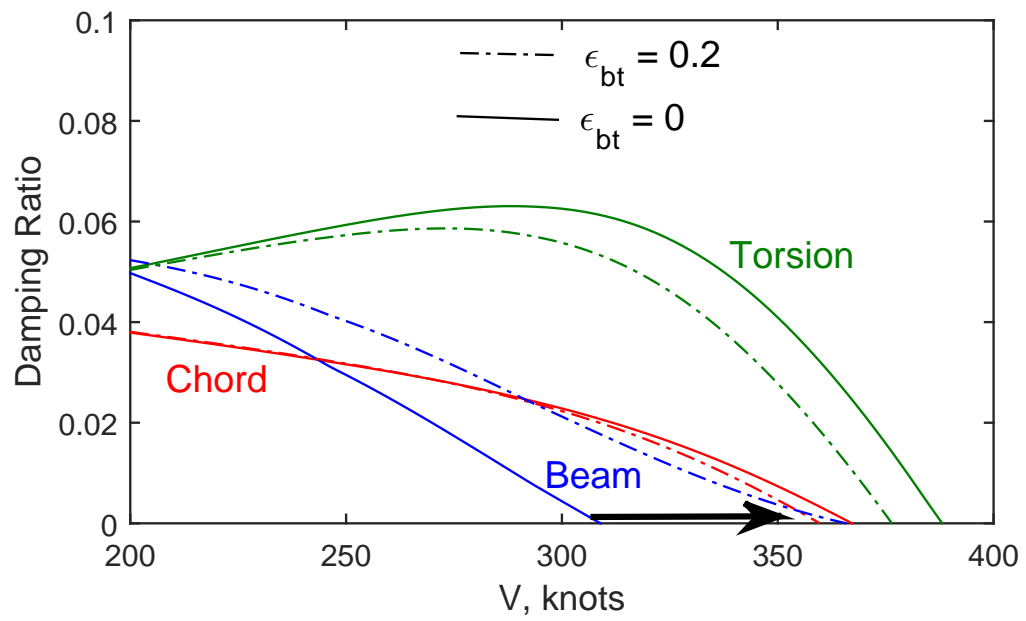Figure 3.4: Effects of composite coupling on wing modes damping.
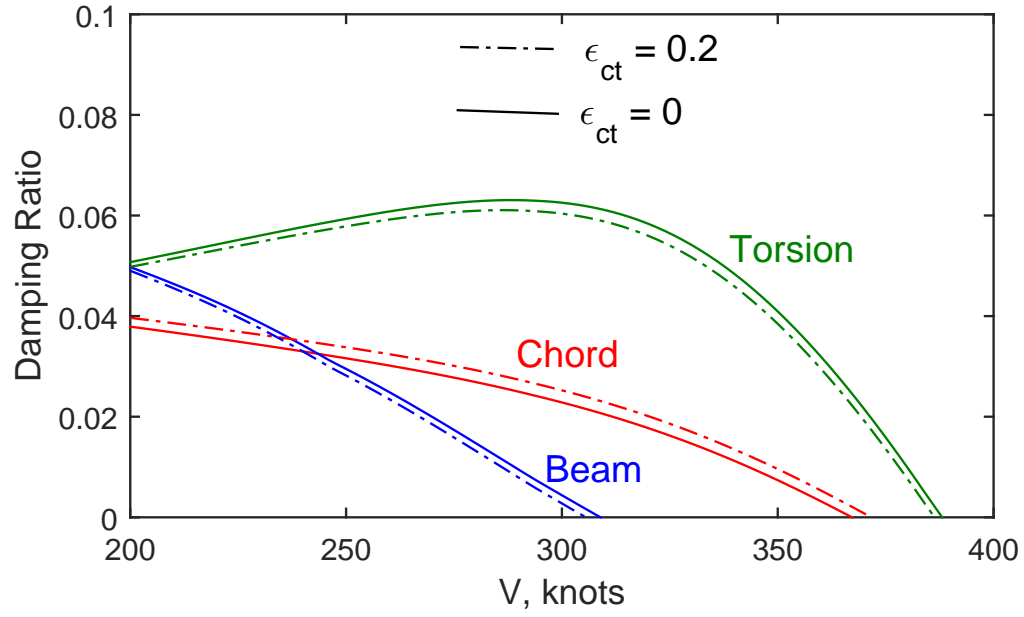
Figure 3.5: Effects of composite coupling on wing modes damping.
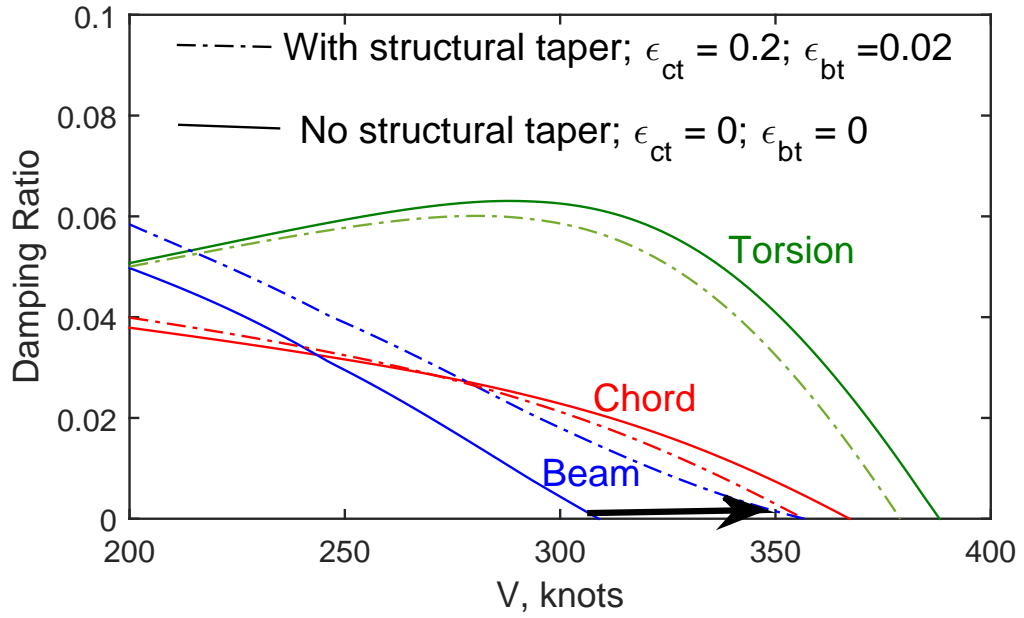
Figure 3.6: Effects of structural taper and composite coupling on wing modes damping.
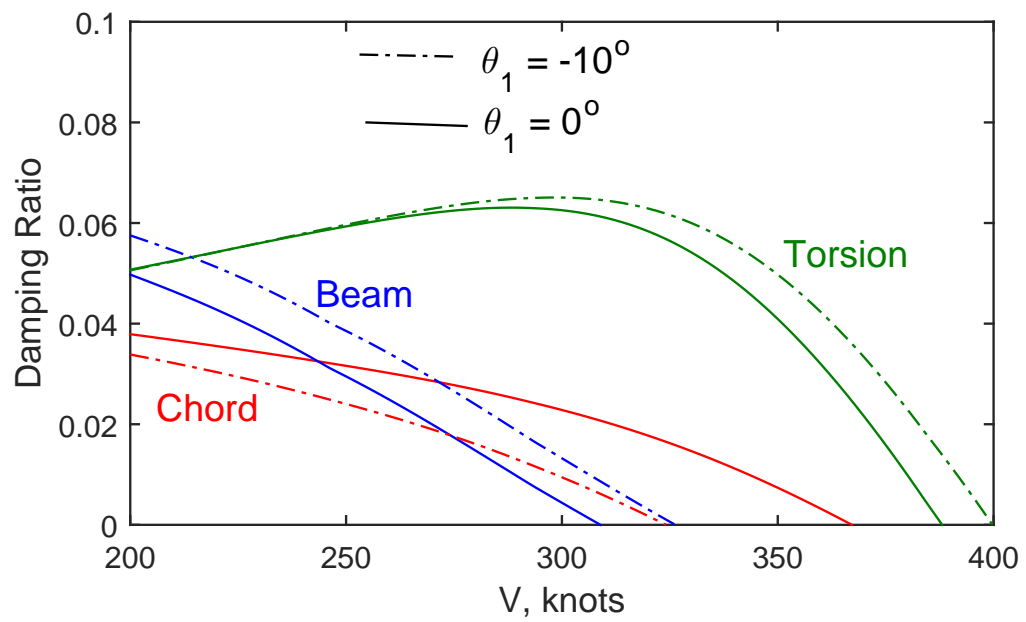
Figure 3.7: Effects of a twisted main wing spar on wing modes damping.
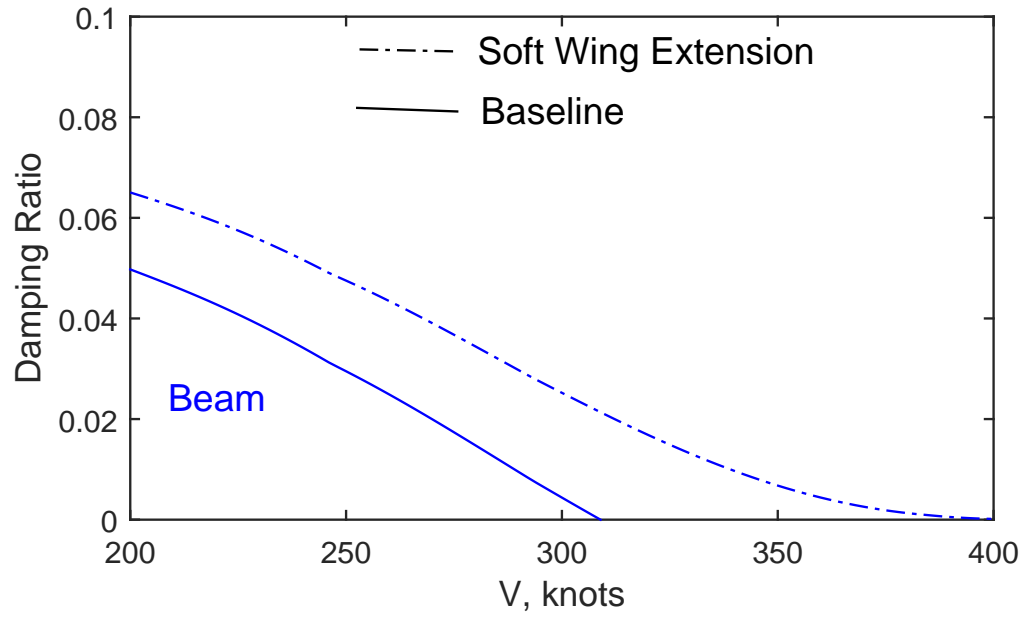
(a) Damping.
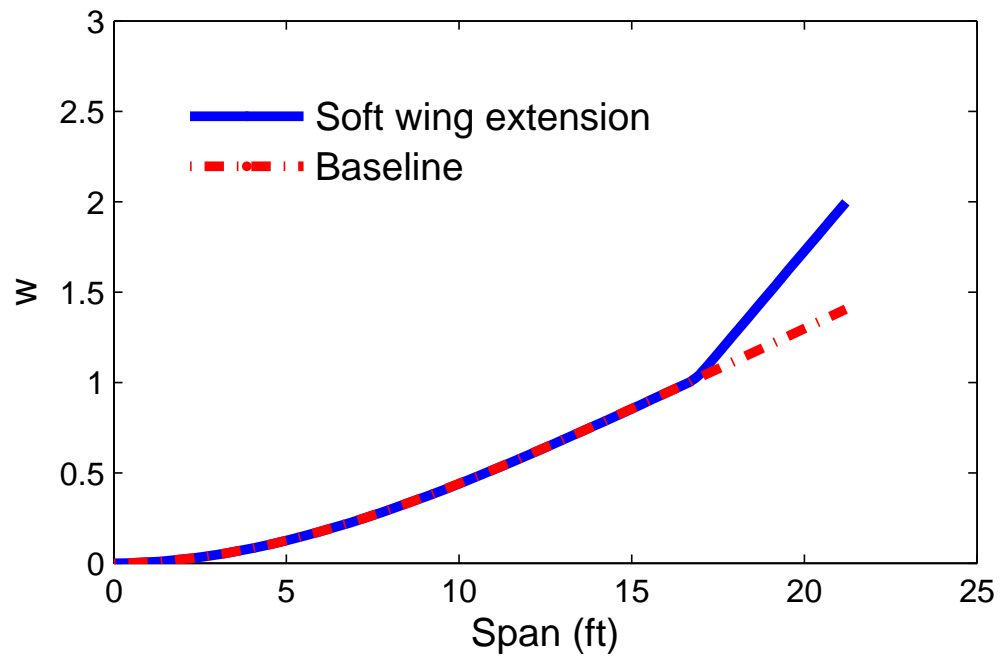
(b) Mode shape of the beam mode.

Figure 3.8: Effects of a soft wing extension on damping and mode shape.
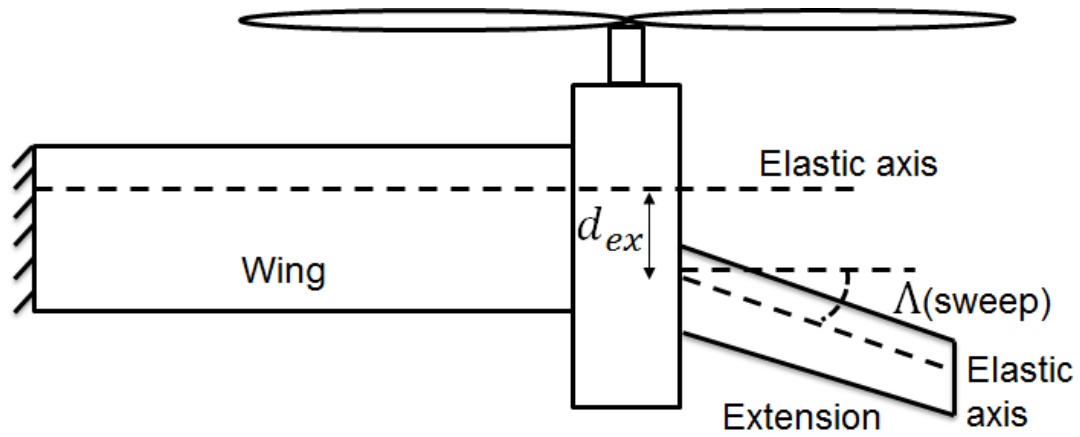
Figure 3.9: A schematic of a swept extension with an offset.
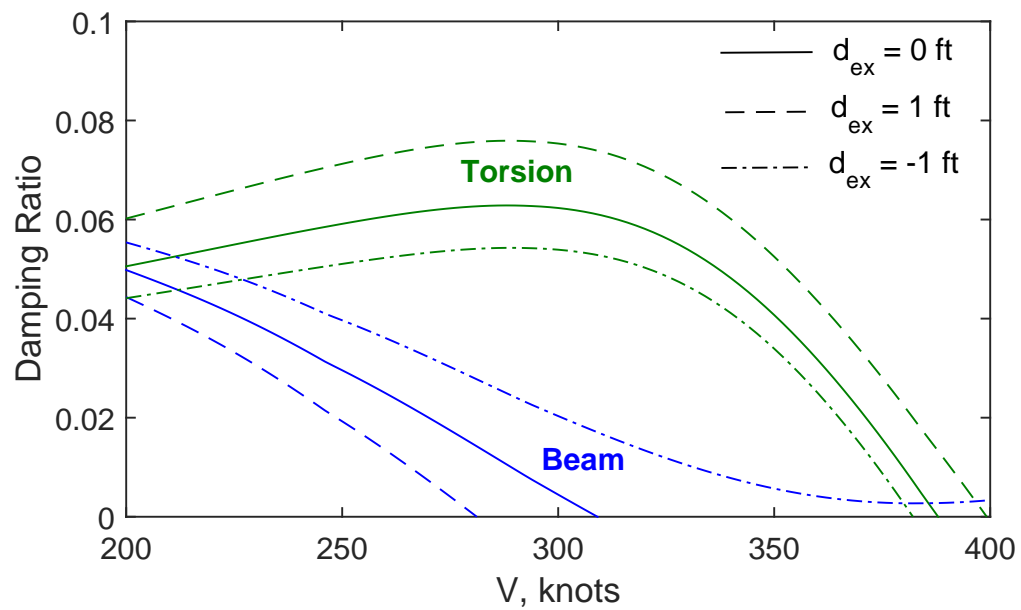
Figure 3.10: Damping of beam and torsion modes for different offset values.
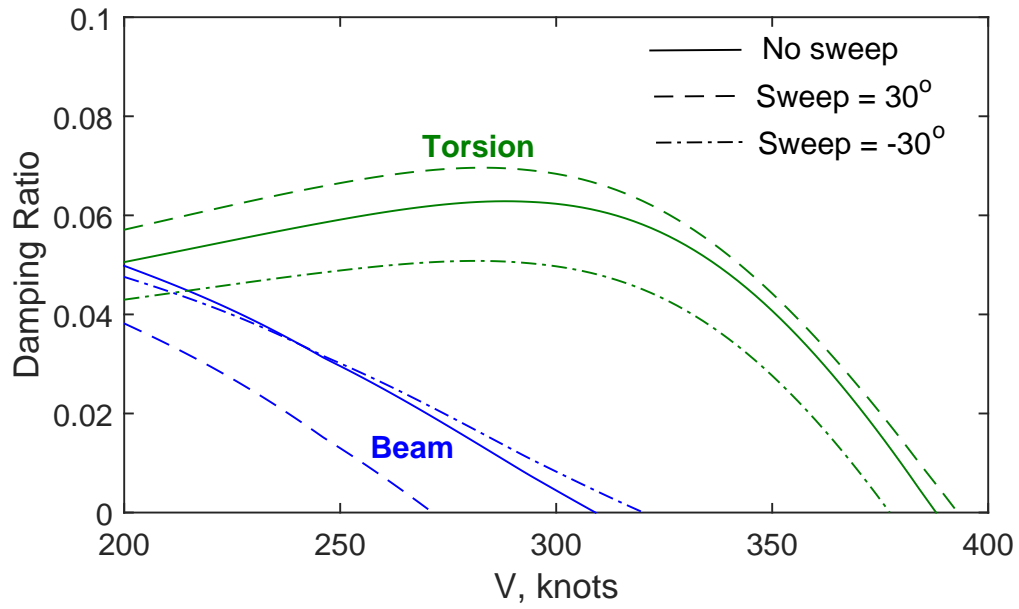
Figure 3.11: Damping of beam and torsion modes for different extension sweep values.
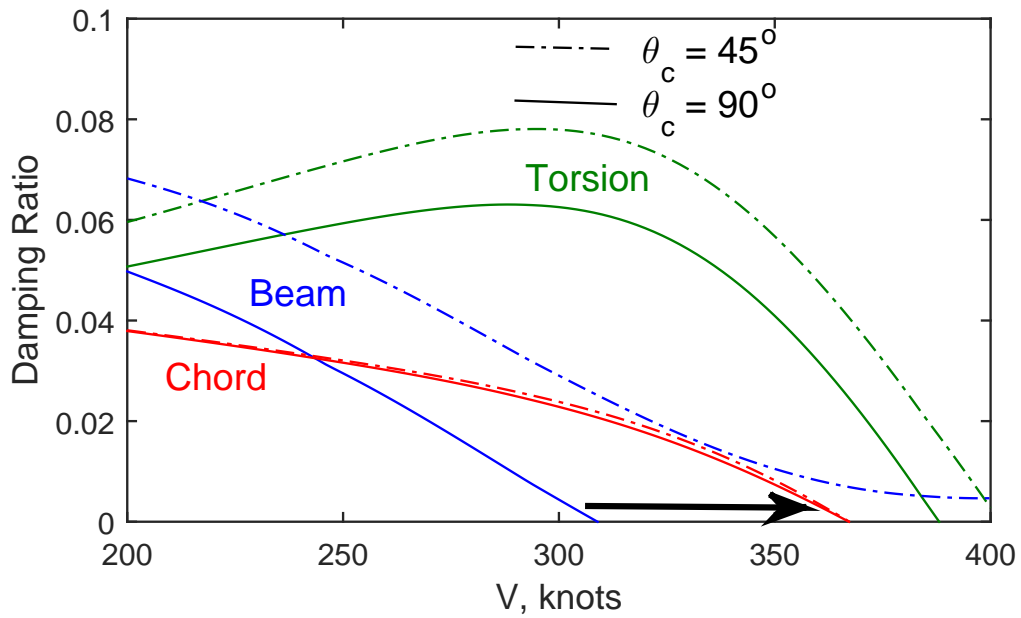
Figure 3.12: Effects of winglet cant angle on the damping of beam and torsion modes.

3.2 Aeroelastic Optimization

The parametric studies helped us understand the influence of many parameters that influence whirl flutter (wing stiffness, taper, composite coupling, and wing-tip devices). This motivated us to conduct an optimization study to improve the aeroelastic stability of the aircraft by identifying the optimal combinations of the aforementioned parameters.

The objective of the aeroelastic optimization is to maximize the whirl flutter speed. The schematic of the wing, extension, and winglet is shown in Fig. 3.13. The inboard wing is divided into three sections and the outboard wing is divided into an extension and a winglet. The design variables for the optimization are the stiffness values in sections 2 and 3 ($EI_b, EI_c, GJ, \epsilon_{bt}, \epsilon_{ct}$), wing spar twist, extension sweep, extension aft offset, and winglet cant angle. Genetic algorithm is used for the optimization [48]. Constraints are placed on these design variables in the form of upper and lower bounds.

The baseline, bounds, and optimum values of the design variables are tabulated in Table 3.4 (EI_b^0, EI_c^0, and GJ_0 are the baseline stiffness values). The damping ratios of the wing modes for the baseline are shown in Fig. 3.14. The whirl flutter speed of the baseline design is 310 knots (beam mode). Since GA is used for the optimization, multiple optimal designs can be obtained in the analysis. The parameters of two optimal designs (Optimized-A and Optimized-B) are tabulated in Table 3.4. The damping ratios of the wing modes for Optimized designs A and B are shown in Fig. 3.14 and Fig. 3.15, respectively. The flutter speed of the optimized design is 65 knots greater than the baseline.
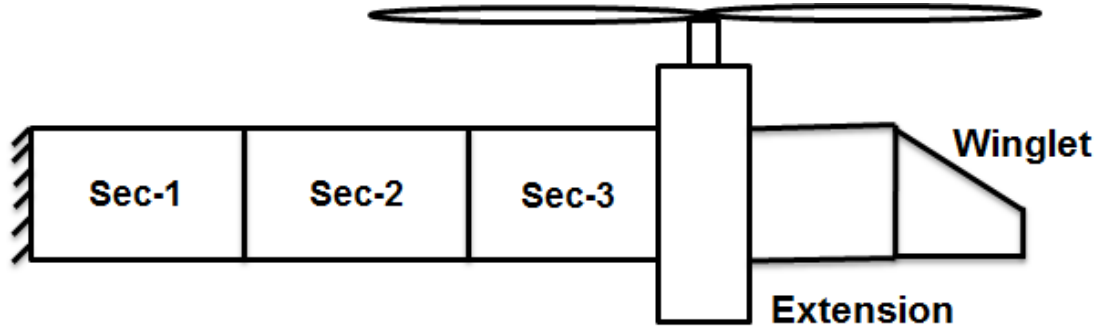
Figure 3.13: Schematic of the wing, extension, and winglet.

Table 3.4: Design variables of baseline, Optimized-A, and Optimized-B designs

Item	Min/Max	Baseline	Optimized-A	Optimized-B
ϵ_{bt}	-0.2/0.2	0	-0.05	-0.07
ϵ_{ct}	-0.2/0.2	0	0.19	-0.05
Spar twist	$0^o/10^o$	0°	2.9^o	6.3^0
		Wing Section-2		
EI_b/EI_b^0	0.5/1	1	0.84	0.89
EI_c/EI_c^0	0.5/1	1	0.84	0.89
GJ/GJ^0	1	1	1	0.63
		Wing Section-3		
EI_b/EI_b^0	0.5/1	1	0.80	0.89
EI_c/EI_c^0	0.5/1	1	0.80	0.89
GJ/GJ^0	0.5/1	1	0.95	0.91
		Extension and Winglet		
Extension sweep	$0^o/25^o$	0°	5°	5°
Extension aft offset (ft)	0/4	0	0	0.4
Winglet cant angle	$60^o/90^o$	90°	68.7^o	60°
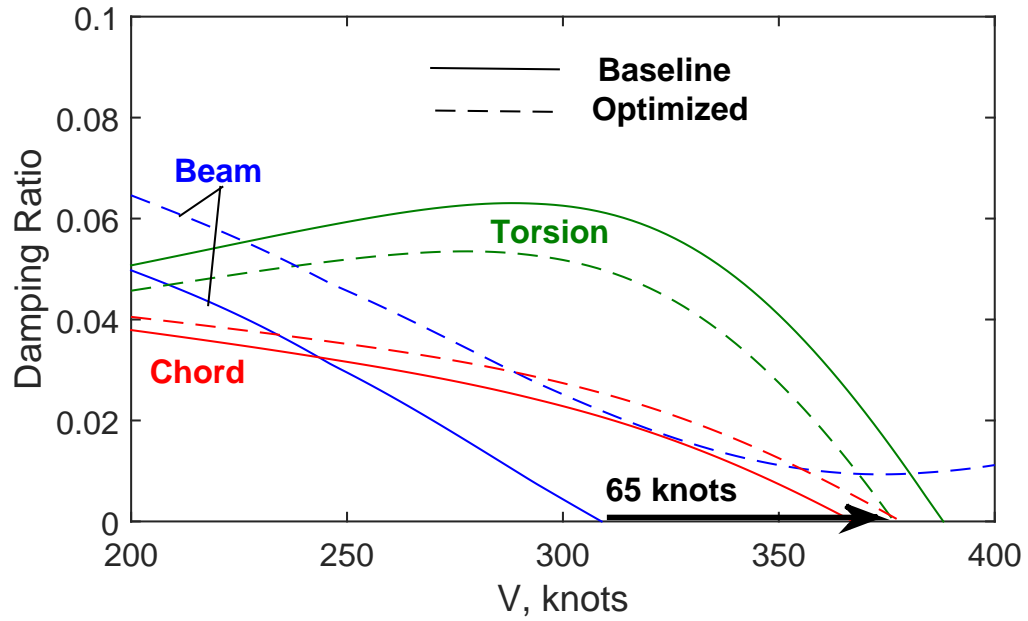
Figure 3.14: Damping Ratios of Baseline and Optimized-A designs.
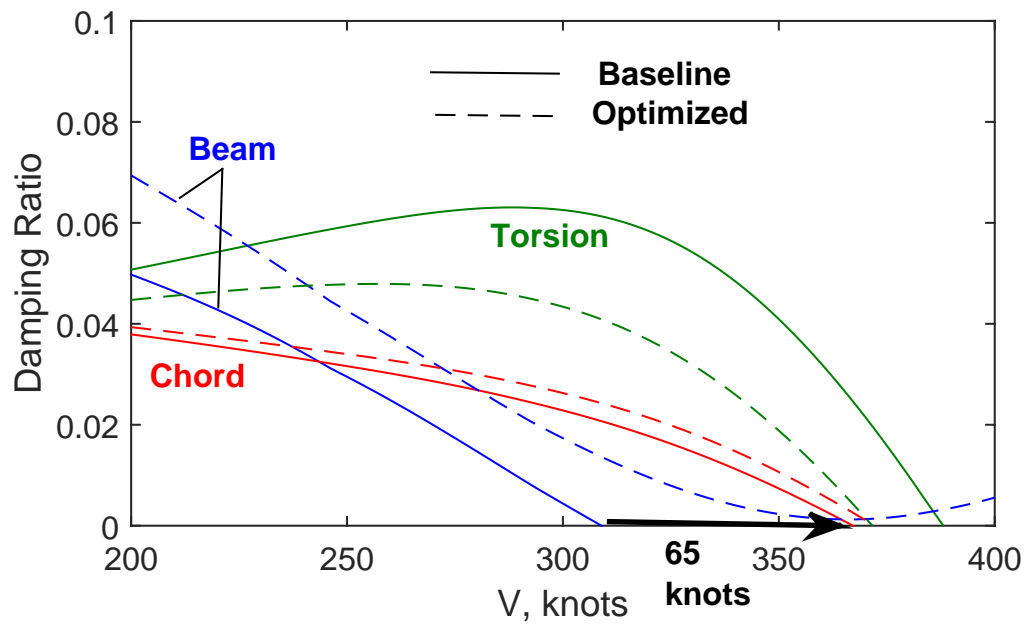
Figure 3.15: Damping Ratios of Baseline and Optimized-B designs.

The optimization results obtained by freezing certain design variable is studied here. Firstly, the bending-torsion coupling variables (ϵ_{bt}, ϵ_{ct}) are set to zero in order to investigate the effects of composite coupling. The resulting optimal design variables (Optimized-C) are tabulated in Table 3.5. The damping ratios of the wing modes are plotted in Fig. 3.16. From Fig. 3.16, we can see that the optimum design has an improved flutter speed of 375 knots (a 65 knot increase). These results show that the flutter speed of Optimized-A and Optimized-B, which have composite couplings, have the same flutter speed as Optimized-C, which has no composite coupling.

Next the cant angle held fixed at 90 degrees to investigate the effects of the outboard wing span. The resulting optimal design variables (Optimized-D) are tabulated in Table 3.5. The damping ratios of the wing modes are plotted in Fig. 3.17 where we can see that the optimized design has a 60 knot increase in flutter speed.

Table 3.5: Design variables of Optimized-C and Optimized-D designs.

| Item	Min/Max	Baseline	Optimized-C	Optimized-D
ϵ_{bt}	-0.2/0.2	0	0	-0.1
ϵ_{ct}	-0.2/0.2	0	0	0.13
Spar twist	$0^o/10^o$	0°	8.6^o	2.3^0
Wing Section-2				
EI_b/EI_b^0	0.5/1	1	1	0.5
EI_c/EI_c^0	0.5/1	1	1	0.5
GJ/GJ^0	1	1	0.96	0.95
Wing Section-3				
EI_b/EI_b^0	0.5/1	1	0.76	0.5
EI_c/EI_c^0	0.5/1	1	0.76	0.5
GJ/GJ^0	0.5/1	1	0.76	0.96
Extension and Winglet				
Extension sweep	$0^o/25^o$	0°	5°	6.4^o
Extension aft offset (ft)	0/4	0	0	0.53
Winglet cant angle	$60^o/90^o$	90°	63.6^o	90°

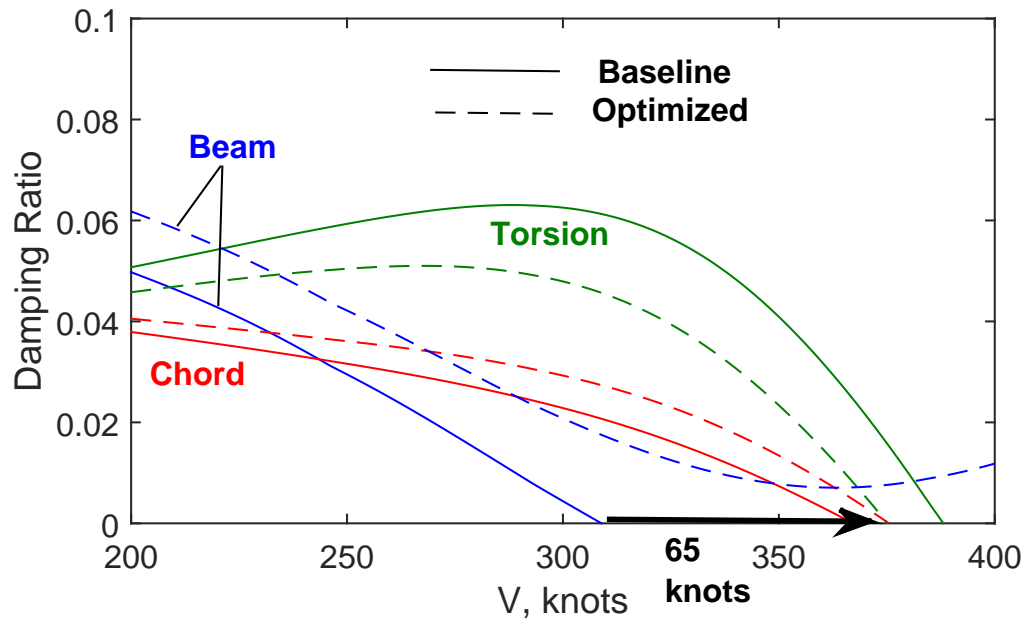Figure 3.16: Damping Ratios of Baseline and Optimized-C designs.
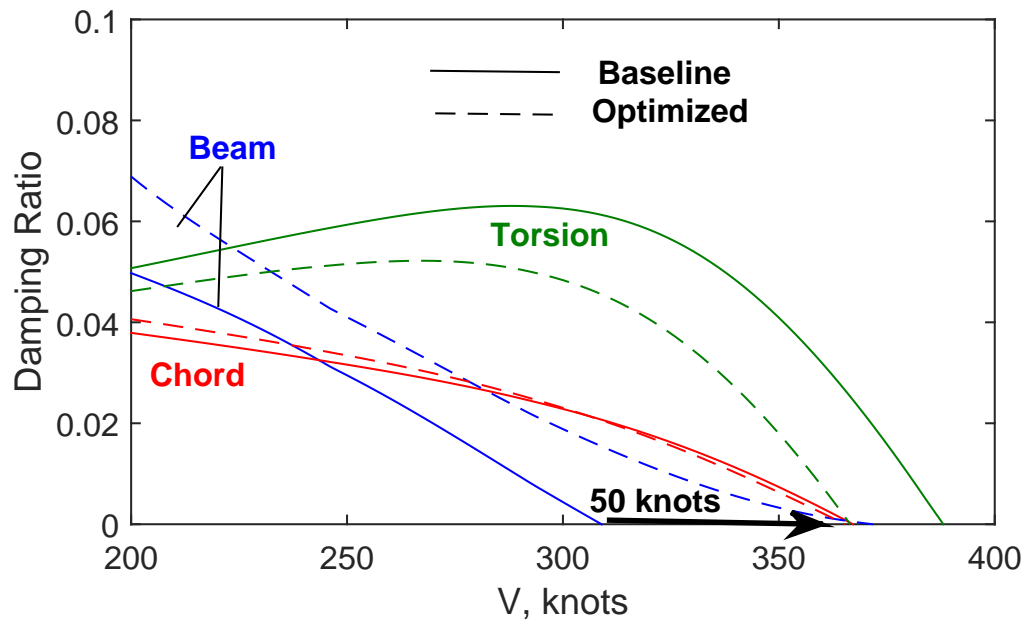

Figure 3.17: Damping Ratios of Baseline and Optimized-D designs.

3.3 Validation of the Aeroelastic Optimization using RCAS

The optimization is validated using a software called Rotorcraft Comprehensive Analysis System (RCAS), which is an ongoing effort by the US Army Aeroflightdynamics Directorate at Ames Research Center to provide rotorcraft modeling and analysis technology [49].

RCAS uses finite element modeling for structural analysis, using a non-linear beam element with ten DOFs per element. RCAS also has the capability of modeling hinges, linear and torsional springs and dampers. The aerodynamic analysis uses linear steady and unsteady, quasi-steady airfoil table lookup, and vortex shedding methods. The rotor disc inflow is modeled using dynamic inflow methods. The aeroelastic stability analysis is performed by perturbing the system about the equilibrium state.

In this section, the optimization studies are validated using RCAS. A comprehensive model of an elastic wing with an extension and a winglet, and a rigid gimballed rotor is developed in RCAS for this purpose. Since the rotor model developed in RCAS is that of a rigid rotor, the lag and torsion frequencies are set to infinity in the analytical model ($\nu_\zeta = \omega_\theta = \infty$).

First, a parametric study of the extension and winglet on the damping of the wing modes computed using the developed aeroelastic analysis and RCAS is studied. In Fig. 3.18 the damping of the beam mode is shown. The analysis predicts that adding an extension and a winglet increases the damping by approximately 2%, and increases the flutter speed by approximately 20 knots. The results obtained using RCAS show that the extension and a winglet increases the damping by approximately 2%, and increases the flutter speed by approximately 25 knots – agreeing well with the analysis. In Fig. 3.19 the damping of the torsion mode is shown, where we can see that the extension increases the damping by approximately 1%. The results obtained by RCAS predict that the extension increases the damping by more than 2%.

Next, the optimization is performed again for the rigid rotor. The baseline and optimized (Optimized-E) design variables are tabulated in Table 3.6. Note that the baseline design already has an extension and a winglet; and the baseline and

optimized designs have no composite couplings. The damping ratios of the wing for the baseline and optimized designs, calculated using the developed aeroelastic analysis and RCAS, are shown in Fig. 3.20. In Fig. 3.20, we can see that analysis predicts that the optimized design has approximately 3% more damping, and a 25-knot increase in the flutter speed than the baseline. The results obtained using RCAS agree well with the present analysis, showing that the optimized design has approximately 3% more damping as well as a 25-knot increase in flutter speed than the baseline design – agreeing well with the analysis.
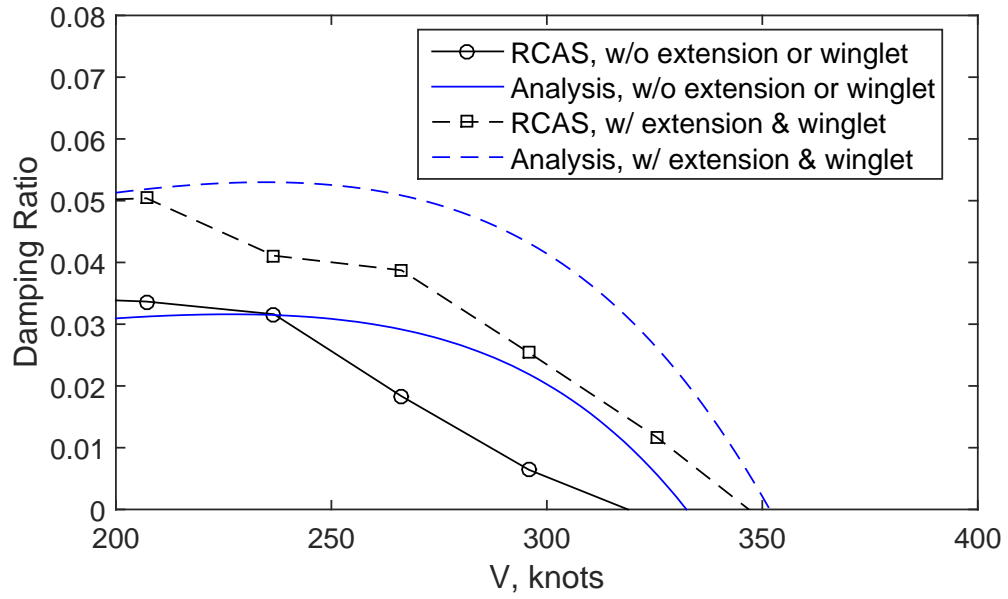
Figure 3.18: Damping ratios with and without wing-tip devices for the beam mode.
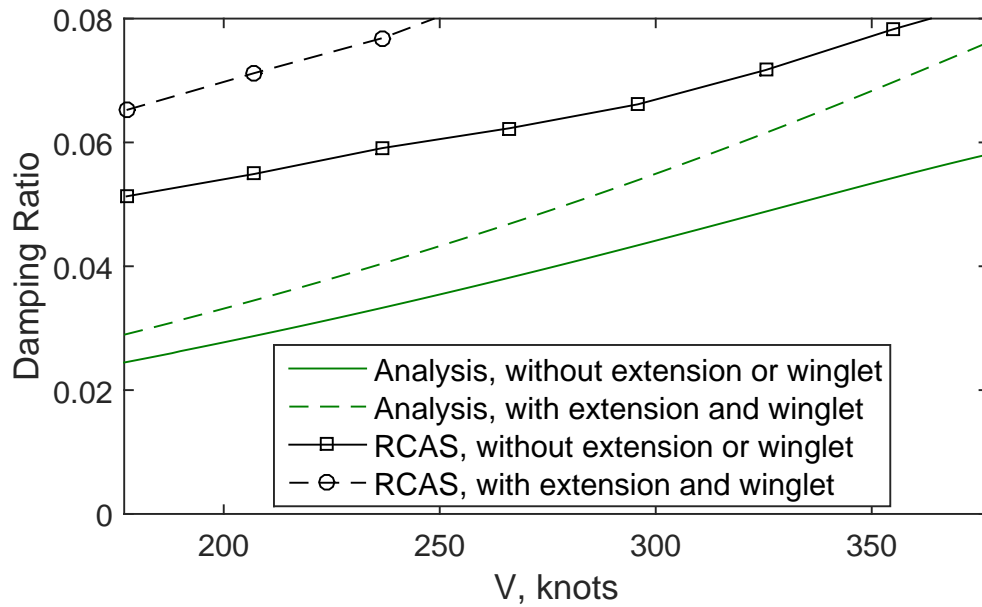
Figure 3.19: Damping ratios with and without wing-tip devices for the torsion mode.

Table 3.6: Design variables of baseline and Optimized-E designs for the rigid rotor model for validation in RCAS.

Item	Min/Max	Baseline	Optimized-E
ϵ_{bt}	0/0	0	0
ϵ_{ct}	0/0	0	0
Spar twist	$0^o/10^o$	0°	-7.2^o
Wing Section-2			
EI_b/EI_b^0	0.5/1	1	0.61
EI_c/EI_c^0	0.5/1	1	0.61
GJ/GJ^0	1	1	1
Wing Section-3			
EI_b/EI_b^0	0.5/1	1	0.52
EI_c/EI_c^0	0.5/1	1	0.52
GJ/GJ^0	0.5/1	1	1
Extension and Winglet			
Extension sweep	$0^o/25^o$	0°	0°
Extension aft offset (ft)	0/4	0	0
Winglet cant angle	$60^o/90^o$	90°	63°
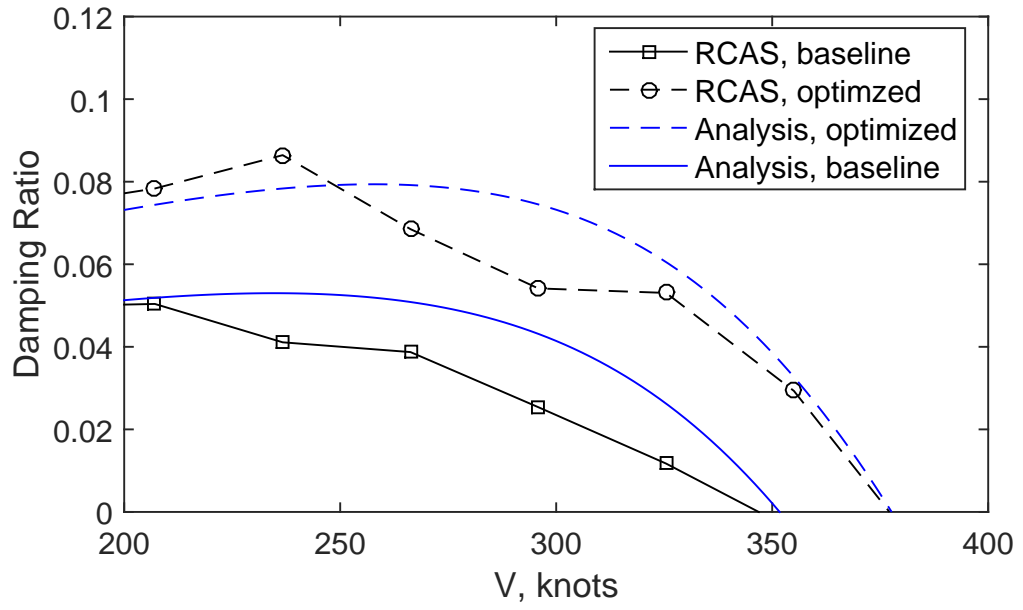
Figure 3.20: Damping ratios of the beam mode for the baseline and optimized (Optimized-E) designs.

Chapter 4
Wing Structural Model and Parametric Studies

The optimization studies presented in Chapter-3 determine the optimal combinations of the wing beamwise stiffness (EI_b), chordwise stiffness (EI_c), torsional stiffness (GJ), bending torsion coupling parameters (K_{bt}, K_{ct}), and structural taper. The wing structural model in developed in this chapter computes the stiffness parameters for a given airfoil contour, stringers and spar locations, torque box dimensions, and material properties. The model also computes the strength of the wing under any given loading condition. The Tsai-Wu stress criterion, which is a quadratic stress criterion (material fails if Tsai-Wu coefficient is greater than unity [50]), is used as a metric to quantify strength. The structural model also calculates the buckling load. The panels on the upper surface are under compression and are susceptible to buckling. The compressive force is computed by integrating the in-plane normal force under the given loading. This in-plane force must be less than the buckling load of the panel. The panel is modeled as a rectangular panel, clamped between adjacent ribs and simply supported between two adjacent stringers.

4.1 Structural Model

The wing is structurally modeled as a three-cell cross section including stringers, skin, and a torque box. A schematic of the wing structure is shown in Fig. 4.1. This structural model of the wing is similar to the models describes in Refs. 4, 5, and 51. The details of the structural model are described here.
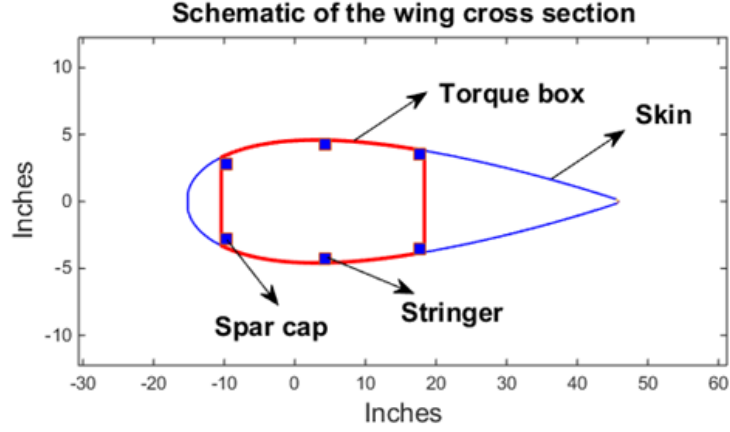
Figure 4.1: Schematic of the wing structural model.

4.1.1 Modeling Composite Panels

The torque box of the wing is made of composite laminate panels (Fig. 4.2, from Ref. 5). The classical laminated plate theory, where the contributions of each individual lamina are summed together to form properties of the laminate, is used to model the composite laminate panels.
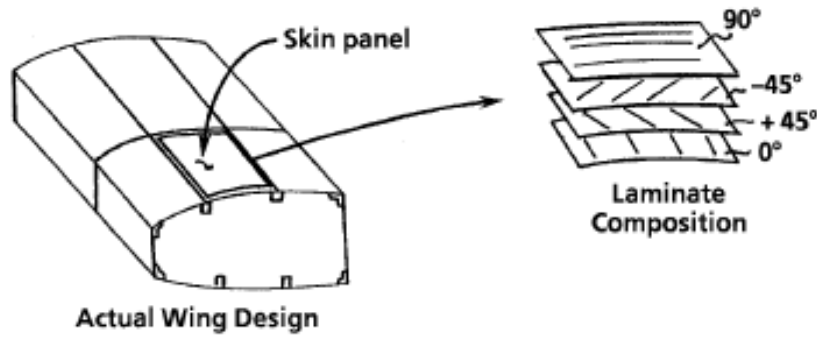
Figure 4.2: Schematic showing wing torque box and composite laminate panels.

The stiffness coefficients of the individual lamina depend on its orientation θ_p with respect to its principal axes (Fig. 4.3a, from Ref 52). The equations governing the stress and strain of a laminate is given by

$$
\begin{bmatrix} \sigma_x \\ \sigma_y \\ \sigma_{xy} \end{bmatrix} = \begin{bmatrix} \bar{Q}_{11} & \bar{Q}_{12} & \bar{Q}_{61} \\ \bar{Q}_{21} & \bar{Q}_{22} & \bar{Q}_{62} \\ \bar{Q}_{61} & \bar{Q}_{26} & \bar{Q}_{66} \end{bmatrix} \begin{bmatrix} \epsilon_x \\ \epsilon_y \\ \epsilon_{xy} \end{bmatrix}
\tag{4.1}
$$

(a) Schematic of a lamina showing its orientation with the principal axis.

(b) Laminate displacement and force definitions.

Figure 4.3: Laminae principal directions and laminate force and moment definitions.

If transverse in-plane stress, σ_y is neglected, the above equation can be rewritten as

$$
\begin{bmatrix} \sigma_x \\ \sigma_{xy} \end{bmatrix} = [Q_1] \begin{bmatrix} \epsilon_x \\ \epsilon_{xy} \end{bmatrix} \tag{4.2}
$$

where

$$
[Q_1] = \begin{bmatrix} \bar{Q}_{11} - \frac{\bar{Q}_{12}^2}{\bar{Q}_{22}} & \bar{Q}_{16} - \frac{\bar{Q}_{12}\bar{Q}_{26}}{\bar{Q}_{22}} \\ \bar{Q}_{16} - \frac{\bar{Q}_{12}\bar{Q}_{26}}{\bar{Q}_{22}} & \bar{Q}_{66} - \frac{\bar{Q}_{26}^2}{\bar{Q}_{22}} \end{bmatrix} \tag{4.3}
$$

The properties of a composite laminate are calculated by integrating individual lamina properties through thickness (t_p) of the blade.

The relationship between the force resultants and laminate strains is given by

$$
\begin{bmatrix} N_z \\ N_{zs} \\ M_z \\ M_{zs} \end{bmatrix} = \begin{bmatrix} A_{11} & A_{16} & B_{11} & B_{16} \\ A_{16} & A_{66} & B_{16} & B_{66} \\ B_{11} & B_{16} & D_{11} & D_{16} \\ B_{16} & B_{66} & D_{16} & D_{66} \end{bmatrix} \begin{bmatrix} \epsilon_z \\ \epsilon_{zs} \\ \kappa_z \\ \kappa_{zs} \end{bmatrix} \tag{4.4}
$$

where

$$
(A_{ij}, B_{ij}, D_{ij}) = \int_{-t_p/2}^{t_p/2} Q_{1ij}(1, z, z^2) \, dz \tag{4.5}
$$

and N_z and N_{zs} are the plate stress resultants, M_z and M_{zs} are the plate moment resultant, ϵ_z and ϵ_{zs} are the plate strains, and κ_z and κ_{zs} are the plate bending curvatures (Fig. 4.3b).

4.1.2 Computing Wing Stiffnesses and Strength

The wing stiffness is computed based on the laminate panel properties and the cross-section geometry using Vlasov theory [53]. The wing displacements and rotations are computed in terms of the beam forces to find the wing stiffness. The detailed derivation of this analysis can be found in Ref. 53. The wing is assumed to undergo beamwise bending $(w(z))$, chordwise bending $(v(z))$, and torsion $(\phi(z))$, where z is the spanwise coordinate (Fig. 4.4).
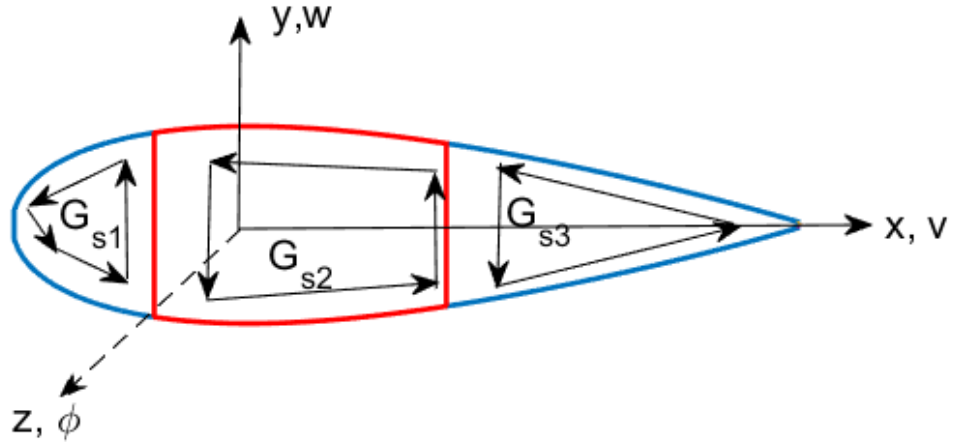
Figure 4.4: A schematic the wing showing shear moduli for different cells.

The relationship between the beamwise bending moment (M_x), chordwise bending moment (M_y), torsional moment (M_z), and the curvatures $w''(z), v''(z), \phi'(z)$, is given by

$$\begin{bmatrix} M_x \\ M_y \\ M_z \end{bmatrix} = \begin{bmatrix} EI_b & 0 & K_{bt} \\ 0 & EI_c & K_{ct} \\ K_{bt} & K_{ct} & GJ \end{bmatrix} \begin{bmatrix} w''(z) \\ v''(z) \\ \phi'(z) \end{bmatrix} \tag{4.6}$$

where the expressions for various stiffness terms appearing in the above equations are given by

$$EI_b = \oint \cos\theta(D_{11}\cos\theta + B_{11}y) + y(B_{11}\cos\theta + A_{11}y) \, ds \tag{4.7}$$

$$EI_c = \oint \sin\theta(D_{11}\sin\theta - B_{11}x) - x(B_{11}\sin\theta - A_{11}x) \, ds \tag{4.8}$$

$$GJ = \oint 4D_{66} - (2B_{66}G_s)/G_t - (G_s(2B_{66} - (A_{66}G_s)/G_t))/G_t \, ds \tag{4.9}$$

$$K_{bt} = \oint -\cos\theta(2D_{16} - (B_{16}G_s)/G_t) - y(2B_{16} - (A_{16}G_s)/G_t) \, ds \qquad (4.10)$$

$$K_{ct} = \oint \sin\theta(2D_{16} - (B_{16}G_s)/G_t) - x(2B_{16} - (A_{16}G_s)/G_t) \, ds \qquad (4.11)$$

where θ is the angle between a tangent drawn at the airfoil segment location and the x axis (see Fig. 4.5). $G_t = A_{66}$ and G_s is the variation of shear modulus along
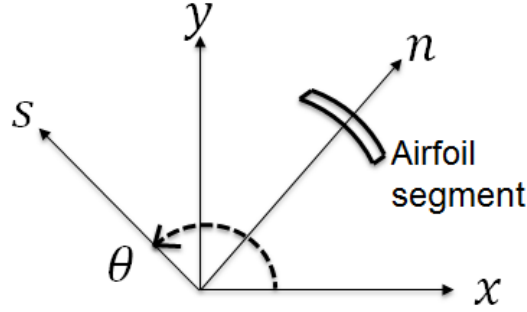
Figure 4.5: A schematic showing the tangential (s) and normal directions (n) of an airfoil segment.

the contour. The shear flow distribution for the three-celled cross section wing is shown in Fig. 4.4. In Fig. 4.4, G_{s1}, G_{s2}, and G_{s3}, are the shear moduli for cells 1,2, and 3, respectively. The shear moduli are computed by setting the warping deformation over each cell to be zero, yielding the following equations:

$$\oint \frac{G_s}{A_{66}} \, ds = 2A_i; \quad i = 1, 2, 3 \qquad (4.12)$$

where A_i is the area of the ith cell.

The stiffness values thus calculated can be substituted in Eq. (4.6) to compute w'', v'', ϕ' for any given moments M_x, M_y, and M_z. The strains ϵ_{zs} and ϵ_z can be computed using the expressions:

$$\epsilon_z = xw'' + yv'' \qquad (4.13)$$

$$\epsilon_{sz} = \frac{G_s}{A_{66}}\phi'_z \qquad (4.14)$$

The strains are substituted into the Eq. 4.2 to get the stresses in each lamina. The Tsai-Wu stress criterion, which is a quadratic stress criterion, is used as a metric to

quantify strength. The Tsai-Wu stress criterion is [50]:

$$F_{11}\sigma_1^2 + F_{22}\sigma_2^2 + F_{66}\sigma_6^2 + F_1\sigma_1 + F_2\sigma_2 + 2F_{12}\sigma_1\sigma_2 < 1 \qquad (4.15)$$

where

$$F_{11} = \frac{1}{s_L^+ s_L^-} \;\; ; \;\; F_1 = \frac{1}{s_L^+} - \frac{1}{s_L^-} \qquad (4.16)$$

$$F_{22} = \frac{1}{s_T^+ s_T^-} \;\; ; \;\; F_2 = \frac{1}{s_T^+} - \frac{1}{s_T^-} \qquad (4.17)$$

$$F_{66} = \frac{1}{s_{LT}^2} \;\; ; \;\; F_{12} = -\frac{\sqrt{F_{11}F_{22}}}{2} \qquad (4.18)$$

and s is the strength of the lamina. The subscripts L and T stand for longitudinal and transverse directions, respectively. The superscripts $+$ and $-$ stand for tension and compressive strength, respectively.

4.1.3 Buckling

The model also calculates the buckling load. The panels on the upper surface are under compression and are susceptible to buckling. The compressive force is computed by integrating the in-plane normal force under the given loading (Fig. 4.6). This in-plane force must be less than the buckling load of the panel. The panel is modeled as a rectangular panel, clamped between adjacent ribs and simply supported between two adjacent stringers.
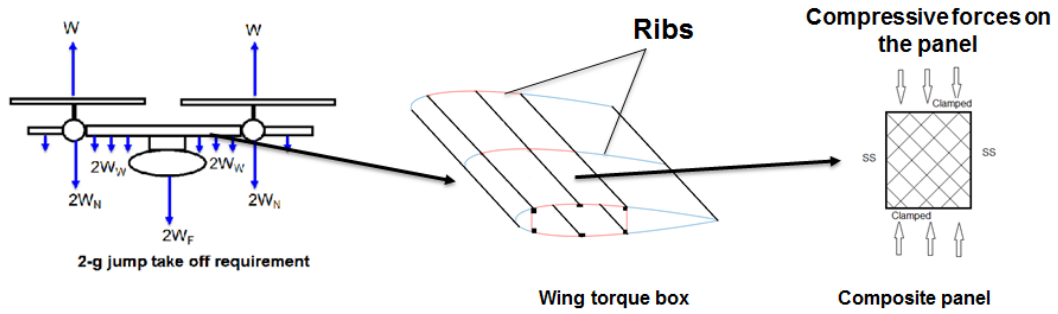

Figure 4.6: A schematic for computing buckling loads.

Consider a composite rectangular panel with sides a and b, as shown in Fig. 4.7 (from Ref. 54). The in-plane compressive forces are N_{xx}^0 and N_{yy}^0. The in-plane

shear load is N_{xy}^0. In this analysis, $N_{yy}^0 = 0$ and $N_{xy}^0 = 0$, and only the compressive buckling load N_{xx}^0 is studied.
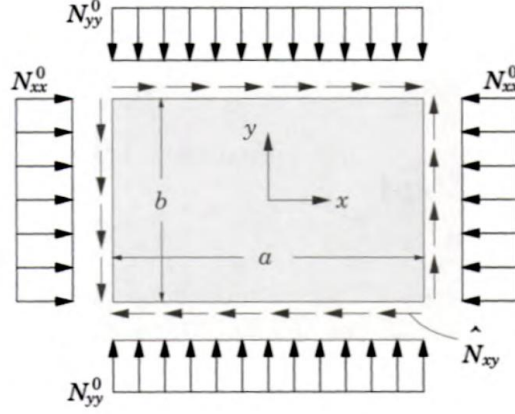

Figure 4.7: Schematic of a composite panel (from Ref. 54).

The Ritz method [54] is used to find the critical buckling loads. The transverse deflection, $w(x, y)$ is written as a sum of admissible functions, depending on the boundary conditions:

$$w(x, y) = \sum_{i}^{m} \sum_{i}^{n} c_{ij} X_i(x) Y_j(y) \tag{4.19}$$

where $X_i(x)$ and $Y_j(y)$ are the admissible functions. The panel is assumed to be clamped between the adjacent ribs ($x = 0$ and $x = a$) and simply supported along two adjacent stringers ($y = 0$ and $y = b$). The admissible functions are given by:

$$X_i(x) = \left(\frac{x}{a}\right)^{i+1} \left(\frac{a - x}{a}\right)^{i+1} \tag{4.20}$$

$$Y_j(x) = \left(\frac{y}{b}\right)^{j} \left(\frac{b - y}{b}\right)^{j} \tag{4.21}$$

The total energy (Π) of the system is given by

$$2\Pi = \int_0^b \int_0^a \left[D_{11} \left(\frac{\partial^2 w}{\partial x^2}\right)^2 + 2D_{12} \left(\frac{\partial^2 w}{\partial x^2}\right) \left(\frac{\partial^2 w}{\partial y^2}\right) + 4D_{66} \left(\frac{\partial^2 w}{\partial x \partial y}\right)^2 \right.$$
$$\left. + D_{22} \left(\frac{\partial^2 w}{\partial y^2}\right)^2 - 2N_{xx} \left(\frac{\partial w}{\partial x}\right)^2 \right] dx \, dy \tag{4.22}$$

Applying the total minimum total energy principle, $\delta\Pi = \frac{\partial\Pi}{\partial c_{ij}} = 0$, results in an eigenvalue problem:

$$[A_b][X_b] = N_{xx}[B_b][X_b] \tag{4.23}$$

where $[A_b]$ and $[B_b]$ are $mn \times mn$ matrices given by

$$[A_b]_{rs} = D_{11}X_i''Y_jX_p''Y_q + 2(D_{12} + 2D_{66})X_i'Y_j'X_p'Y_q' + D_{22}X_iY_j''X_pY_q'' \tag{4.24}$$

$$[B_b]_{rs} = X_i'X_p'Y_jY_q \tag{4.25}$$

and $i = 1, \ldots, m$; $p = 1, \ldots, m$; $j = 1, \ldots, n$; $q = 1, \ldots, n$, $r = (i-1)m + j$, and $s = (p-1)m + q$.

4.2 Structural Parametric Studies

The wing structural model is exercised by designing a wing with similar characteristics as that of the XV-15 wing (23% t/c). The material chosen for the laminates is the advanced composite material IM7/8552. The material properties of IM7/8552 composite are tabulated in Table 4.1 (from [52]).

Table 4.1: IM7/8552 material properties (from [52]).

Property	E_L	E_T	G_{LT}	ν_{LT}	S_L^+	S_L^-	S_T^+	S_T^-	S_{LT}
Value	23.8	1.7	0.754	0.32	395	245	16.1	21.8	17.4
Unit	msi	msi	msi	msi	ksi	ksi	ksi	ksi	ksi

The vertical walls of the torque box are designed to be at a distance of $0.07c$ and $0.55c$ from the leading edge, where $c = 5.16$ ft, is the chord of the wing. The skin is designed with ±45 laminates; adding more plies to the skin increases the bending and torsional stiffness, but also increases the weight. Fifty unidirectional plies are used for the spar caps and stringers. The torque box of the wing is designed using $[\pm15, \pm30_3]_S$ laminates. The orientations are determined using the trial-and-error method, such that the stiffness of the designed wing matches that of the XV-15 wing. The beamwise bending stiffness (EI_b), chordwise bending stiffness (EI_c), and torsional stiffness (GJ) of the designed wing and the XV-15 wing are tabulated in

Table 4.2: Comparison of the XV-15 wing stiffness [4] and the designed wings in this study.

Stiffness (lb-in^2)	XV-15 23% t/c	Designed 23% t/c
EI_b	3.70E09	3.66E09
EI_c	1.12E10	1.35E10
GJ	2.80E09	2.82E09

Table 4.2. From Table 4.2, we can say that the designed wing has similar stiffness to the XV-15 wing.

The loading cases considered are 2g jump takeoff (helicopter mode) and 4g pull-up loadings (airplane mode). The 2g jump takeoff loading case is where a load equal to twice the aircraft weight, multiplied by a safety factor of 1.25 ($T = 2 \times 1.25 \times W$) is applied at the wing-tips. The 4g pull-up loading case is where a load of four-times the aircraft weight, multiplied by a safety factor of 1.25 is applied on the wings (triangularly distributed). The corresponding bending moment plots for the 2g and the 4g loadings are shown in Fig. 4.8. The 2g and the 4g loading cases are used in the design of the NASA LCTR2 (Ref. 46).
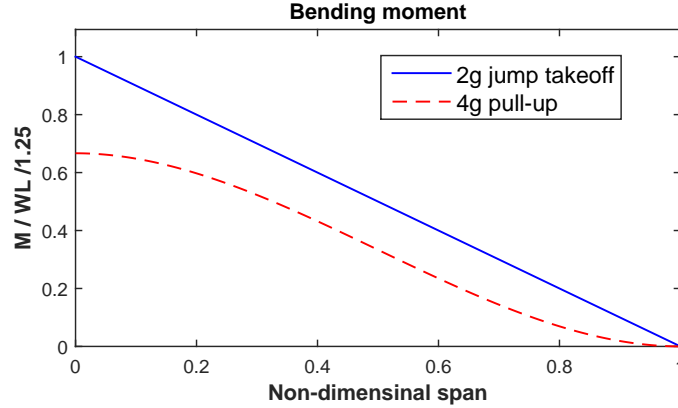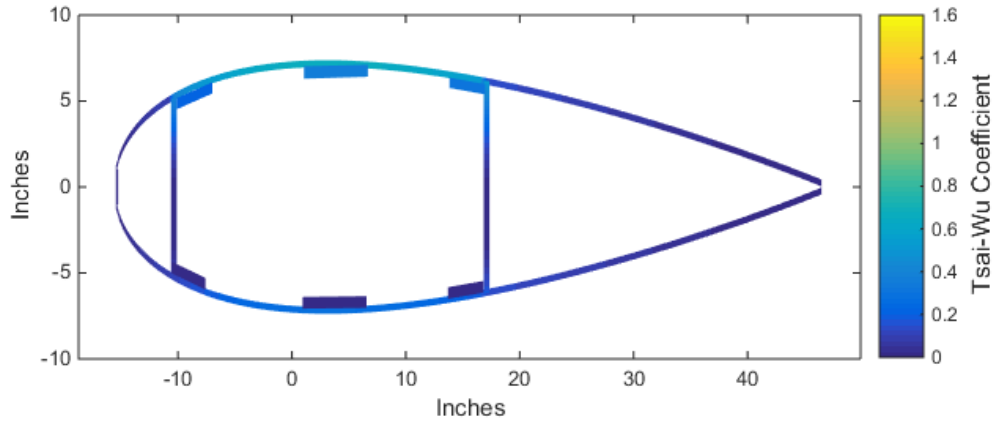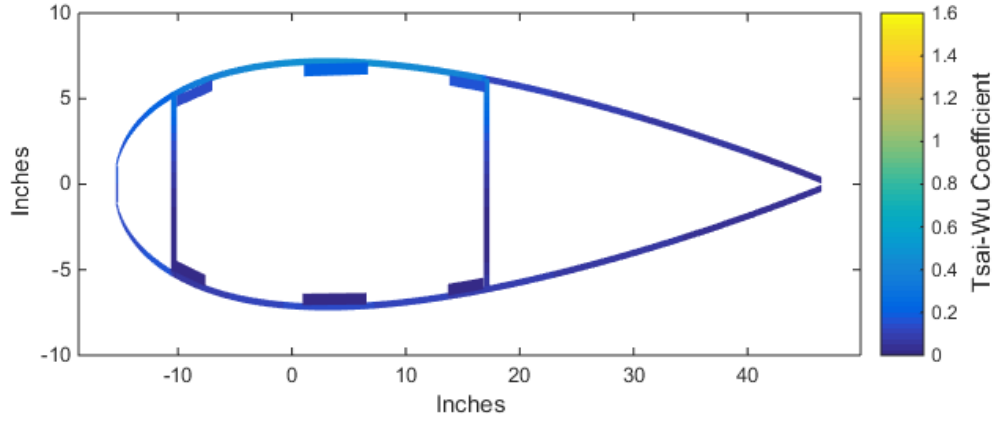

Figure 4.8: Bending moment distribution for the 2g jump takeoff and 4g pull-up loading cases.

The Tsai-Wu coefficient along the wing contour is shown in Fig. 4.9 for 2g loading and 4g loading. The maximum Tsai-Wu coefficient is 0.71 for the 2g loading and 0.46 for the 4g loading.

(a) 2g jump takeoff loading (max Tsai-Wu = 0.71).

(b) 4g pull-up loading (max Tsai-Wu = 0.46).

Figure 4.9: Tsai-Wu coefficient for the designed XV-15 wing.

To simulate an aerodynamically efficient wing, the thickness of the designed wing is reduced from 23% to 15% retaining the material properties. The Tsai-Wu coefficient along the wing contour for this thin wing, is shown in Fig. 4.10. In Fig. 4.10, we can see that the top and bottom faces walls of the torque box are in yellow – which implies that the Tsai-Wu coefficient is greater than unity in these regions. The maximum Tsa-Wu coefficient for the thin wing is 1.57 for 2g loading and 1.01 for 4g loading.
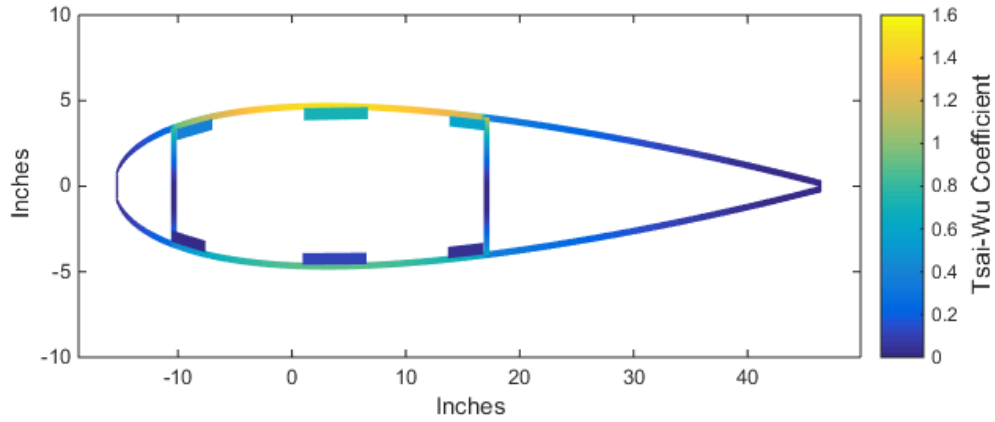
(a) 2g jump takeoff loading (max Tsai-Wu = 1.57).
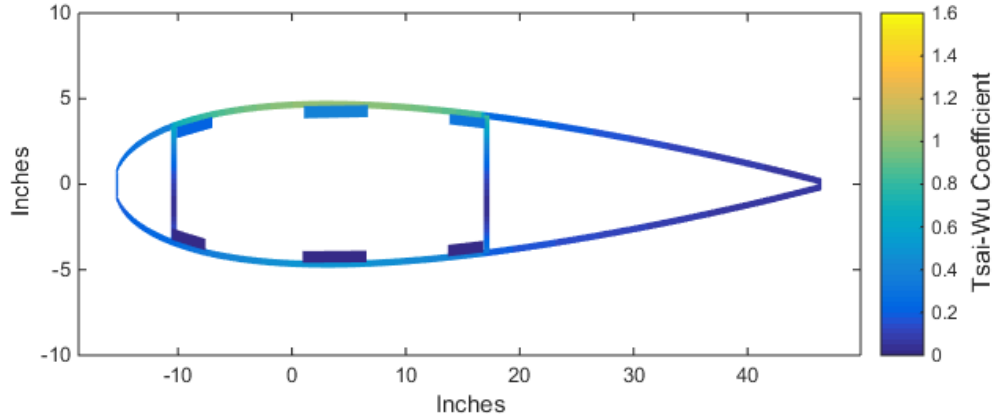
(b) 4g pull-up loading (max Tsai-Wu = 1.01).

Figure 4.10: Tsai-Wu coefficient for the 15% t/c wing.

To strengthen the thin wing, the torque box is redesigned with eight unidirectional plies at the top and bottom of the torque box. This brought down the maximum Tsai-Wu coefficient to 0.61 and 0.45 for the 2g and 4g loadings, respectively (see Fig. 4.11).

Reducing the wing thickness also decreases the beamwise bending and torsion stiffnesses. The beamwise bending stiffness is reduced by 30% while the torsional stiffness is reduced by 49%. The stiffnesses for the thick wing and thin wing are tabulated in Table 4.3.

The reduction in stiffness of the thin wing affects the aeroelastic characteristics of the wing. The damping characteristics of the thin and thick wings are plotted in Fig. 4.12. We can see from Fig. 4.12 that the damping of the beam and torsion
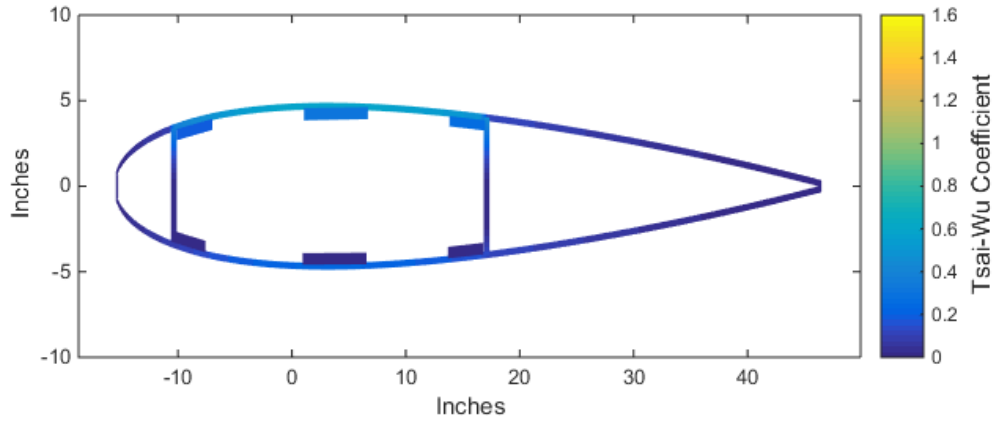
(a) 2g jump takeoff loading (max Tsai-Wu = 0.61).

(b) 4g pull-up loading (max Tsai-Wu = 0.45).
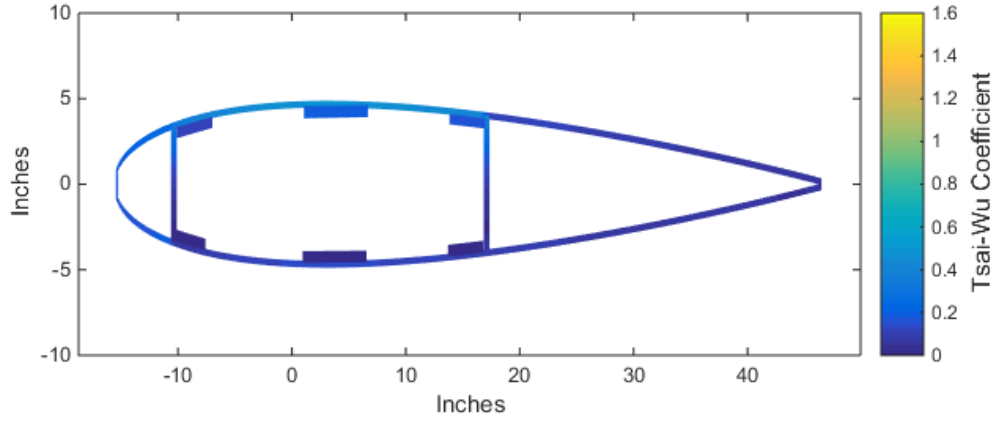
Figure 4.11: Tsai-Wu coefficient for the strength designed 15% t/c wing.

Table 4.3: Comparison of the thin wing and the thick wing stiffnesses.

Stiffness (lb-in^2)	Designed 23% t/c	Strength designed 15% t/c
EI_b	3.66E09	2.55E09
EI_c	1.35E10	1.70E10
GJ	2.82E09	1.42E09

modes decreases significantly. This result, showing the reduction in the stability with decreasing wing thickness, is consistent with the results reported in Ref. 4.

The variation of buckling load of the laminate of the torque box is computed
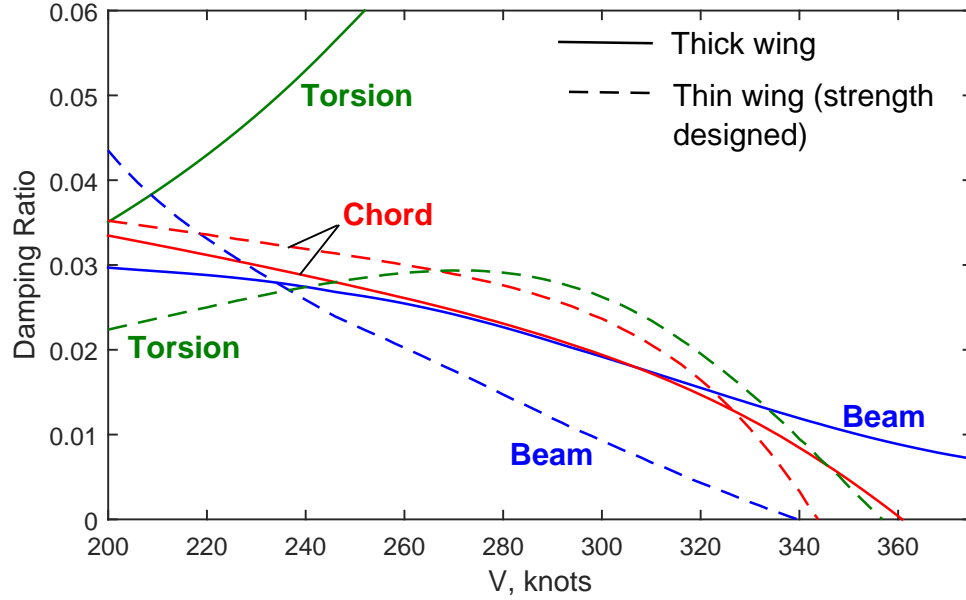
Figure 4.12: Damping characteristics of the thin and thick wings.

using 25 admissible functions. The buckling load factor (BLF), which is the ratio of the critical buckling load and applied load, is tabulated in Table 4.4 for the laminate $[\pm 30_3, \pm 15, 0_4]_S$, for different thickness ratios and boundary conditions: simply supported along the stringers and clamped between ribs (ss-cc), and simply supported along the stringers and ribs (ss-ss). From Table 4.4, we can see that BLF increases with thickness and is higher for the ss-cc boundary condition compared to the ss-ss boundary condition. Therefore, the ss-ss boundary condition must be used in the bucking analysis of torque box laminates.

For t/c = 15%, the BLF is less than one for the $[\pm 30_3, \pm 15, 0_4]_S$ laminate under the ss-cc boundary condition, and hence it buckles. Since BLF is less than one, the laminate is reinforced with unidirectional plies $[0_2]$, (the new reinforced laminate is $[\pm 30_3, \pm 15, 0_5]_S$) to increase the stiffness of the laminate and to increase the BLF. We can see from Table 4.4 that the reinforced laminate $[\pm 30_3, \pm 15, 0_5]_S$ has a BLF of 1.11 for t/c = 15%, and hence does not buckle.

Table 4.4: Variation of buckling load factor vs wing thickness.

| t/c | $[\pm 30_3, \pm 15, 0_4]_S$ | | $[\pm 30_3, \pm 15, 0_5]_S$ | |
	BLF (ss-cc)	BLF (ss-ss)	BLF (ss-cc)	BLF (ss-ss)
15%	1.15	0.88	1.45	1.11
17%	1.32	1.01	1.66	1.27
19%	1.49	1.15	1.87	1.43
21%	1.66	1.28	2.09	1.60

Chapter 5
Aerodynamic Model and Parametric Studies

The previous chapters discuss the aeroelastic and structural aspects of tiltrotor wing design. This chapter discusses the aerodynamic issues involved in designing high-speed tiltrotor aircraft. An existing aerodynamic model (described in the following section) is used for conducting parametric studies on improving the lift-to-drag ratio.

5.1 Aerodynamic Model

The aerodynamic performance is generated from an in-house tool called Polar Generation Software (PGEN, [55]), which was developed to analyze the performance of sailplanes, and applied to tiltrotors recently [45]. PGEN calculates the total drag for fixed-wing aircraft based on the aircraft geometry, center of gravity, gross weight, two-dimensional aerodynamic airfoil data, and operating conditions. The induced drag of the wing is calculated using Horstmann's multiple lifting line method for non-planar wings. This method allows the modeling of complex geometrical discontinuities such as wing-nacelle and wing extension-winglet junctions. The wing and empennage profile drag and pitching moment are computed from two-dimensional airfoil tables based on the sectional lift coefficient. The fuselage drag is modeled using the equivalent flat plate area approximation. PGEN computes accurate and fast calculation of vehicle aerodynamic performance, which is needed when coupled to an optimizer. The propeller/wing interaction effect was not taken in account in the analysis due to research results showing limited impact on the

tiltrotor performance [45].

The wing and extension airfoils used in this analysis are the SM205 airfoil [56]. The SM205 airfoil (21% t/c) is designed for high-efficiency tiltrotors by taking advantage of laminar flow. It has a large minimum drag bucket that extends to relatively high lift coefficients as shown in Fig. 5.1. This allows the tiltrotor to cruise at high lift coefficients with relatively low drag.
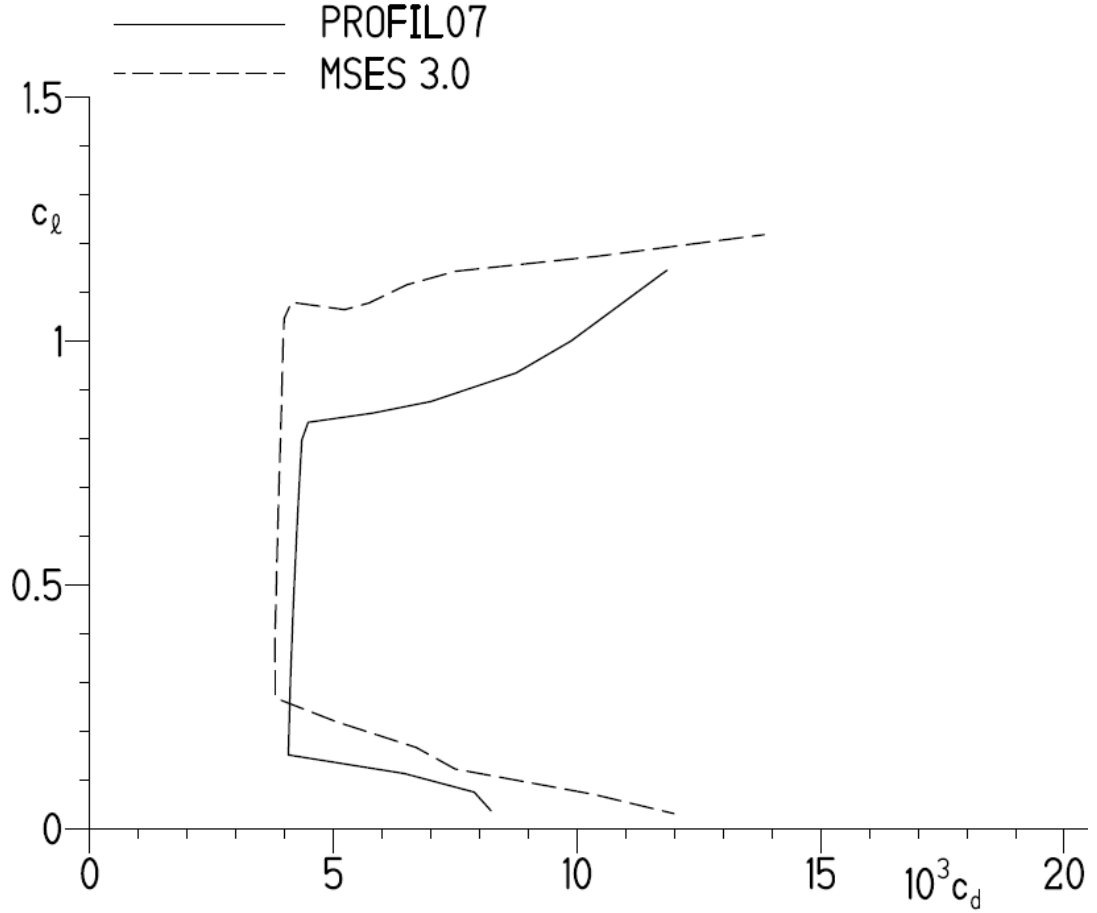

Figure 5.1: Drag polar of the SM205 airfoil, M = 0.55, R = 23.6E06, computed by Somers and Martin in [56], using PROFIL07 [57] , MSES 3.0 [58].

The data for the SM205 airfoil was not available in the literature for the range of Reynolds and Mach numbers required for the current study. Therefore, the Prandlt-Gluaert corrections are used to scale the airfoil characteristics to incompressible

flow. The Prandlt-Gluaert corrections are

$$c_x = \frac{c_{x0}}{\sqrt{1 - M_\infty^2}} \tag{5.1}$$

where $c_x = \{c_l, c_m, c_d\}$, and c_l, c_m, and c_d are the lift, moment, and drag coefficients, respectively. The following equation [59] is used to account for the behavior of drag coefficient with Reynolds number:

$$c_d = c_{d0}\left(\frac{R_0}{R}\right)^{0.11} \tag{5.2}$$

The drag polars for R= $7.3E06, 14.6E06$, and $29.2E06$, calculated using the above equation, are shown in Fig. 5.2.
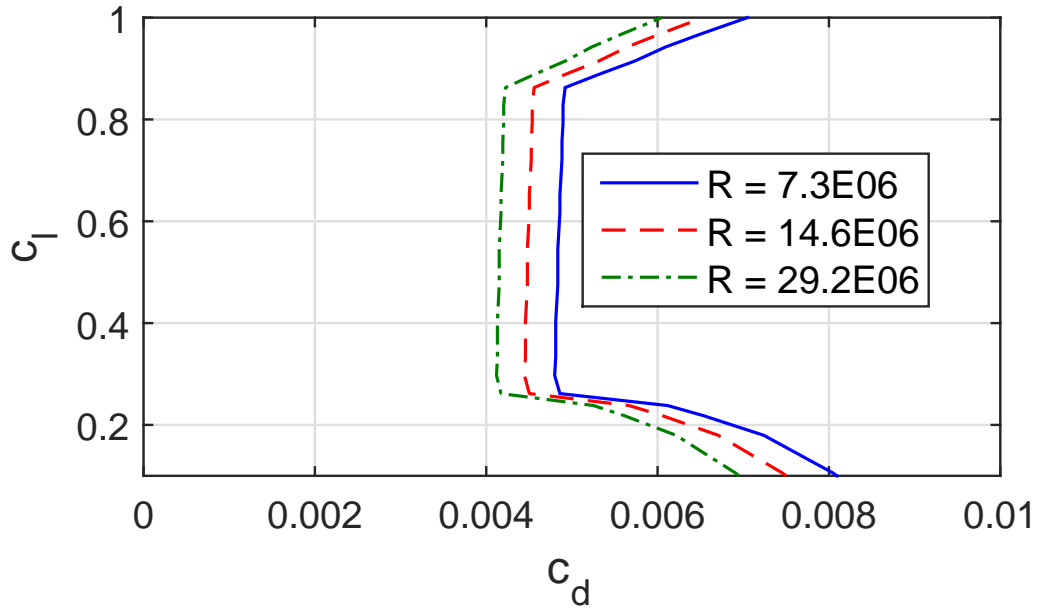

Figure 5.2: Drag polars of the SM205 airfoil at different Reynolds numbers.

5.2 Parametric Studies

The aerodynamic effects of parameters such as wing thickness, extension and winglet planform variables, and cruise speed and altitude are discussed here. The baseline parameters are tabulated in Tables 5.1 and 5.2. The cruise speed and altitude are

assumed to be 250 knots and 10,000 ft, respectively. All the parametric studies conducted here are for a constant wing loading. In other words, the planform area, which is the projected area of the wing, extension, and winglet, is maintained constant throughout the parametric studies. The chords of the wing, extension, and winglet are multiplied by a correction factor (k_{wl}, a function of extension span and taper ratio, and winglet span and taper ratio), so as to maintain a constant planform area. A schematic showing the extension span, winglet height and winglet span is shown in Fig. 5.3. In Fig. 5.3, l_0, l_e, and l_w are the spans of the inboard wing, extension, and winglet, respectively. c_1 and c_2 are the root and tip chords of the extension, respectively. c_2 and c_3 are the root and tip chords of the winglet, respectively. The expression for the total planform area of the wing is

$$S_W = 2(c_1 l_0 + 0.5(c_1 + c_2)l_e + 0.5(c_2 + c_3)l_w) \tag{5.3}$$

The expression for k_{wl} is:

$$k_{wl} = \frac{l_0}{l_0 + 0.5l_e(1 + \lambda_e) + 0.5l_w\lambda_e(1 + \lambda_w)} \tag{5.4}$$

where λ_e and λ_w are the taper ratios of the extension and winglet.

Table 5.1: Rotor and wing properties (baseline).

Rotor	
Number of blades	3
Radius (R) (ft)	12.5
Lock number	3.83
Solidity	0.089
Blade flapping inertia (slug-ft^2)	105
Lift curve slope	5.7
Pitch-flap coupling	-0.268
Tip speed (ft/sec.)	600
Rotational speed (Ω) (rad/sec.)	48
Wing (Semi-span)	
Span (L/R)	1.333
Chord (c/R)	0.413
Mast height (h/R)	0.342

Table 5.2: Wing extension and winglet properties (baseline).

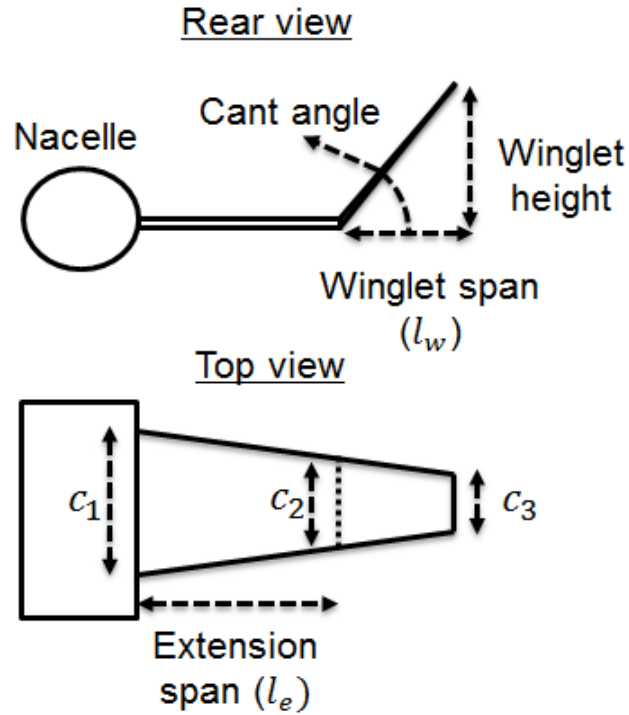| Wing Extension	
Length	4.5 ft
Root chord	5.16 ft
Taper	0.5
Sweep	0 deg
Aft offset	0 ft
Winglet	
Height	4.5 (ft)
Root chord	2.58 ft
Taper	0.5
Sweep	0 deg
Cant angle	80 deg
Toe angle	0 deg
Twist angle	0deg

Figure 5.3: A schematic showing extension span, winglet winglet height.

5.2.1 Wing Extension Span and Winglet Height

The extension increases the span of the aircraft and reduces induced drag. The effects of the wing extension on L/D are shown in Fig. 5.4 for different winglets heights. From Fig. 5.4, we can see that the L/D increases with extension span; and for a given extension span, L/D increases as the winglet height is increased.
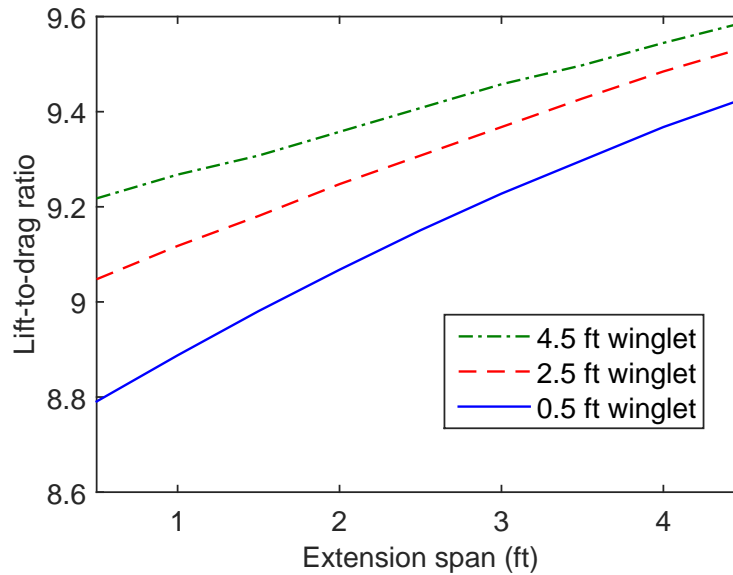

Figure 5.4: L/D vs extension span for different winglet heights.

5.2.2 Winglet Cant, Toe, and Twist Angles

The effects of winglet cant, sweep, and toe angles (schematic shown in Fig. 5.5) on L/D are investigated here. The properties of the extension are held at their baseline values. The L/D vs cant angle for is shown in Fig. 5.6. Increasing the cant angle reduces the span, and hence increases induced drag. From Fig. 5.6, we can see that increasing the cant angle reduces the efficiency of the winglet in improving L/D.

The effects of the winglet toe and twist angles on L/D are shown in Figures 5.7 and 5.8. We can see from Figures 5.7 and 5.8 that a winglet toe angle of about 4 degrees yields a maximum L/D, while a winglet twist angle of about 6 degrees yields a maximum L/D.
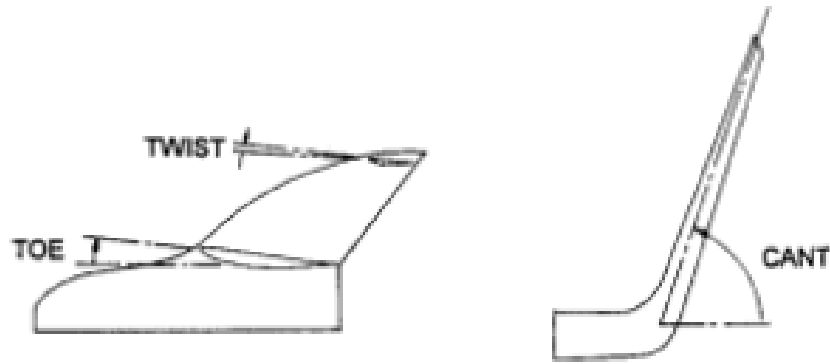
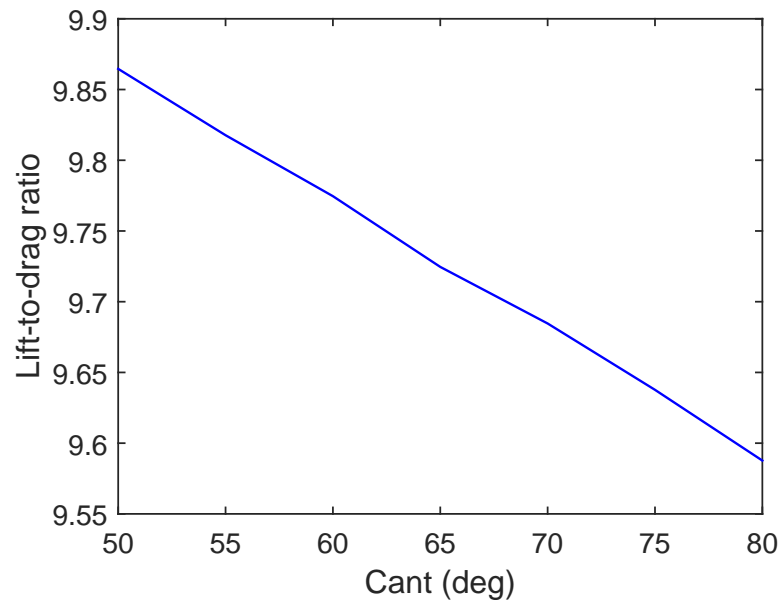Figure 5.5: A schematic showing the toe, twist, and cant angles of the winglet [45].
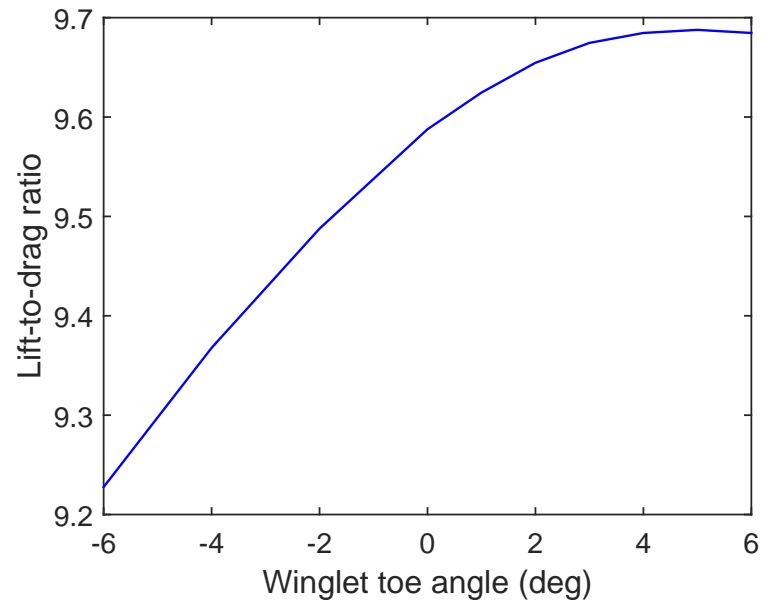

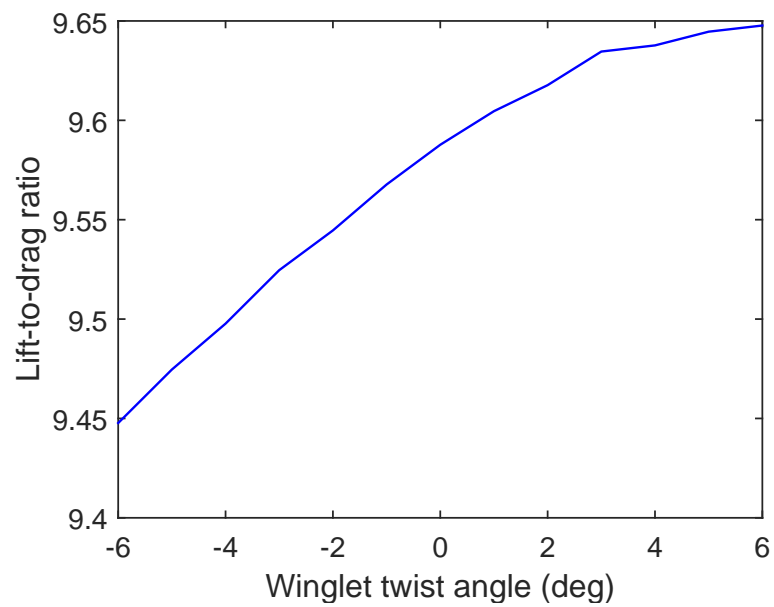Figure 5.6: L/D vs cant angle.

Figure 5.7: L/D vs winglet toe angle.

Figure 5.8: L/D vs winglet twist angle.

5.2.3 Wing Thickness

Thickness ratios of t/c = 15%, 18%, and 21% are considered for analyzing the aerodynamic effects of thickness. The SM205 airfoil is used for the 21% thick wing. To analyze the t/c = 15% and 18% cases, the drag of the SM205 airfoil is reduced by 6 drag counts and 3 drag counts, respectively. The drag polars of the for the 21%, 18%, and 15% wings is shown in Fig. 5.9, for R = 14.6 million and Mach number M = 0.55.

The effects of thickness on L/D of the aircraft, for different extension spans (with the baseline winglet on), is shown in Fig. 5.10. From Fig. 5.10, we can see that L/D increases with extension for all t/c ratios, and for a given thickness ratio, the L/D decreases with increase in thickness.
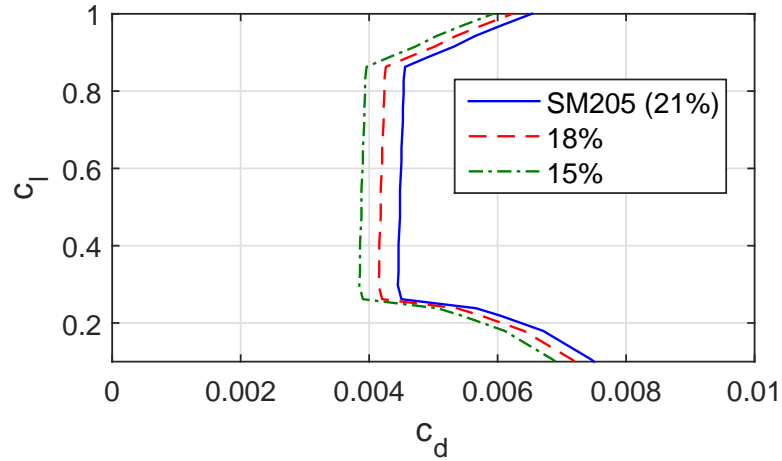
Figure 5.9: Drag polars of the airfoils considered.

5.2.4 Cruise Speed and Altitude

The L/D vs cruise speed for different altitudes is shown in Fig. 5.11 (with the extension and winglet). As the altitude increases, cruise c_l increases, which increases the c_l/c_d. As the cruise speed increases, the fuselage drag increases, which reduces L/D.

Extensions and winglets are more effective in increasing L/D when the cruise c_l is high (at high altitudes). The L/D vs extension span is shown in Fig. 5.12 for cruise speed = 250 knots, and altitude = 5000 ft and 20000 ft. We can see from
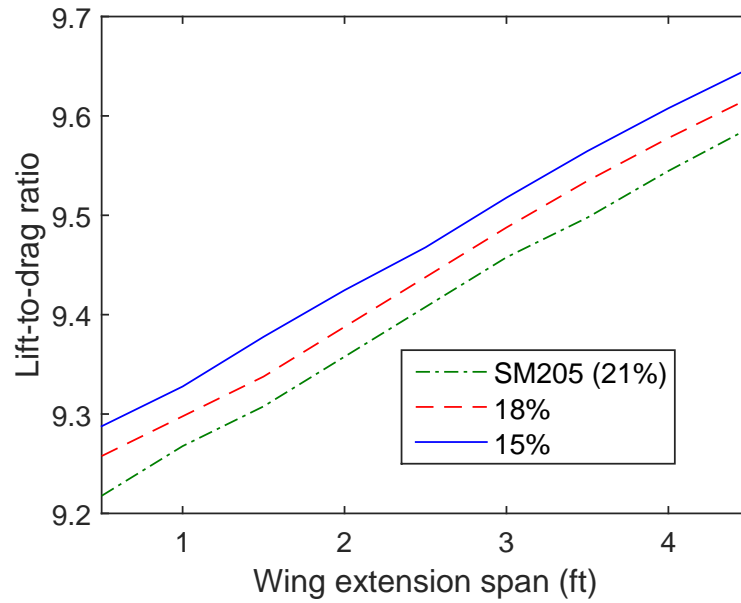
Figure 5.10: L/D vs extension span 250 knots.
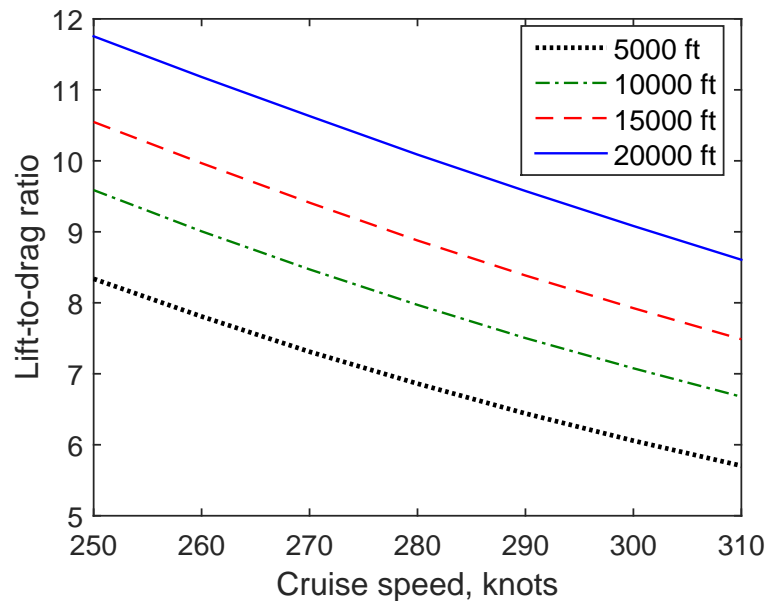
Figure 5.11: L/D vs cruise speed for different altitudes.

Fig. 5.12 that at 5000 ft, adding the extension and winglet increases the L/D from 7.82 to 8.27, which is an 5.7% increase in L/D. At 20000 ft, adding the extension and winglet increases the L/D from 10.25 to 11.78, which is a 15% increase in L/D.

Thus, we can see that efficiency of the extension and winglet in increasing L/D increases with altitude.
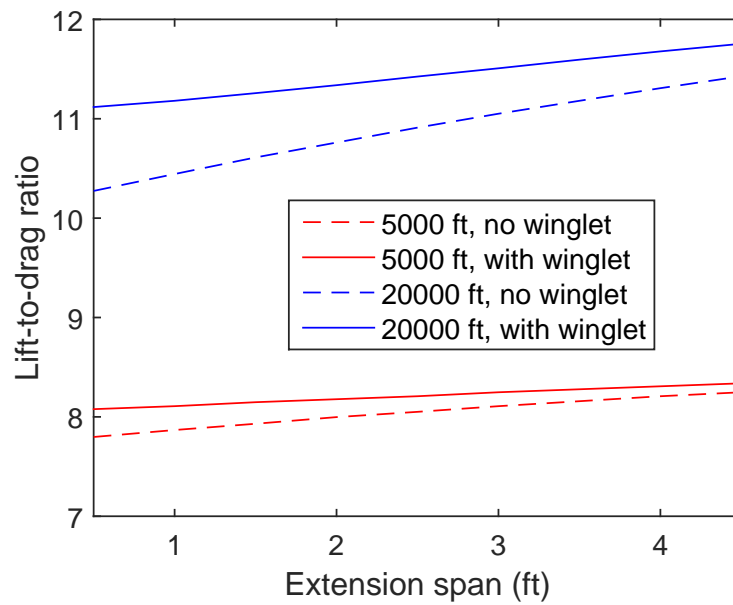
Figure 5.12: L/D vs extension span for different altitudes.

Chapter 6 | Multidisciplinary Optimization

In this study, we extend the optimization studies presented in Chapter 3 by investigating the combined structural and aerodynamic design and optimization of a tiltrotor wing equipped with an extension and a winglet. The aeroelastic and structural models developed are merged with the aerodynamic model for the purpose of optimization. The optimization objective is to minimize the weight penalty due to extensions while maximizing aerodynamic efficiency (lift-to-drag ratio, L/D), subject to strength, buckling, wing loading, and whirl flutter constraints. The key design variables that affect both the structural and aerodynamic characteristics are wing thickness and wing-tip span. The wing loading is held constant throughout the optimization process. The Bell XV-15 tiltrotor aircraft is chosen as the parent aircraft for this study.

6.1 Optimization Methodology

The optimization flowchart is shown in Fig. 6.1. The process begins with choosing the design variables for the optimization. The design variables corresponding to the wing are the torque box skin laminate orientation angles, number of plies, stringer locations, and stringer areas. The extension design variables are the span, taper, sweep, and incidence angles. The winglet design variables are its height, cant, taper, and incidence angles.

These design variables are fed into the aerodynamic analysis, which outputs the performance (objective) to the optimizer. The aerodynamic analysis also outputs the loads. Perturbations of these loads around the trim angle of attack are performed to numerically calculate the lift per pitch distributions ($dL/d\theta$).
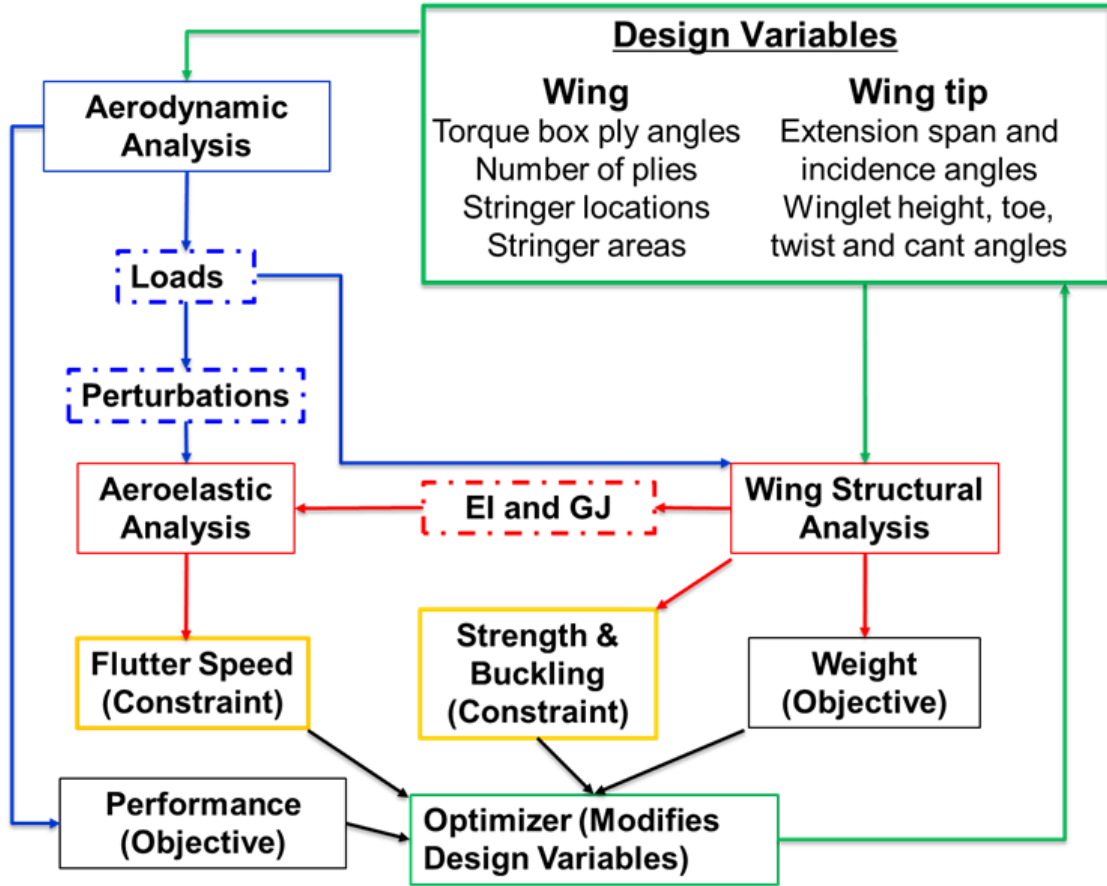
Figure 6.1: Optimization flowchart.

The structural analysis outputs the overall weight of the wing and buckling load, while calculating the stress at any given location along the span, based on the loads generated by the aerodynamic analysis. The weight (objective), buckling load (constraint), and strength (constraint) are fed into the optimizer. The structural analysis also outputs the stiffness (EI and GJ) of the wing.

The EI and GJ values, along with the $(dL/d\theta)$ distributions are fed into the aeroelastic analysis in order to calculate the whirl flutter speed, which is fed into the optimizer as a constraint. The optimizer changes the design variables and the iterations are carried on until the design variables converge to their optimum values.

Only combinations of $0, \pm45$, and 90 degree angles are allowed for the ply orientations. A safety factor of 1.33 is placed on the flutter speed (flutter speed $> 1.3\ V_c$). The other constraints include buckling load factor > 1 and maximum Tsai-Wu coefficient < 1.

Figure 6.2: Schematic of the wing, extension, and winglet.

The chord of the inboard wing is decreased accordingly with the length of the extension, so as to maintain a constant wing loading. Genetic algorithm (GA) is used to for the optimization process [48].

6.2 Results: Winglet Excluded

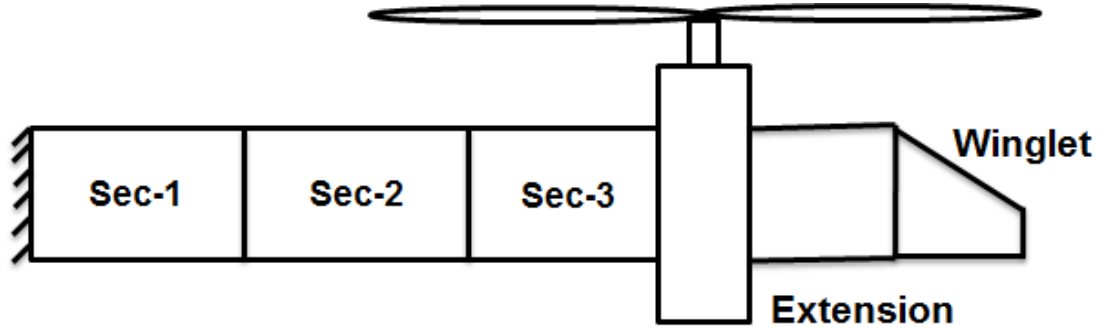The optimization is first performed excluding the winglet in the analysis, for a cruise speed of 220 knots. Five cases were analyzed for different extension spans = {0, 2.5, 3.5, 4.5, 5.5 } ft. The baseline design for the optimization performed is the optimized wing with no extension. The iterations start with a wing weight of 598 lbs. The algorithm converges after 50 iterations to 527 lbs. The convergence plot of the algorithm is plotted in Fig. 6.3. The optimum values for the design variables are tabulated in Table 6.1.

For the case where the wing extension span is set to 2.5 ft, the optimized wing weight is plotted for different thickness ratios in Fig. 6.4. From Fig. 6.4, we can see that the optimum weight decreases from 595 lbs (t/c) to 525 lbs as the thickness increases from 15% to 18%. The optimized laminate is $[0_4, \pm 45_5]$ for the thin wing (thickness ratio = 15 %), and the optimized laminate is $[0_6, \pm 45_4]$ for the thick wing (t/c = 18%). The thin wing has more number of ± 45 plies, which implies that the bending stiffness is compromised for torsional stiffness. Thus, the plies in the stringers need to provide additional bending stiffness. The thick wing, on the other hand has more 0 degree plies and has sufficient bending stiffness, and does not require additional stiffness addition from the stringers. Thus the plies on the stringers can be dropped to save weight.
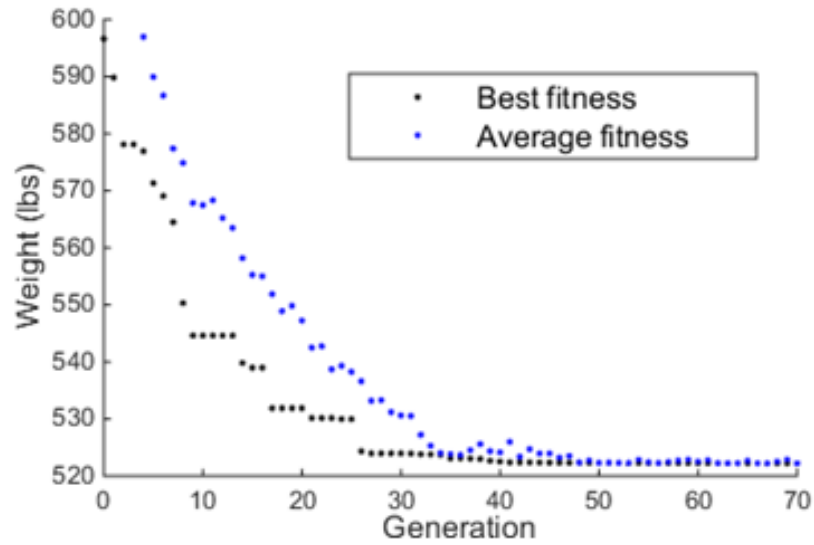
Figure 6.3: Convergence characteristics for the optimization of baseline design.
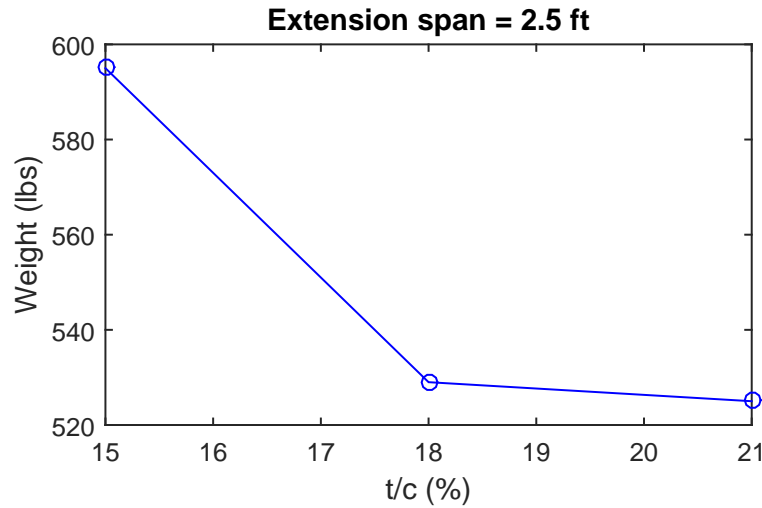
Figure 6.4: Optimum wing weight for vs thickness ratio for extension span = 2.5 ft.

Similar trends are found for other values of extension span. The optimum weight vs thickness ratio for extension span of 3.5 ft and 4.5 ft are plotted in Fig. 6.5. The thinner wings have more 0 degree plies than the thicker wings, and have sufficient bending stiffness. As a result, thick wings do not require additional stiffness addition from the stringers, and hence plies on the stringers can be dropped to save weight.
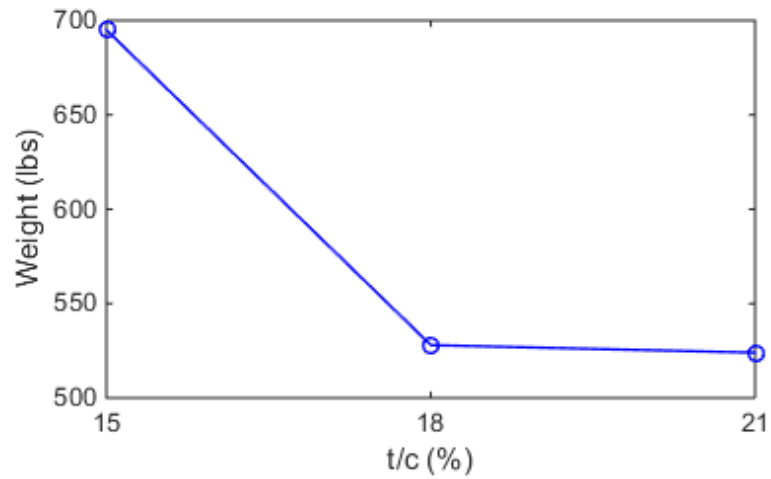
(a) Extension span = 3.5 ft.
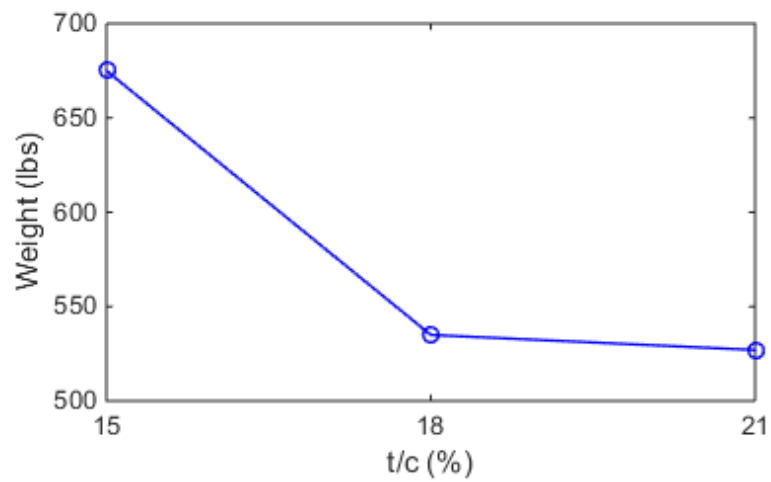
(b) Extension span = 4.5 ft.

Figure 6.5: Optimum wing weight for vs thickness ratio for extension span = 3.5 ft. and 4.5 ft.

The optimum designs for all the cases considered are tabulated in Table 6.1. All the designs have different extension spans while having the same whirl flutter speed. The baseline design and Designs A and B have t/c = 18%, while Designs C and D have t/c = 21%. Design-B has the least wing weight and Design-D has the highest wing weight. However, Design-D has an L/D of 11.51 (11% more than the baseline), for only a weight penalty of 8 lbs (1.5%).

Table 6.1: Optimization results.

	Baseline	Design-A	Design-B	Design-C	Design-D
Extension span (ft)	0	2.5	3.5	4.5	5.5
t/c	18%	18%	18%	21%	21%
Wing Weight (lbs)	527	528	513	527	535
L/D	8.36	8.76	8.90	9.02	9.14
WFS (kts)	330	330	330	330	330
Buckling safety	1.43	2.43	2.43	2.65	2.65
Laminate	$[0_{12}, \pm 45_2]_S$	$[0_6, \pm 45_4]_S$	$[0_6, \pm 45_4]_S$	$[0_8, \pm 45_3]_S$	$[0_8, \pm 45_3]_S$

6.3 Results: Winglet Included

The optimization is performed in the following way: five cases were analyzed where extension and winglet combined span ($l_{ew} = l_e + l_w$) is held fixed at the following values: {0 ft, 2 ft, 3.5 ft, 5.5 ft, 7.5 ft}. The case where $l_{ew} = 0$ ft is the baseline case, which has no extension or winglet. The other cases are labeled Designs A, B, C, and D, for $l_{ew} = \{2 \text{ ft}, 3.5 \text{ ft}, 5.5 \text{ ft}, 7.5 \text{ ft}\}$, respectively.

6.3.1 Results: Cruise speed = 250 knots

The baseline design for the optimization is the optimized wing with no extension and winglet. Since the cruise speed is 250 knots, the whirl flutter speed must be at least 330 knots for maintaining a safety factor of 1.33. Only the wing weight needs to be minimized for the baseline case, since the variables influencing L/D (extension and winglet variables) are absent. The following fitness function is used for optimization:

$$\text{fitness} = \frac{W}{W_0} - \frac{L/D}{(L/D)_0} \tag{6.1}$$

where W_0 and $(L/D)_0$ are the wing weight and L/D of the baseline case.

The optimum designs for all the cases considered are tabulated in Table 6.2. All the designs have the same whirl flutter speed and wing loading. The optimum extension span for all the designs is less than 1 ft, and the optimum cant angle is less than 30 degrees. The optimum winglet span and height increase with l_{ew}.

The stiffness distribution and damping ratios of the optimized design are shown in Fig. 6.6, Fig. 6.7, Fig. 6.8, and Fig. 6.9 for $l_{ew} = 2$, 3.5, 5.5, and 7.5 ft, respectively. From these figures, we can see that the beamwise and chordwise stiffness decreases along span for all the designs, while the torsional stiffness is almost a constant for all values of wing-tip spans.

Table 6.2: Optimization results when cruise speed = 250 knots.

	Baseline	Design-A	Design-B	Design-C	Design-D
l_{ew} (ft)	0	2.0	3.5	5.5	7.5
Extension span (ft)	–	0.64	0.66	0.87	0.56
Winglet span (ft)	–	1.36	2.84	3.63	6.94
Winglet height (ft)	–	0.49	1.51	0.64	3.69
Winglet cant (deg)	–	20	28	11	23
t/c	21%	21%	21%	21%	21%
Wing Weight (lbs)	518	529	539	577	607
L/D	8.48	8.85	9.09	9.33	9.53
Fitness	0	-0.022	-0.031	0.014	0.048
WFS (kts)	330	330	330	330	330
Buckling safety	1.52	2.65	2.65	2.65	2.65
Laminate	$[0_{12}, \pm45_2]_S$	$[0_8, \pm45_3]_S$	$[0_8, \pm45_3]_S$	$[0_8, \pm45_3]_S$	$[0_8, \pm45_3]_S$
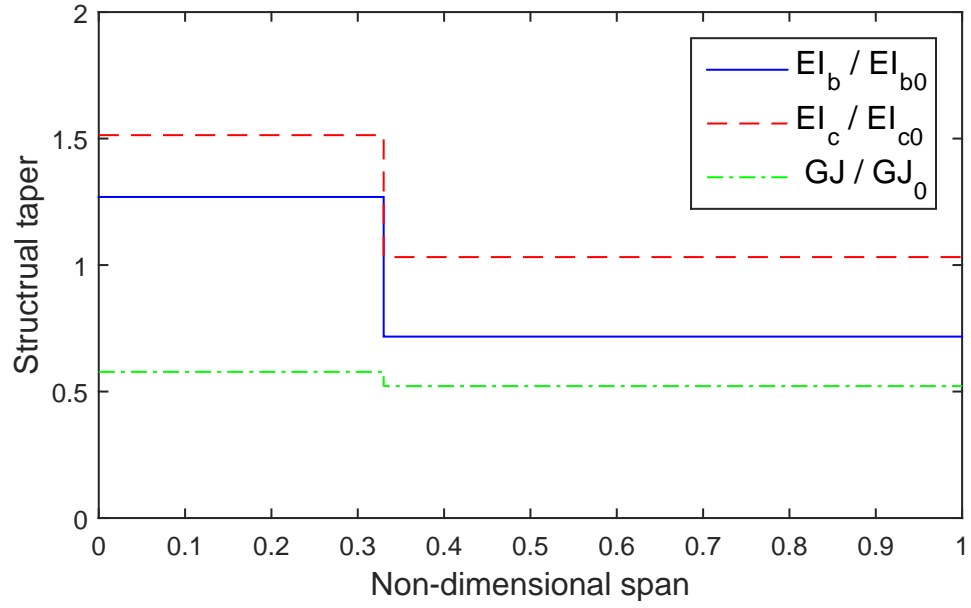
(a) Stiffness distribution.
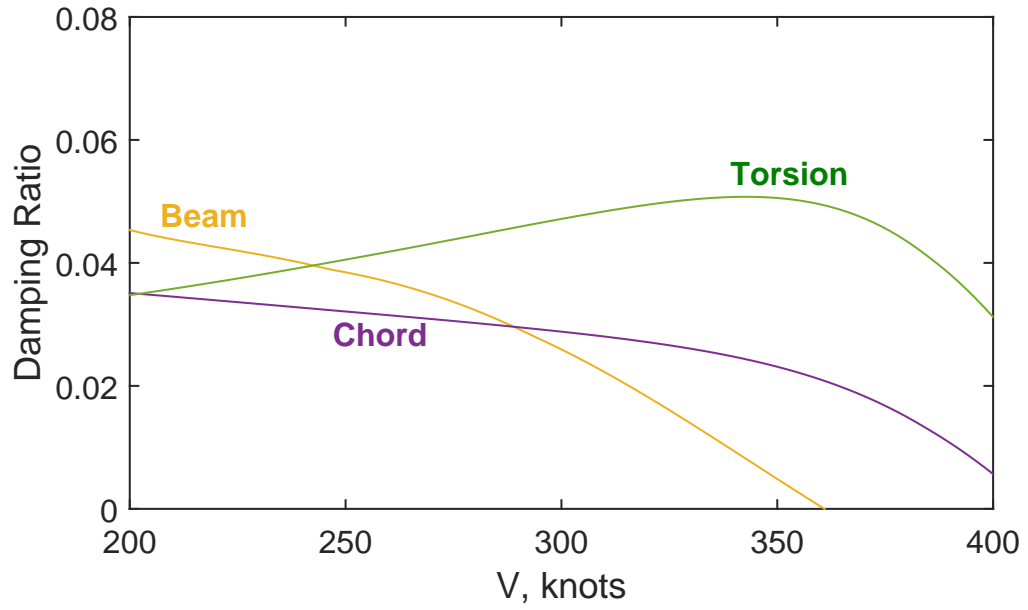
(b) Damping characteristics.

Figure 6.6: Stiffness distribution and damping ratios of the optimized design for $l_{ew} = 2$ ft and cruise speed = 250 knots.

(a) Stiffness distribution.

(b) Damping characteristics.

Figure 6.7: Stiffness distribution and damping ratios of the optimized design for $l_{ew} = 3.5$ ft and cruise speed = 250 knots.

(a) Stiffness distribution.

(b) Damping characteristics.

Figure 6.8: Stiffness distribution and damping ratios of the optimized design for $l_{ew} = 5.5$ ft and cruise speed = 250 knots.
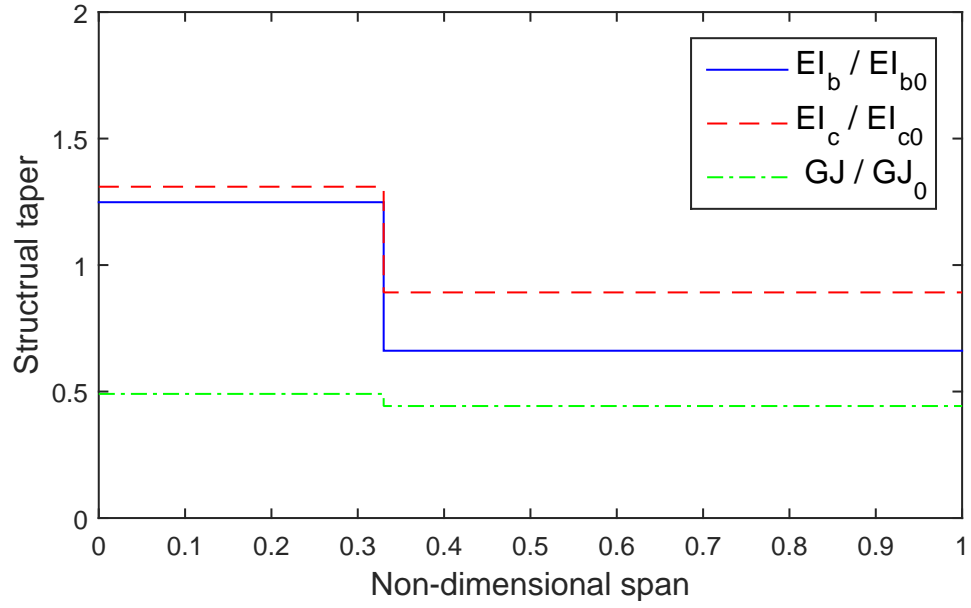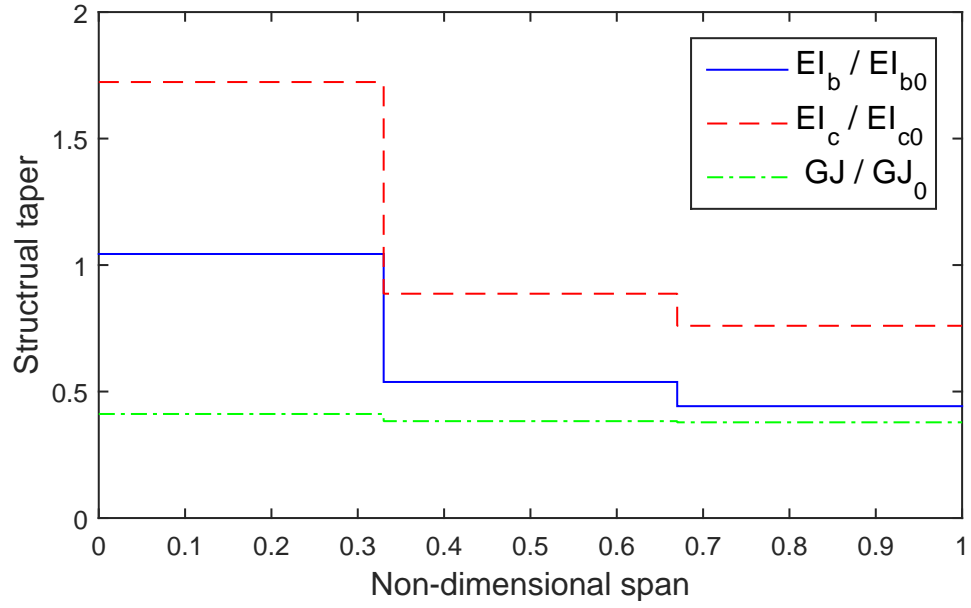
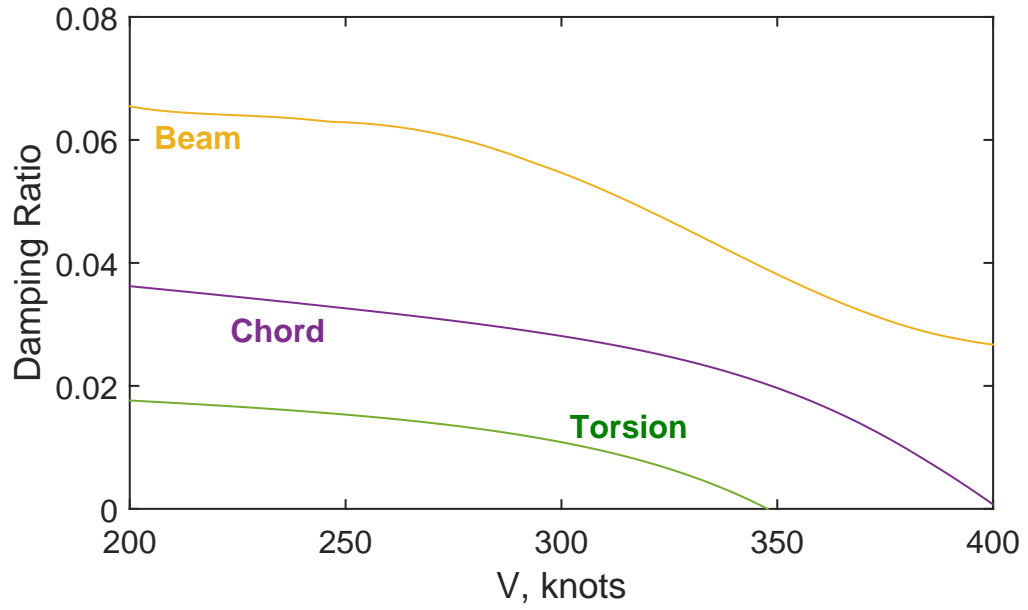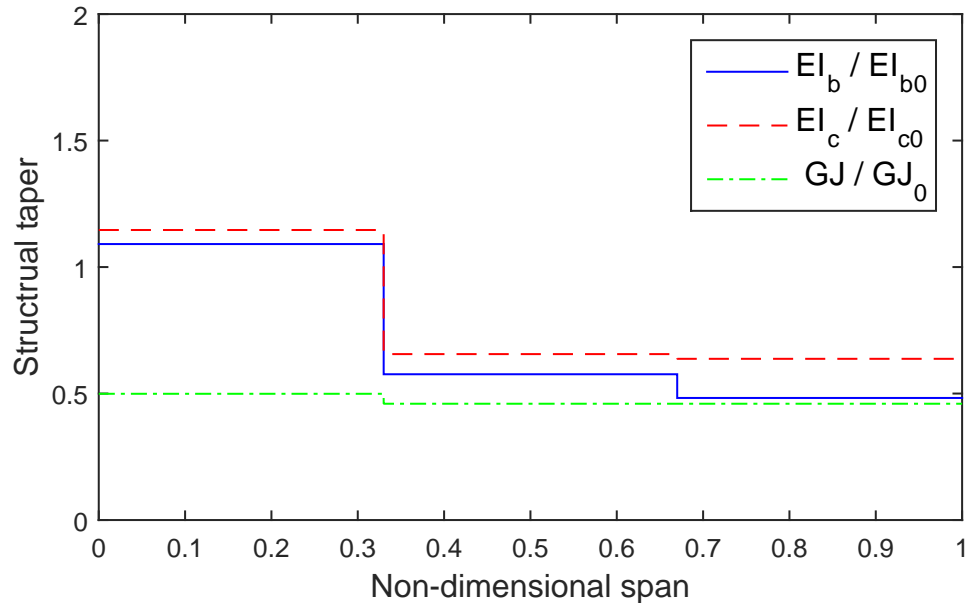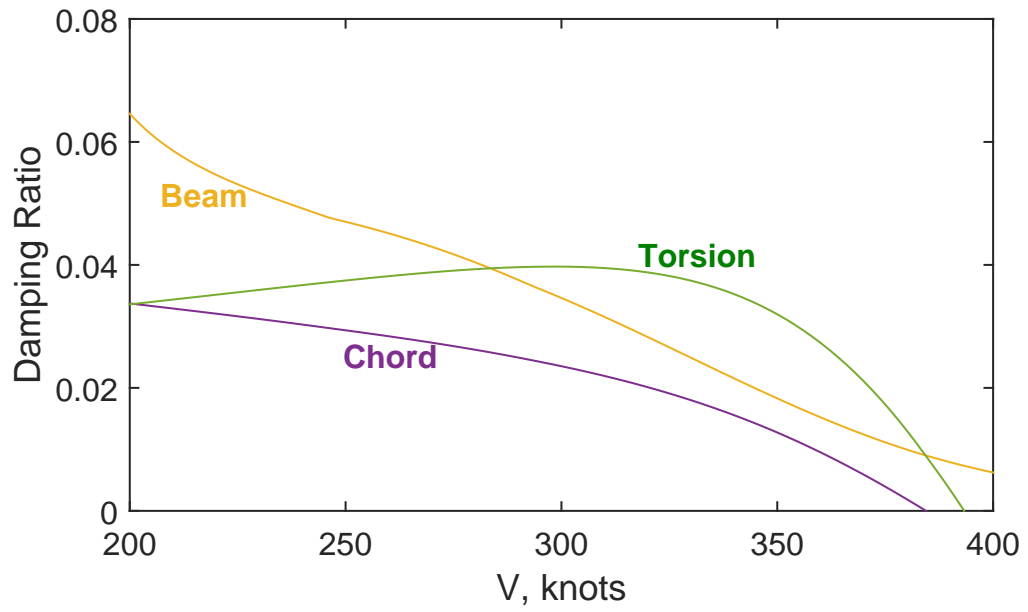(a) Stiffness distribution.

(b) Damping characteristics.

Figure 6.9: Stiffness distribution and damping ratios of the optimized design for $l_{ew} = 7.5$ ft and cruise speed = 250 knots.

6.3.2 Results: Cruise speed = 300 knots

The cruise speed is set to be 300 knots, and hence the whirl flutter speed must be at least 400 knots. The optimum designs for all the cases considered are tabulated in Table 6.3. All the designs have the same whirl flutter speed and wing loading. The optimum winglet spans increase with l_{ew}, while the optimum extension span is less than 1 ft for all the designs.

The stiffness distribution and damping ratios of the optimized design are shown in Fig. 6.10, Fig. 6.11, Fig. 6.12, and Fig. 6.13 for $l_{ew} = 2$, 3.5, 5.5, and 7.5 ft, respectively. From these figures, we can see that the stiffness in beamwise and chordwise direction decreases, while the torsional stiffness is almost a constant, similar to previous case where cruise speed is 250 knots. Also, the whirl flutter speed is close to 400 knots for all the cases.

From Tables 6.2 and 6.3, we can see that the optimum L/D reduces as cruise speed increases. This can be attributed to the fact that the fuselage profile drag increases with the square of cruise speed – reducing L/D significantly. Also, the optimum wing weight increases with cruise speed, as the stiffness required to maintain the whirl flutter boundary increases – making the wing heavier.

Table 6.3: Optimization results when cruise speed = 300 knots.

|	Baseline	Design-A	Design-B	Design-C	Design-D
l_{ew} (ft)	0	2.0	3.5	5.5	7.5
Extension span (ft)	–	0.52	0.51	0.82	0.50
Winglet span (ft)	–	1.48	2.99	4.86	7.00
Winglet height (ft)	–	1.69	3.21	1.61	1.87
Winglet cant (deg)	–	47	46	19	15
t/c	21%	21%	21%	21%	21%
Wing Weight (lbs)	529	537	544	589	607
L/D	6.52	6.71	6.82	6.92	7.00
Fitness	0	-0.014	-0.0177	0.052	0.073
WFS (kts)	400	400	400	400	400
Buckling safety	1.43	2.33	2.65	2.88	2.88
Laminate	$[0_{12}, \pm 45_2]_S$	$[0_{10}, \pm 45_2]_S$	$[0_8, \pm 45_3]_S$	$[0_6, \pm 45_4]_S$	$[0_6, \pm 45_4]_S$
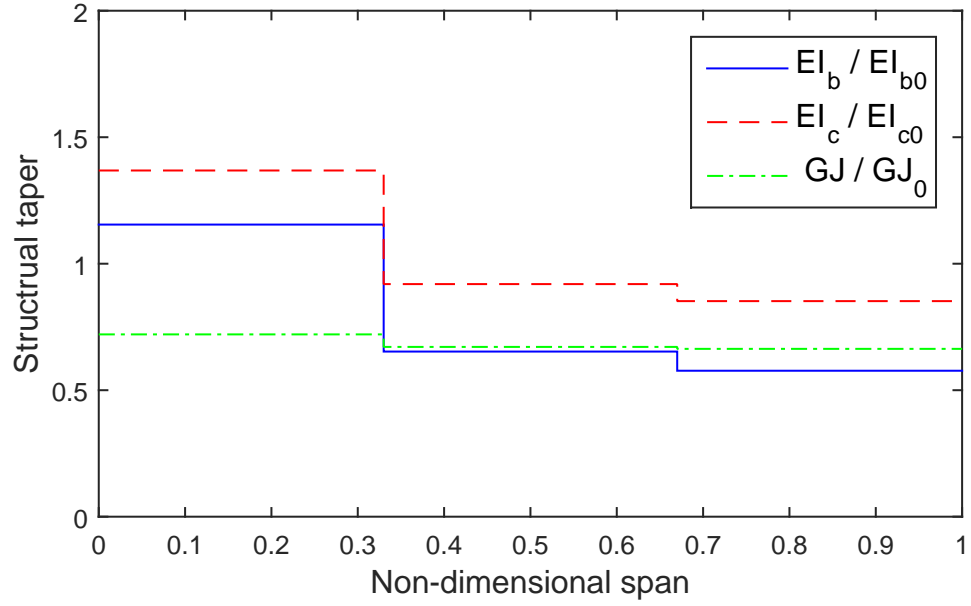
(a) Stiffness distribution.
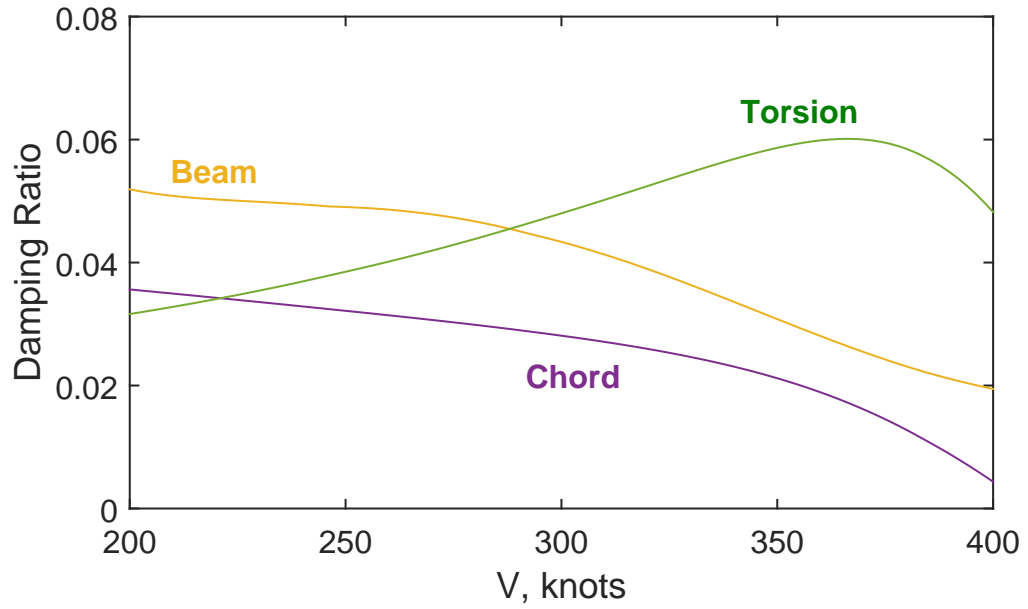
(b) Damping characteristics.

Figure 6.10: Stiffness distribution and damping ratios of the optimized design for $l_{ew} = 2.0$ ft and cruise speed $= 300$ knots.
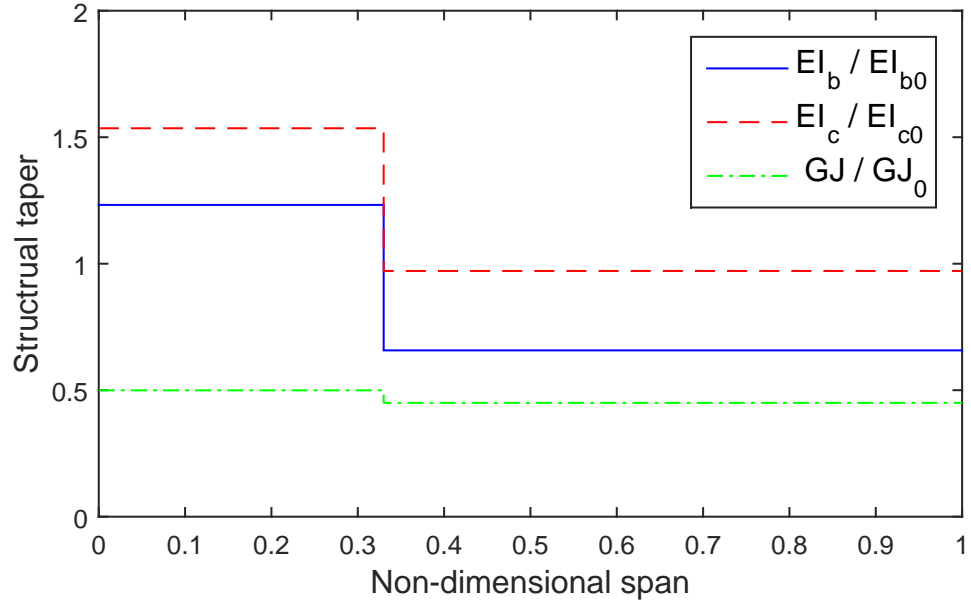
(a) Stiffness distribution.
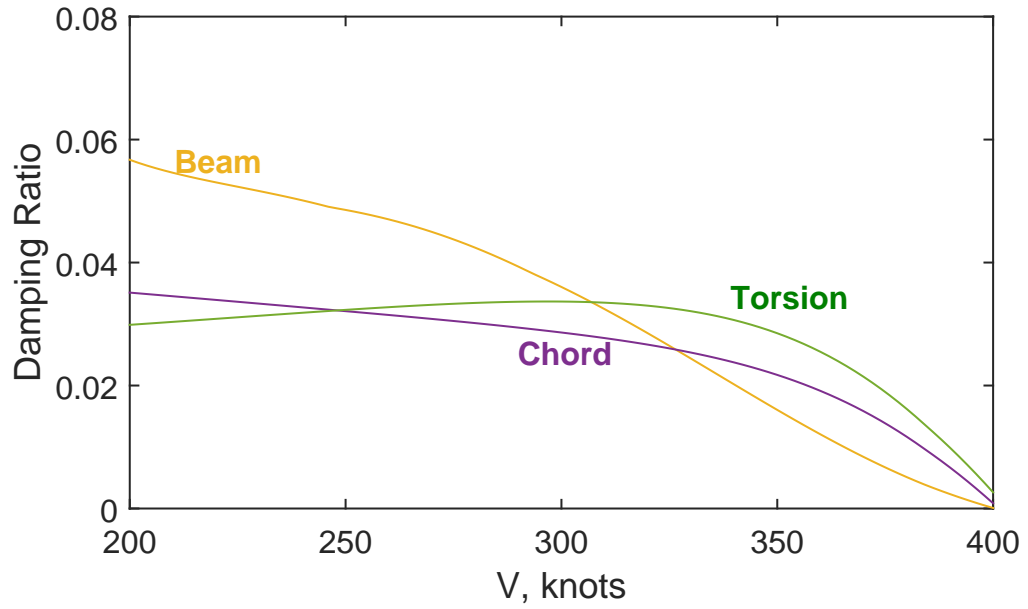
(b) Damping characteristics.

Figure 6.11: Stiffness distribution and damping ratios of the optimized design for $l_{ew} = 3.5$ ft and cruise speed $= 300$ knots.
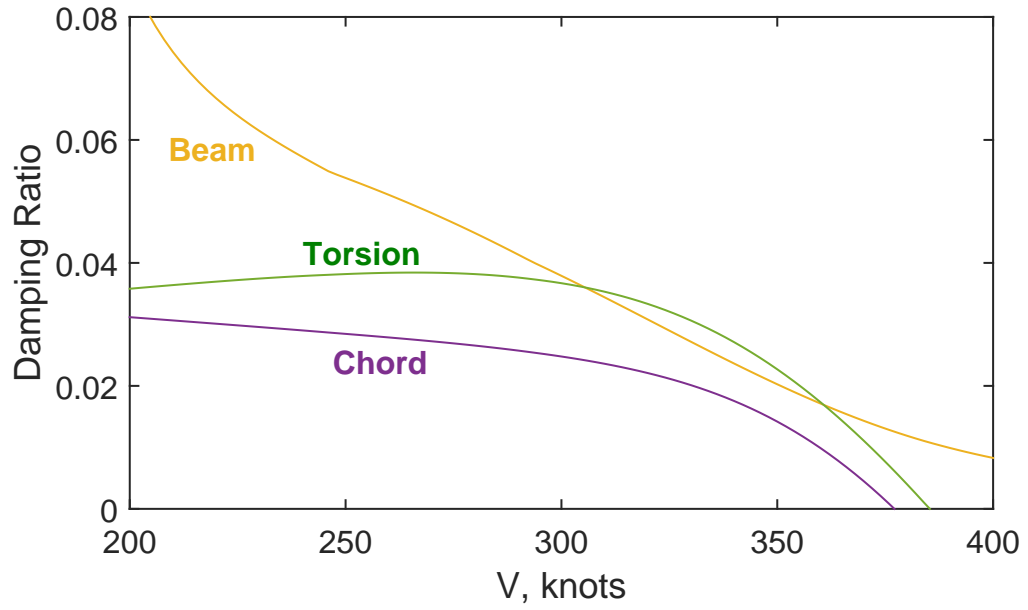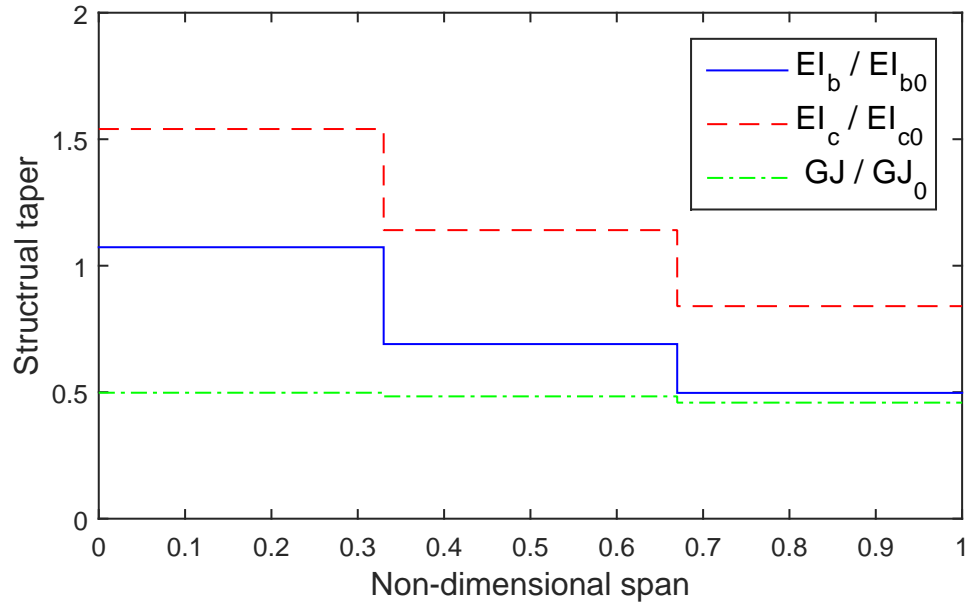
(a) Stiffness distribution.
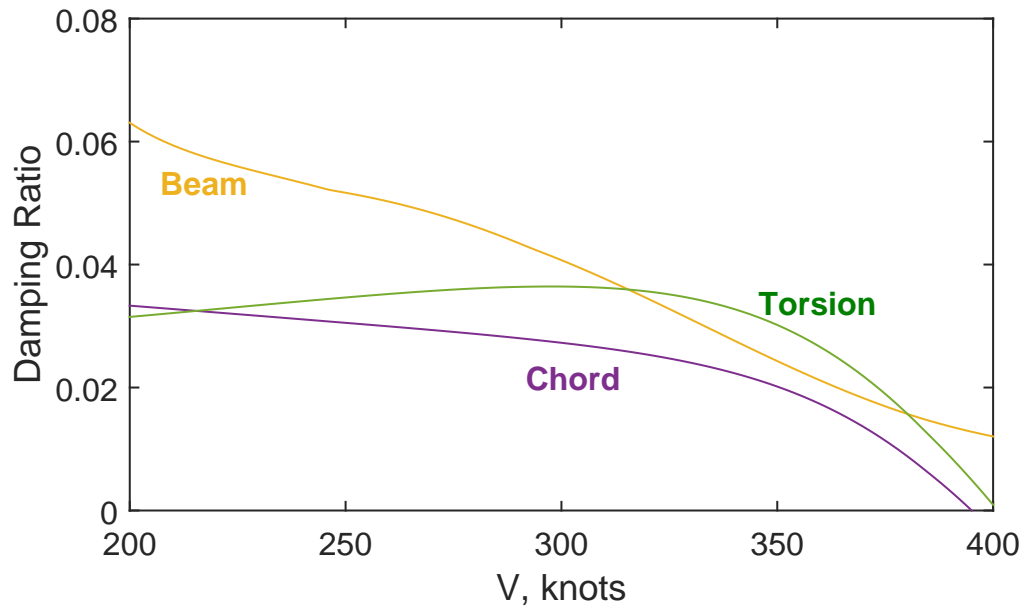
(b) Damping characteristics.

Figure 6.12: Stiffness distribution and damping ratios of the optimized design for $l_{ew} = 5.5$ ft and cruise speed $= 300$ knots.
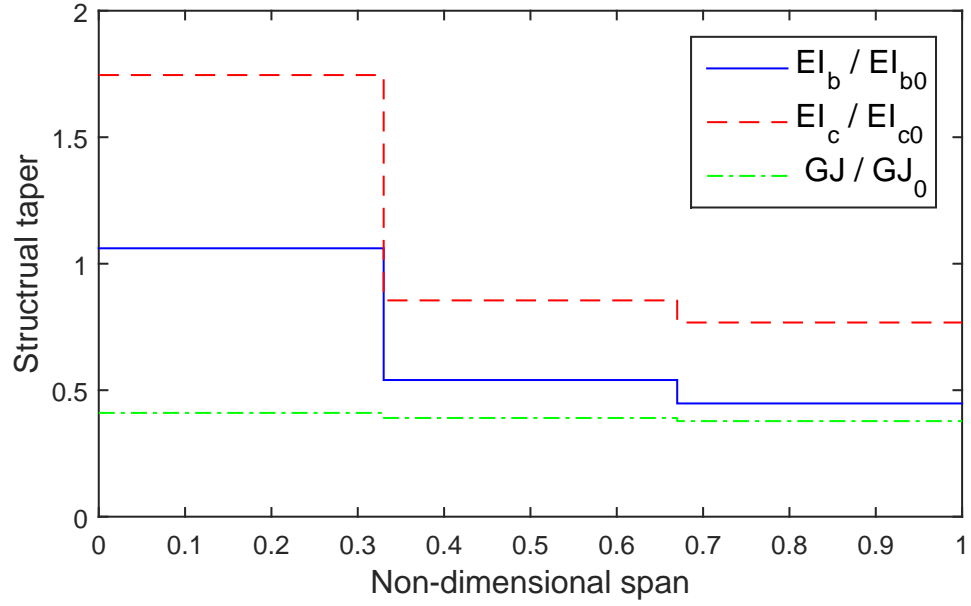
(a) Stiffness distribution.
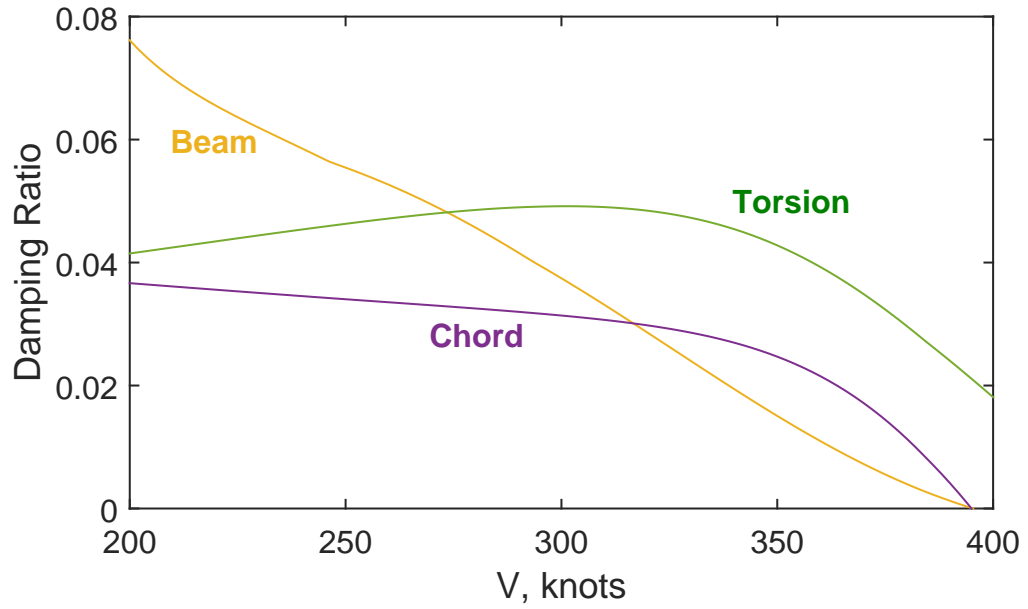
(b) Damping characteristics.

Figure 6.13: Stiffness distribution and damping ratios of the optimized design for $l_{ew} = 7.5$ ft and cruise speed = 300 knots.

6.3.3 Discussion: Fitness

The fitness (Eq. (6.1)) of all the optimal designs is shown in Fig. 6.14 for cruise speeds of both 250 knots and 300 knots. From Fig. 6.14, we can see that the best fitness is achieved for $l_{ew} = 3.5$ ft for both the cruise speeds considered. Specifically, the optimum fitness is -0.031 and -0.017 for cruise speeds of 250 knots and 300 knots, respectively.
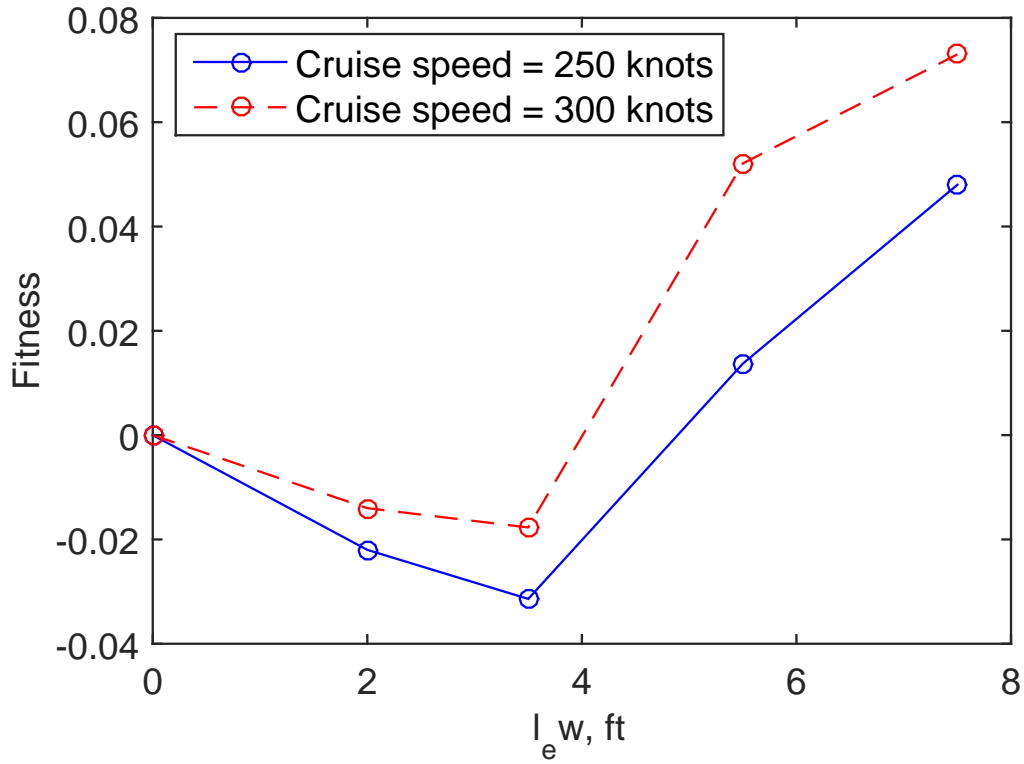
Figure 6.14: Fitness values for all the optimal designs.

The L/D and wing weights of optimal designs are shown in Fig. 6.15 and Fig. 6.16 for 250 knots and 300 knots, respectively. From Fig. 6.15 and Fig. 6.16, we can see that the for lower values of wing-tip span (l_{ew}), weight penalty (W/W_0) is small compared to the increase in efficiency $((L/D)/(L/D)_0)$. For higher values of wing-tip span, the weight penalty is comparable or even more than the increase in efficiency.
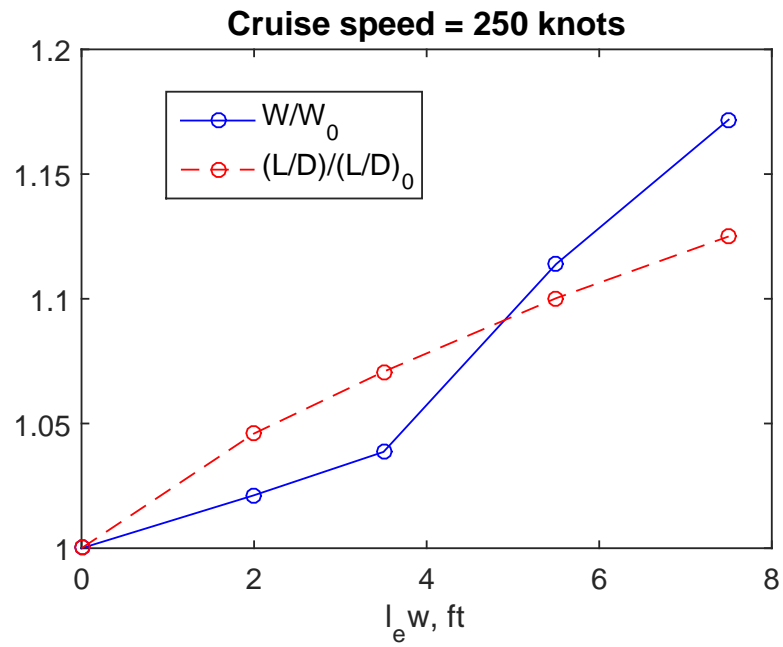
Figure 6.15: L/D and wing weights of optimal designs for cruise speed = 250 knots.
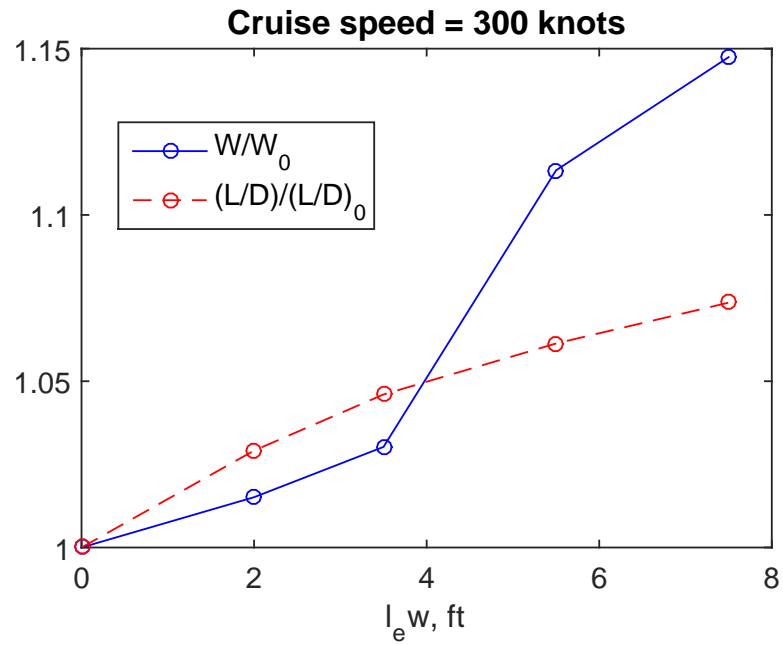
Figure 6.16: L/D and wing weights of optimal designs for cruise speed = 300 knots.

6.3.4 Discussion: Range

The optimum designs are substituted in the Breguet range equation [60], which computes the maximum range R for a propeller driven aircraft with a given L/D, empty weight, and specific fuel consumption (SFC). The Breguet range equation is

$$R = \frac{1000}{SFC} \frac{L}{D} \log \left(1 + \frac{W_F}{W_E}\right) \qquad (6.2)$$

where W_F is the fuel weight and W_E is the empty weight.

The range of the optimum designs, normalized by the range of the baseline (R_0), is shown in Fig. 6.17. From Fig. 6.17, we can see that for cruise speed equal to 250 knots, the optimized design where $l_{ew} = 3.5$ ft gives 5.5% more range than the baseline. For cruise speed = 300 knots, the optimized design where $l_{ew} = 3.5$ ft gives 3.3% more range than the baseline.
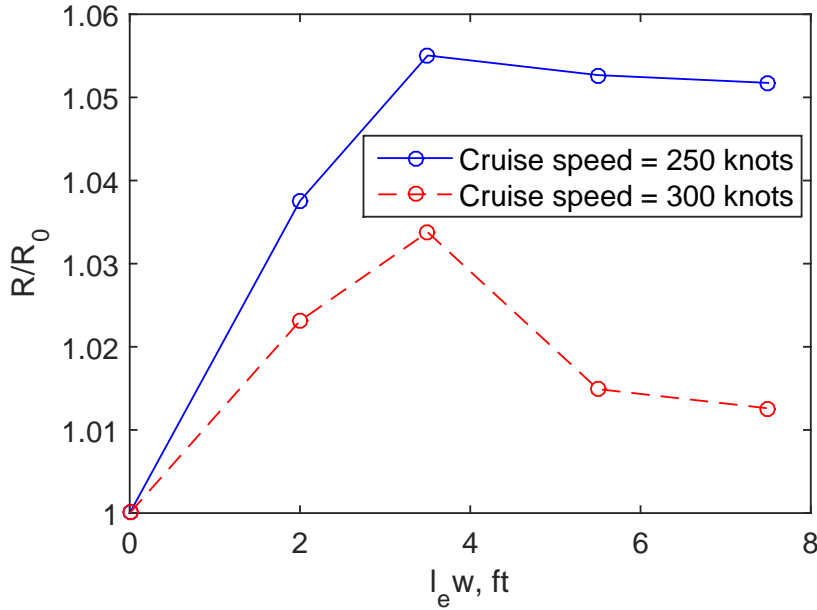
Figure 6.17: Range of the optimum designs for cruise speed = 250 knots and 300 knots.

6.3.5 Discussion: Range Specific Transport Efficiency

The Range Specific Transport Efficiency (RSTE), suggested by Lieshman [61], is a useful metric to evaluate tiltrotor performance when the range is fixed. The RSTE is the ratio of the payload weight transported to the fuel consumed for a specific transport range. The expression for RSTE is

$$RSTE = \frac{W_G - W_E - W_F}{W_F} \tag{6.3}$$

where W_G is the aircraft gross weight, W_E is the aircraft empty weight, and W_F is the fuel weight.

The RSTE values for the optimum designs are shown in Fig. 6.18 for cruise speeds equal to 250 knots and 300 knots. From Fig. 6.18, we can see that the for cruise speed equal to 250 knots, the RSTE increases from 1.03 for the baseline to 1.21 for the optimum design with $l_{ew} = 7.5$ ft. For cruise speed equal to 300 knots, the RSTE increases from 1.02 for the baseline to 1.12 for the optimum design with $l_{ew} = 3.5$ ft.
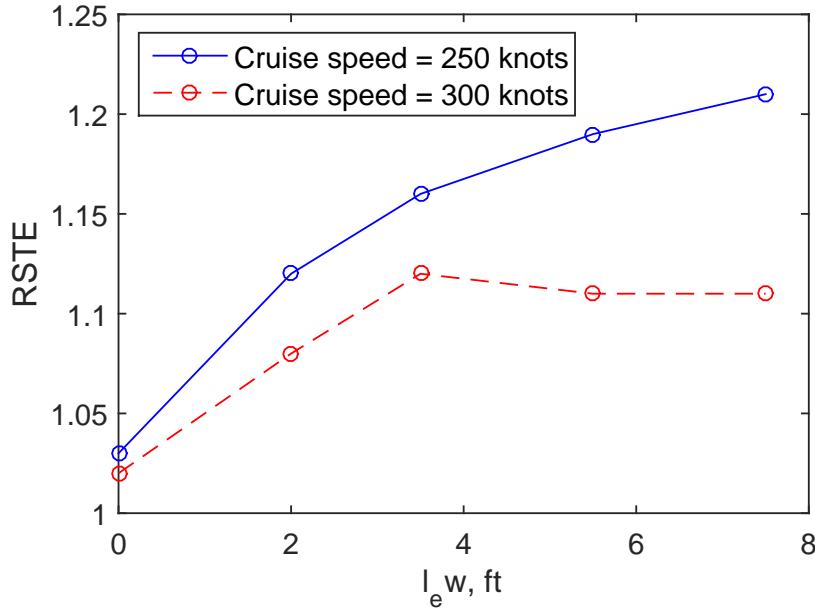
Figure 6.18: RSTE values for the optimum designs for cruise speed = 250 knots and 300 knots.

Chapter 7 | Conclusions and Recommendations

The investigation of combined structural and aerodynamic design and optimization of a tiltrotor is performed. An aeroelastic analysis and a wing structural analysis model is developed for analyzing tiltrotor wings with extensions and winglets. The aeroelastic and structural analysis models are merged with an existing aerodynamic analysis model for the optimization.

7.1 Aeroelastic Model

The aeroelastic model has 12 DOFs and takes into account the rotor blade torsion degree of freedom. Parametric studies of the structural taper, composite couplings, stiffness of the wing and wing extension, on whirl flutter are conducted. The parametric study is followed by an optimization study, where the optimal combinations of these parameters to maximize the whirl flutter speed are computed. The following conclusions can be drawn based on this study:

1. The rotor blade torsion degree of freedom is destabilizing to whirl flutter, reducing the whirl flutter speed by 35 % (100) knots (consistent with previous studies).

2. The wing-tip devices continue to improve the beam and torsion mode stability, even after adding the blade torsion degree of freedom. However, they do not have a significant influence on the chord mode.

3. Structural taper increases the tip deflection, and hence the wing extensions are more efficient in increasing the beam mode damping – by 15% (45 knots) when the wing has a structural taper. The chord and torsion modes are, however, not affected by structural taper.

4. A wing extension, which is swept back or located aft of the wing, can aerodynamically couple the beam and torsion modes. Such an extension destabilizes the beam mode, while stabilizing the torsion mode, if the modeshape of the beam mode has a flap-up nose-up type of coupling.

5. The optimized design has an improved flutter speed of 22% (65 knots) more than that of the baseline design. The beam mode is the least stable mode in the baseline design, while the chord and torsion modes are the least stable modes in the optimized design.

6. The optimization is performed by setting the bending-torsion composite coupling parameters to zero. The resulting optimum design also has a 22% (65 knots) increase in flutter speed. Thus, maximum gains in flutter speed can be achieved without using the composite coupling parameters.

7. The aeroelastic optimization study is validated using RCAS, a commercial software for performing comprehensive rotorcraft analyses. The analytical model and the optimization results agree well with RCAS.

7.2 Structural Model

A wing structural model – to compute the wing stiffness, strength, buckling load, and weight for a given wing geometry, planform variables, material properties, and torque box dimensions is developed. The wing stiffness and strength are computed using an analysis based on Vlasov therory [53]. The laminate buckling load is calculated using the Ritz method with 25 admissible functions. The structural model is exercised by successfully designing a wing which has a similar characteristics of the XV-15 wing. The designed wing was made sure that it can handle 2g jump take off loads and 4g pull up loads loads. The following conclusions can be drawn from the parametric studies conducted on the structural model:

1. Reducing the thickness of the designed wing from 23% t/c to 15% t/c decreases the strength. The thin wing is reinforced by adding unidirectional plies, which increased the strength of the 15% wing.

2. Reducing the thickness also reduces the stiffness of the thin wing – affecting the aeroelastic stability of the wing – even after the thin wing is reinforced with unidirectional plies. The damping of the beam and torsion modes decreases significantly when the thickness is decreased from 21% to 15%.

7.3 Aerodynamic Model

An existing aerodynamic model called Polar Generation Software (PGEN), which was developed to analyze the performance of sailplanes, is used to compute the aerodynamic performance of tiltrotors equipped with wing extensions and winglets. Parametric studies are conducted on the effects of wing, extension, and winglet planform variables on the lift-to-drag ratio. The following conclusions can be drawn from this study:

1. Adding an extension of span 4.5 ft and a winglet of height 4.5 ft on a 1.67 semi-span wing increases L/D by over 9%

2. Decreasing the wing thickness from 21% to 15% increases the drag by only 1%, as at high-speeds, the fuselage drag is the dominant source of drag.

3. Wing-tip devices are more effective in increasing the L/D of the tiltrotor at higher altitudes, as the cruise c_l increases with altitude.

7.4 Optimization

A multi-objective optimization methodology for tiltrotor aircraft is developed, where the weight penalty due to extensions and winglets is minimized while maximizing L/D, subject to strength, buckling, wing loading, and whirl flutter constraints. The aeroelastic, aerodynamic, and the structural models developed are merged together for the optimization study. The wing design variables are wing thickness, the torque box skin laminate orientation angles, number of plies, stringer locations, and stringer areas. The extension design variables are the span, taper, sweep, and

incidence angles. The winglet design variables are its taper, height, cant, toe, and twist angles. The wing thickness and the extension span effect both structural and aerodynamic properties of the aircraft. The following conclusions can be drawn from the optimization study:

1. The results show that achieving the stiffness criteria (for whirl-flutter constraints) is possible with fewer plies on thick wings than on thin wings. This implies that thick wings can be lighter than the thin wings while providing adequate whirl-flutter stability.

2. For cruise speed = 250 knots, the optimal design has an increased L/D of 7% for a weight penalty of 3% over the baseline.

3. For cruise speed = 300 knots, the optimal design has an increased L/D of 5% for a weight penalty of 2.5% over the baseline.

4. The optimal designs for cruise speeds of 250 knots and 300 knots have a better transport range of over 5.5% and 3.5%, respectively, over the baseline.

5. When the transport range is fixed, the RSTE can be used as metric to evaluate performance. The optimal design for cruise speed of 250 knots and 300 knots increase the RSTE from 1.03 to 1.21, and from 1.02 to 1.12, respectively.

7.5 Recommendations for Future Work

The research presented in this dissertation is focused on conducting parametric and optimization studies on improving the performance of tiltrotors by using wing extensions and winglets. This section discusses recommendations for future work on tiltrotor wing design using extensions and winglets.

7.5.1 Validating the Aerodynamic Model of the Wing-Nacelle-Extension with Wind-Tunnel Data

A 6% scale model of the NASA Large Civil Tilt Rotor (LCTR) was tested without rotors in airplane mode at NASA Ames Research Center [62]. The purpose of the test was to collect data for validating their computational fluid dynamics tools. Measurements of lift, drag, and moments were acquired for isolated wing and various wing-tip configurations. The study concluded with the following interesting observations:

1. The addition of the nacelle to the LCTR isolated wing produced an increase in lift – due to the end-plating effect of the nacelle. However the L/D decreased due to a larger increase in drag.

2. The addition of the extension to the nacelle decreased overall drag. The authors claimed that this result may be due to the complex interactions between the nacelle and the wing extension.

The aerodynamic model used in the current dissertation can be validated with the experimental data and the above observations. This validation study can shed some light on the end-plating effect of the nacelle and the aerodynamic interactions between extension and winglet – by qualitatively as well as quantitatively examining their effects on lift and drag of the airframe.

7.5.2 Experimental Validation of Aeroelastic Effects of Extensions and Winglets

Wind-tunnel tests on semi-span whirl flutter models are presented in [2]. The wing is fabricated using composite laminates, with an integrated spar that acted as a flexure. The stiffness of the flexure was tuned so that the wing vibrated at desired frequencies. The model exhibited whirl flutter at a tunnel speed of 101 ft/s. The test data was validated with the aeroelastic analysis presented in this dissertation. However, the models developed in Ref. 2 did not include wing extensions or winglets. Also, the non-dimensional frequencies of the wing used in Ref. 2 does not represent typical tiltrotors.

Wind-tunnel models which are similar to the models presented in Ref. 2 can be fabricated such that (a) the wing frequencies represent typical tiltrotors; and (b) the wings are equipped with extensions and winglets. The structural properties of the proposed wind-tunnel wing and the XV-15 tiltrotor wing are tabulated in Table. 7.1. We can see from Table. 7.1 that the non-dimensional properties of the proposed model are approximately equal to the XV-15.

Such a scaled-down wind-tunnel model helps us to quantify the effects of the extension and winglet on the original tiltrotor. For example, the beam mode damping predictions of the scaled-down model, with and without an extension are shown in Fig. 7.1. These damping results in Fig. 7.1 can be scaled up and can be used to predict the damping ratios of the XV-15 tiltrotor (shown in Fig. 7.2). The damping results presented in Fig. 7.2 show that the damping of the beam mode of the XV-15 is unstable at 380 knots; and adding an extension increases the damping and stabilizes the beam mode.

Table 7.1: The properties of the proposed wind-tunnel wing and the XV-15 tiltrotor wing.

Item	XV-15	Scaled-down
Dimensional		
Rotor radius, R (ft)	12.5	0.712
Rotor RPM (rad/s)	48	125
Wing semi-span, b (ft)	16.67	0.94
EI_b ($lb-ft^2$)	3.3E7	20
EI_c ($lb-ft^2$)	8.5E7	40
GJ ($lb-ft^2$)	1.6E7	17
Non-Dimensional		
Lock number	3.83	3.24
Beam frequency	0.42	0.46
Chord frequency	0.70	0.65
Torsion frequency	1.3	1.26
b/R	1.33	1.33
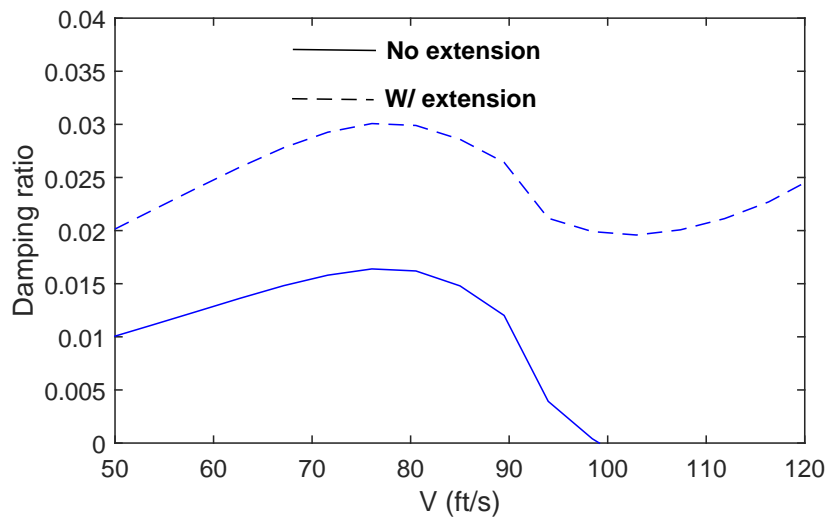
Figure 7.1: Damping predictions for the beam mode for the wind-tunnel model.
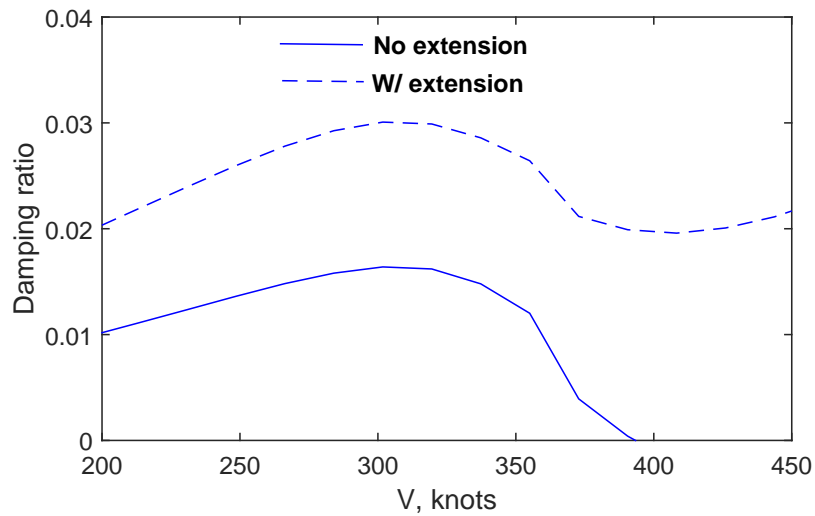
Figure 7.2: Damping predictions for the beam mode for the XV-15, predicted by scaling up the results from the scaled down model.

7.5.3 Whirl Flutter Alleviation Using Flexible Torque Tubes

In Section 3.1.5, we showed that reducing the bending stiffness of the extension can significantly improve the damping of the beam mode. Similarly, the torsional stiffness of the extension can be made sufficiently flexible so that it can improve the damping of the wing. Specifically, the extension can be attached to the wing by means of a flexible torque tube. Such flexible torque tubes were proposed by Miller [32].

The stiffness and location of the tube can be tailored such that the extension experiences a nose-down pitching moment whenever the wing flaps up – thus creating an aerodynamic force opposing the motion of the wing and increasing damping. Applications of such flexible torque tubes are discussed in Ref. 31.

For example, if the torsional stiffness of the torque tube is tailored to 10% of the torsional stiffness of the wing, and is located 3 ft aft of the aerodynamic center of the wing, the perturbational forces create a nose-down pitching moment and thus increasing damping. The damping ratio of the beam and torsion modes of the wing using flexible torque tubes is shown in Fig. 7.3, where we can see that the flexible torque tube increases that damping of the beam mode. Thus, other means of alleviating whirl flutter using flexible torque tubes can be investigated.
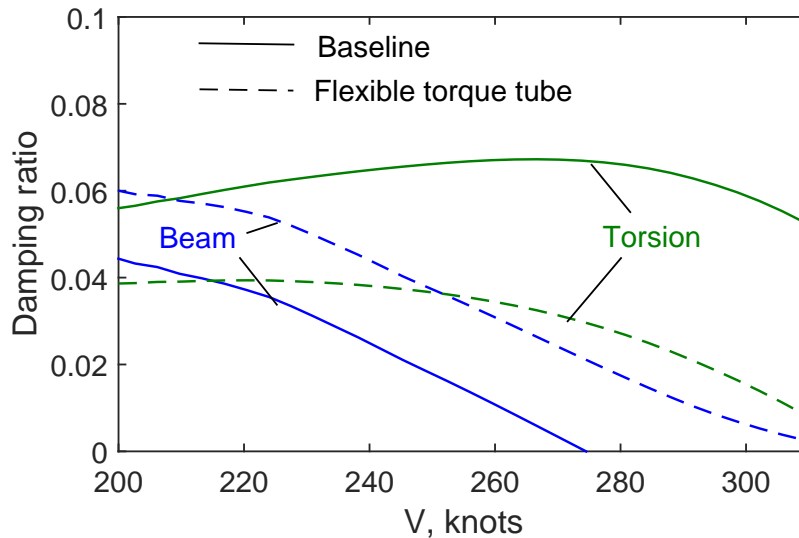
Figure 7.3: Damping predictions for the beam and torsion modes for the flexible torque tubes.

7.5.4 Conducting Optimization Studies Using the Standard Weight Model

In Ref. 63, a method is developed and described for estimating the wing weights of tiltrotors at a conceptual level and development. This method is based on dynamically scaling the wing stiffness requirements, and is used in Ref. 4 to compute the weight of a thin composite wing representative of a high-speed tiltrotor. The key parameters required for this method are

1. Wing planform and cross-section geometry

2. Wing beamwise, chordwise, and torsional frequencies

3. Wing torque box cross-sectional and wing spar cap area and geometry

4. Ultimate load factors for the wing for pull-up maneuver and landing

This method can be used to validate the wing structural model and to conduct optimization studies.

7.5.4.1 Validation of the Wing Structural Model

The following approach can be followed for validating the wing weight model developed in this dissertation with the wing weight model presented in Ref. 63:

1. Start with an optimum design in presented in Chapter-6.

2. Compute the wing beamwise, chordwise, and torsional frequencies (at zero forward speed) using the analysis presented in Chapter-3.

3. Compute the torque box and cross-sectional wing spar cap area and geometry (which are outputs of the structural analysis used in Chapter-4).

4. Compute bending moment at the root based on the loads for 2g jump takeoff and 4g pull up (aerodynamic analysis in Chapter-5) maneuver.

5. Compare the weights of the optimum designs presented in Chapter-5 versus the wing weights computed using the standard tiltrotor wing weight model.

7.5.4.2 Conducting Optimization Studies

The standard structural tiltrotor model can be used for the multi-objective optimization presented in Chapter-6, section 6.1. In order to do this, the optimization flowchart needs to be modified as shown in Fig. 7.4. The modifications are:

1. The root bending moments M_b, based on the loads generated by the aerodynamic analysis, and the wing planform area S_W are given to the wing weight model.

2. The wing structural analysis computes the wing frequencies for beamwise bending, chordwise bending, and torsion $(\omega_b, \omega_c, \omega_t)$. These frequencies are inputs to the wing weight model.

3. The wing weight model uses M_b, ω, S_W and computes the wing weight, which is given to the optimizer as an objective.
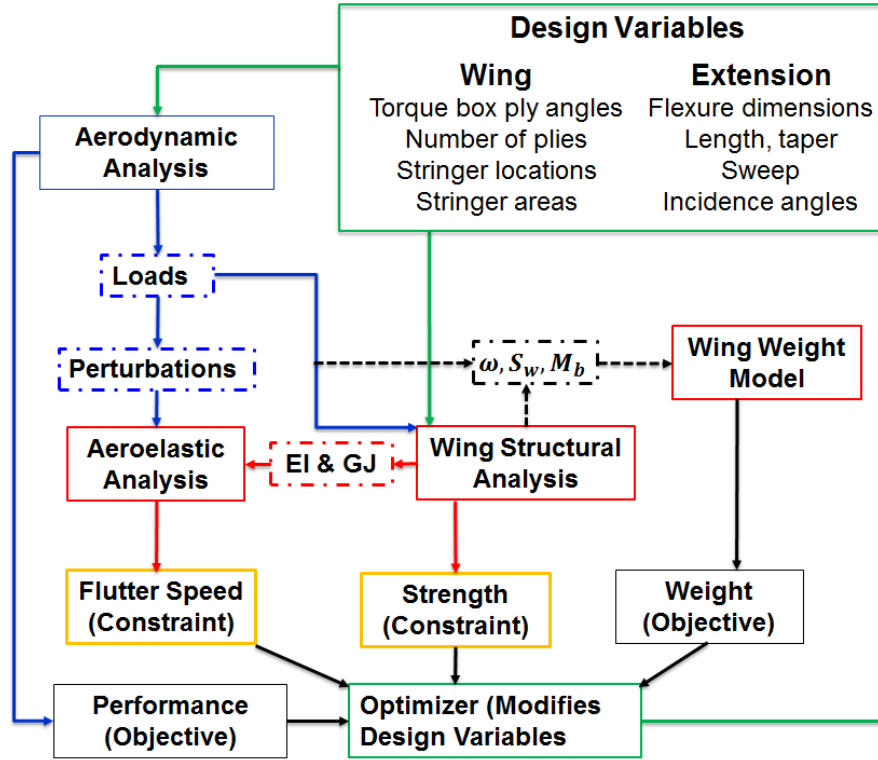
Figure 7.4: Optimization flowchart using the standard tiltrotor weight model.

Appendix | Appendix-A

The rotor/wing matrices $M_R = MR$, $C_R = CR$, and $K_R = KR$ are 14×14 matrices. The non-zero terms are listed below. Some of the parameters appearing in the listing are defined as follows:

```
MR(1,1) = 2*Mb;
MR(1,3) = 2*Mb*csl*h;
MR(1,5) = 2*Mb*h*snl;
MR(1,9) = Sz;
MR(2,2) = gam*((2*Mb*csl^2)/gam + (2*Mb*snl^2)/gam);
MR(2,4) = -2*Mb*h*snl;
MR(2,8) = -Sz*snl;
MR(2,10) = 2*Sb0*csl;
MR(3,1) = 2*Mb*csl*h;
MR(3,3) = 2*I0*snl^2 + 2*Mb*csl^2*h^2;
MR(3,5) = 2*Mb*csl*h^2*snl - 2*I0*csl*snl;
MR(3,9) = Sz*csl*h;
MR(3,11) = 2*Iz0al*snl;
MR(4,2) = -2*Mb*h*snl;
MR(4,4) = 2*Mb*h^2;
MR(4,8) = Sz*h;
MR(5,1) = 2*Mb*h*snl;
MR(5,3) = 2*Mb*csl*h^2*snl - 2*I0*csl*snl;
MR(5,5) = 2*I0*csl^2 + 2*Mb*h^2*snl^2;
MR(5,9) = Sz*h*snl;
```

```
MR(5,11) = -2*Iz0al*csl;
MR(6,3) = -Ibal*csl;
MR(6,5) = -Ibal*snl;
MR(6,6) = Ib;
MR(7,4) = Ibal;
MR(7,7) = Ib;
MR(8,2) = -Sz*snl;
MR(8,4) = Sz*h;
MR(8,8) = Iz;
MR(9,1) = Sz;
MR(9,3) = Sz*csl*h;
MR(9,5) = Sz*h*snl;
MR(9,9) = Iz;
MR(10,2) = Sb0*csl;
MR(10,10) = Ib0;
MR(11,3) = Iz0al*snl;
MR(11,5) = -Iz0al*csl;
MR(11,11) = Iz0;
MR(12,12) = Ip;
MR(13,4) = Ip;
MR(13,13) = Ip;
MR(14,3) = Ip*csl;
MR(14,5) = Ip*snl;
MR(14,14) = Ip;
CR(1,1) = Hu*gam;
CR(1,3) = Hu*csl*gam*h;
CR(1,4) = -Hb_d*gam;
CR(1,5) = Hu*gam*h*snl;
CR(1,7) = -Hb_d*gam;
CR(1,9) = Hz_d*gam;
CR(2,2) = -gam*(2*Tlam*csl^2 - Hu*snl^2);
CR(2,3) = -gam*(Hb_d*csl*snl - 2*Tz_d*csl*snl);
CR(2,4) = -Hu*gam*h*snl;
CR(2,5) = -gam*(2*Tz_d*csl^2 + Hb_d*snl^2);
```

```
CR(2,6) = Hb_d*gam*snl;
CR(2,8) = -Hz_d*gam*snl;
CR(2,10) = -2*Tb_d*csl*gam;
CR(2,11) = 2*Tz_d*csl*gam;
CR(3,1) = Hu*csl*gam*h;
CR(3,2) = -2*Qlam*csl*gam*snl;
CR(3,3) = 2*Qz_d*gam*snl^2 + Hu*csl^2*gam*h^2;
CR(3,4) = -Hb_d*csl*gam*h;
CR(3,5) = Hu*csl*gam*h^2*snl - 2*Qz_d*csl*gam*snl;
CR(3,7) = -Hb_d*csl*gam*h;
CR(3,9) = Hz_d*csl*gam*h;
CR(3,10) = -2*Qb_d*gam*snl;
CR(3,11) = 2*Qz_d*gam*snl;
CR(4,2) = -Hu*gam*h*snl;
CR(4,3) = Hb_d*csl*gam*h;
CR(4,4) = Hu*gam*h^2;
CR(4,5) = Hb_d*gam*h*snl;
CR(4,6) = -Hb_d*gam*h;
CR(4,8) = Hz_d*gam*h;
CR(5,1) = Hu*gam*h*snl;
CR(5,2) = 2*Qlam*csl^2*gam;
CR(5,3) = Hu*csl*gam*h^2*snl - 2*Qz_d*csl*gam*snl;
CR(5,4) = -Hb_d*gam*h*snl;
CR(5,5) = 2*Qz_d*csl^2*gam + Hu*gam*h^2*snl^2;
CR(5,7) = -Hb_d*gam*h*snl;
CR(5,9) = Hz_d*gam*h*snl;
CR(5,10) = 2*Qb_d*csl*gam;
CR(5,11) = -2*Qz_d*csl*gam;
CR(6,2) = -Mu*gam*snl;
CR(6,3) = Mb_d*csl*gam;
CR(6,4) = 2*Ibal + Mu*gam*h;
CR(6,5) = Mb_d*gam*snl;
CR(6,6) = -Mb_d*gam;
CR(6,7) = 2*Ib;
```

```
CR(6,8) = Mz_d*gam;
CR(7,1) = Mu*gam;
CR(7,3) = 2*Ibal*csl + Mu*csl*gam*h;
CR(7,4) = -Mb_d*gam;
CR(7,5) = 2*Ibal*snl + Mu*gam*h*snl;
CR(7,6) = -2*Ib;
CR(7,7) = -Mb_d*gam;
CR(7,9) = Mz_d*gam;
CR(8,2) = -Qu*gam*snl;
CR(8,3) = Qb_d*csl*gam;
CR(8,4) = Qu*gam*h;
CR(8,5) = Qb_d*gam*snl;
CR(8,6) = -Qb_d*gam;
CR(8,8) = Qz_d*gam;
CR(8,9) = 2*Iz;
CR(9,1) = Qu*gam;
CR(9,3) = Qu*csl*gam*h;
CR(9,4) = -Qb_d*gam;
CR(9,5) = Qu*gam*h*snl;
CR(9,7) = -Qb_d*gam;
CR(9,8) = -2*Iz;
CR(9,9) = Qz_d*gam;
CR(10,2) = -Mlam*csl*gam;
CR(10,3) = Mz_d*gam*snl;
CR(10,5) = -Mz_d*csl*gam;
CR(10,10) = -Mb_d*gam;
CR(10,11) = Mz_d*gam;
CR(11,2) = -Qlam*csl*gam;
CR(11,3) = Qz_d*gam*snl;
CR(11,5) = -Qz_d*csl*gam;
CR(11,10) = -Qb_d*gam;
CR(11,11) = Qz_d*gam;
CR(13,14) = 2*Ip;
CR(14,13) = -2*Ip;
```

```
KR(1,3) = -Hu*csl*gam*(V + v);
KR(1,5) = -Hu*gam*snl*(V + v);
KR(1,6) = Hb_d*gam;
KR(1,7) = Ht*Kp*gam;
KR(1,8) = -Hz_d*gam;
KR(1,14) = -Ht*gam;
KR(2,4) = Hu*gam*snl*(V + v);
KR(2,6) = -Ht*Kp*gam*snl;
KR(2,7) = Hb_d*gam*snl;
KR(2,9) = -Hz_d*gam*snl;
KR(2,10) = 2*Kp*Tt*csl*gam;
KR(2,12) = -2*Tt*csl*gam;
KR(2,13) = Ht*gam*snl;
KR(3,3) = -Hu*csl^2*gam*h*(V + v);
KR(3,5) = -Hu*csl*gam*h*snl*(V + v);
KR(3,6) = csl*gam*(Hb_d*h + (Ib*(vb^2 - 1))/gam);
KR(3,7) = Ht*Kp*csl*gam*h;
KR(3,8) = -Hz_d*csl*gam*h;
KR(3,10) = 2*Kp*Qt*gam*snl;
KR(3,12) = -2*Qt*gam*snl;
KR(3,14) = -Ht*csl*gam*h;
KR(4,4) = -Hu*gam*h*(V + v);
KR(4,6) = Ht*Kp*gam*h;
KR(4,7) = -gam*(Hb_d*h + (Ib*(vb^2 - 1))/gam);
KR(4,9) = Hz_d*gam*h;
KR(4,13) = -Ht*gam*h;
KR(5,3) = -Hu*csl*gam*h*snl*(V + v);
KR(5,5) = -Hu*gam*h*snl^2*(V + v);
KR(5,6) = gam*snl*(Hb_d*h + (Ib*(vb^2 - 1))/gam);
KR(5,7) = Ht*Kp*gam*h*snl;
KR(5,8) = -Hz_d*gam*h*snl;
KR(5,10) = -2*Kp*Qt*csl*gam;
KR(5,12) = 2*Qt*csl*gam;
KR(5,14) = -Ht*gam*h*snl;
```

```
KR(6,4) = -Mu*gam*(V + v);
KR(6,6) = Ib*(vb^2 - 1) + Kp*Mt*gam;
KR(6,7) = -Mb_d*gam;
KR(6,9) = Mz_d*gam;
KR(6,13) = -Mt*gam;
KR(7,3) = -Mu*csl*gam*(V + v);
KR(7,5) = -Mu*gam*snl*(V + v);
KR(7,6) = Mb_d*gam;
KR(7,7) = Ib*(vb^2 - 1) + Kp*Mt*gam;
KR(7,8) = -Mz_d*gam;
KR(7,14) = -Mt*gam;
KR(8,4) = -Qu*gam*(V + v);
KR(8,6) = Kp*Qt*gam;
KR(8,7) = -Qb_d*gam;
KR(8,8) = Iz*(vz^2 - 1);
KR(8,9) = Qz_d*gam;
KR(8,13) = -Qt*gam;
KR(9,3) = -Qu*csl*gam*(V + v);
KR(9,5) = -Qu*gam*snl*(V + v);
KR(9,6) = Qb_d*gam;
KR(9,7) = Kp*Qt*gam;
KR(9,8) = -Qz_d*gam;
KR(9,9) = Iz*(vz^2 - 1);
KR(9,14) = -Qt*gam;
KR(10,10) = Ib0*vb0^2 + Kp*Mt*gam;
KR(10,12) = -Mt*gam;
KR(11,10) = Kp*Qt*gam;
KR(11,11) = Iz0*vz0^2;
KR(11,12) = -Qt*gam;
KR(12,11) = M0*gam - btr - bpr;
KR(12,12) = Ip*(wt^2 + 1);
KR(13,8) = M0*gam - btr - bpr;
KR(13,13) = Ip*wt^2;
KR(14,9) = M0*gam - btr - bpr;
```

```
KR(14,14) = Ip*wt^2;
```

where

csl	=	$\cos\Lambda$
snl	=	$\sin\Lambda$
Mb	=	Mb^*
Sz	=	S_ζ^*
gam	=	γ
I0	=	I_0^*
Iz0al	=	$I_{\zeta_0\alpha}$
Sb0	=	S_{β_0}
Hu	=	H_μ
Hb_d	=	$H_{\beta*}$
Hz_d	=	$H_{\zeta*}$
Hlam	=	H_λ
Kp	=	kinematic pitch-flap coupling

and the remaining terms can be understood from the above examples.

The wing matrices $M_W = MW$, $C_W = CW$, and $K_W = KW$ are $10{\times}10$ matrices. The non-zero terms are listed below. Some of the parameters appearing in the listing are defined as follows:

```
MW(1,1) = (13*L*R^2*m)/35;
MW(1,3) = (7*L*R*S)/20;
MW(1,5) = -(11*L^2*R*m)/210;
MW(1,6) = (9*L*R^2*m)/70;
MW(1,8) = (3*L*R*S)/20;
MW(1,10) = (13*L^2*R*m)/420;
MW(2,2) = (13*L*R^2*m)/35;
MW(2,4) = (11*L^2*R*m)/210;
MW(2,7) = (9*L*R^2*m)/70;
MW(2,9) = -(13*L^2*R*m)/420;
MW(3,1) = (7*L*R*S)/20;
MW(3,3) = (I*L)/3;
MW(3,5) = -(L^2*S)/20;
MW(3,6) = (3*L*R*S)/20;
```

```
MW(3,8) = (I*L)/6;
MW(3,10) = (L^2*S)/30;
MW(4,2) = (11*L^2*R*m)/210;
MW(4,4) = (L^3*m)/105;
MW(4,7) = (13*L^2*R*m)/420;
MW(4,9) = -(L^3*m)/140;
MW(5,1) = -(11*L^2*R*m)/210;
MW(5,3) = -(L^2*S)/20;
MW(5,5) = (L^3*m)/105;
MW(5,6) = -(13*L^2*R*m)/420;
MW(5,8) = -(L^2*S)/30;
MW(5,10) = -(L^3*m)/140;
MW(6,1) = (9*L*R^2*m)/70;
MW(6,3) = (3*L*R*S)/20;
MW(6,5) = -(13*L^2*R*m)/420;
MW(6,6) = (13*L*R^2*m)/35;
MW(6,8) = (7*L*R*S)/20;
MW(6,10) = (11*L^2*R*m)/210;
MW(7,2) = (9*L*R^2*m)/70;
MW(7,4) = (13*L^2*R*m)/420;
MW(7,7) = (13*L*R^2*m)/35;
MW(7,9) = -(11*L^2*R*m)/210;
MW(8,1) = (3*L*R*S)/20;
MW(8,3) = (I*L)/6;
MW(8,5) = -(L^2*S)/30;
MW(8,6) = (7*L*R*S)/20;
MW(8,8) = (I*L)/3;
MW(8,10) = (L^2*S)/20;
MW(9,2) = -(13*L^2*R*m)/420;
MW(9,4) = -(L^3*m)/140;
MW(9,7) = -(11*L^2*R*m)/210;
MW(9,9) = (L^3*m)/105;
MW(10,1) = (13*L^2*R*m)/420;
MW(10,3) = (L^2*S)/30;
```

```
MW(10,5) = -(L^3*m)/140;
MW(10,6) = (11*L^2*R*m)/210;
MW(10,8) = (L^2*S)/20;
MW(10,10) = (L^3*m)/105;
CW(1,1) = sdamp_w + (L*R^2*a*q*(10*croot + 3*ctip))/(35*U);
CW(1,3) = (L*R*a*q*(112*croot*e + 35*ctip*e - 112*croot*wexd -
 35*ctip*wexd))/(420*U) -
  (L*R*a*q*(22*L*croot*snlw + 13*L*ctip*snlw))/(420*U*cslw);
CW(1,5) = -(L^2*R*a*q*(15*croot + 7*ctip))/(420*U);
CW(1,6) = (9*L*R^2*a*q*(croot + ctip))/(140*U);
CW(1,8) = (L*R*a*q*(35*croot*e + 28*ctip*e - 35*croot*wexd
- 28*ctip*wexd))/(420*U) - (L*R*a*q*(13*L*croot*snlw
 + 15*L*ctip*snlw))/(420*U*cslw);
CW(1,10) = (L^2*R*a*q*(7*croot + 6*ctip))/(420*U);
CW(2,2) = sdamp_v;
CW(3,1) = (L*R*a*q*(112*croot*e + 35*ctip*e -
 112*croot*wexd - 35*ctip*wexd))/(420*U) -
 (L*R*a*q*(22*L*croot*snlw + 13*L*ctip*snlw))/(420*U*cslw);
CW(3,3) = sdamp_phi + ((L*a*q*(L^2*croot*snlw^2 +
L^2*ctip*snlw^2))/60 - (L*a*cslw*q*(6*L*croot*e*snlw +
4*L*ctip*e*snlw - 6*L*croot*snlw*wexd -
 4*L*ctip*snlw*wexd))/60)/(U*cslw^2) + (L*a*q*(15*croot*e^2
 + 5*ctip*e^2 + 15*croot*wexd^2 + 5*ctip*wexd^2 - 30*croot*e*wexd
 - 10*ctip*e*wexd))/(60*U);
CW(3,5) = (L^2*a*q*(4*L*croot*snlw + 3*L*ctip*snlw))/(420*U*cslw)
 - (L^2*a*q*(14*croot*e + 7*ctip*e - 14*croot*wexd -
  7*ctip*wexd))/(420*U);
CW(3,6) = (L*R*a*q*(28*croot*e + 35*ctip*e - 28*croot*wexd
- 35*ctip*wexd))/(420*U) - (L*R*a*q*(13*L*croot*snlw +
22*L*ctip*snlw))/(420*U*cslw);
CW(3,8) = ((L*a*q*(L^2*croot*snlw^2 + 2*L^2*ctip*snlw^2))/60
 - (L*a*cslw*q*(4*L*croot*e*snlw + 6*L*ctip*e*snlw -
 4*L*croot*snlw*wexd - 6*L*ctip*snlw*wexd))/60)/(U*cslw^2)
  + (L*a*q*(5*croot*e^2 + 5*ctip*e^2 + 5*croot*wexd^2 +
```

```
     5*ctip*wexd^2 - 10*croot*e*wexd - 10*ctip*e*wexd))/(60*U);
CW(3,10) = (L^2*a*q*(7*croot*e + 7*ctip*e - 7*croot*wexd -
7*ctip*wexd))/(420*U) - (L^2*a*q*(3*L*croot*snlw +
4*L*ctip*snlw))/(420*U*cslw);
CW(5,1) = -(L^2*R*a*q*(15*croot + 7*ctip))/(420*U);
CW(5,3) = (L^2*a*q*(4*L*croot*snlw + 3*L*ctip*snlw))/(420*U*cslw)
- (L^2*a*q*(14*croot*e + 7*ctip*e - 14*croot*wexd - 7*ctip*wexd))/(420*U);
CW(5,5) = (L^3*a*q*(5*croot + 3*ctip))/(840*U);
CW(5,6) = -(L^2*R*a*q*(6*croot + 7*ctip))/(420*U);
CW(5,8) = (L^2*a*q*(3*L*croot*snlw + 4*L*ctip*snlw))/(420*U*cslw)
 - (L^2*a*q*(7*croot*e + 7*ctip*e - 7*croot*wexd -
 7*ctip*wexd))/(420*U);
CW(5,10) = -(L^3*a*q*(croot + ctip))/(280*U);
CW(6,1) = (9*L*R^2*a*q*(croot + ctip))/(140*U);
CW(6,3) = (L*R*a*q*(28*croot*e + 35*ctip*e - 28*croot*wexd
 - 35*ctip*wexd))/(420*U) - (L*R*a*q*(13*L*croot*snlw +
  22*L*ctip*snlw))/(420*U*cslw);
CW(6,5) = -(L^2*R*a*q*(6*croot + 7*ctip))/(420*U);
CW(6,6) = sdamp_w + (L*R^2*a*q*(3*croot + 10*ctip))/(35*U);
CW(6,8) = (L*R*a*q*(35*croot*e + 112*ctip*e - 35*croot*wexd
- 112*ctip*wexd))/(420*U) - (L*R*a*q*(22*L*croot*snlw +
90*L*ctip*snlw))/(420*U*cslw);
CW(6,10) = (L^2*R*a*q*(7*croot + 15*ctip))/(420*U);
CW(7,7) = sdamp_v;
CW(8,1) = (L*R*a*q*(35*croot*e + 28*ctip*e - 35*croot*wexd
 - 28*ctip*wexd))/(420*U) - (L*R*a*q*(13*L*croot*snlw +
 15*L*ctip*snlw))/(420*U*cslw);
CW(8,3) = ((L*a*q*(L^2*croot*snlw^2 + 2*L^2*ctip*snlw^2))/60
- (L*a*cslw*q*(4*L*croot*e*snlw + 6*L*ctip*e*snlw -
4*L*croot*snlw*wexd - 6*L*ctip*snlw*wexd))/60)/(U*cslw^2)
+ (L*a*q*(5*croot*e^2 + 5*ctip*e^2 + 5*croot*wexd^2
 + 5*ctip*wexd^2 - 10*croot*e*wexd - 10*ctip*e*wexd))/(60*U);
CW(8,5) = (L^2*a*q*(3*L*croot*snlw + 4*L*ctip*snlw))/(420*U*cslw)
- (L^2*a*q*(7*croot*e + 7*ctip*e - 7*croot*wexd -
```

```
 7*ctip*wexd))/(420*U);
CW(8,6) = (L*R*a*q*(35*croot*e + 112*ctip*e
- 35*croot*wexd - 112*ctip*wexd))/(420*U)
- (L*R*a*q*(22*L*croot*snlw + 90*L*ctip*snlw))/(420*U*cslw);
CW(8,8) = sdamp_phi + ((L*a*q*(2*L^2*croot*snlw^2
+ 10*L^2*ctip*snlw^2))/60 - (L*a*cslw*q*(6*L*croot*e*snlw
+ 24*L*ctip*e*snlw - 6*L*croot*snlw*wexd -
 24*L*ctip*snlw*wexd))/60)/(U*cslw^2) + (L*a*q*(5*croot*e^2 +
 15*ctip*e^2 + 5*croot*wexd^2 + 15*ctip*wexd^2 - 10*croot*e*wexd
  - 30*ctip*e*wexd))/(60*U);
CW(8,10) = (L^2*a*q*(7*croot*e + 14*ctip*e - 7*croot*wexd
- 14*ctip*wexd))/(420*U) - (L^2*a*q*(4*L*croot*snlw +
 10*L*ctip*snlw))/(420*U*cslw);
CW(10,1) = (L^2*R*a*q*(7*croot + 6*ctip))/(420*U);
CW(10,3) = (L^2*a*q*(7*croot*e + 7*ctip*e - 7*croot*wexd
 - 7*ctip*wexd))/(420*U) - (L^2*a*q*(3*L*croot*snlw +
  4*L*ctip*snlw))/(420*U*cslw);
CW(10,5) = -(L^3*a*q*(croot + ctip))/(280*U);
CW(10,6) = (L^2*R*a*q*(7*croot + 15*ctip))/(420*U);
CW(10,8) = (L^2*a*q*(7*croot*e + 14*ctip*e - 7*croot*wexd
- 14*ctip*wexd))/(420*U) - (L^2*a*q*(4*L*croot*snlw +
 10*L*ctip*snlw))/(420*U*cslw);
CW(10,10) = (L^3*a*q*(3*croot + 5*ctip))/(840*U);
KW(1,1) = (12*EIb*R^2)/L^3;
KW(1,3) = -(L*R*a*q*(16*croot + 5*ctip))/60;
KW(1,5) = -(6*EIb*R)/L^2;
KW(1,6) = -(12*EIb*R^2)/L^3;
KW(1,8) = -(L*R*a*q*(5*croot + 4*ctip))/60;
KW(1,10) = -(6*EIb*R)/L^2;
KW(2,2) = (12*EIc*R^2)/L^3;
KW(2,4) = (6*EIc*R)/L^2;
KW(2,7) = -(12*EIc*R^2)/L^3;
KW(2,9) = (6*EIc*R)/L^2;
KW(3,3) = GJ/L - (L*a*q*(15*croot*e + 5*ctip*e +
```

```
15*croot*wexd + 5*ctip*wexd))/60 -
(L*a*q*(3*L*croot*snlw + 2*L*ctip*snlw))/(60*cslw);
KW(3,4) = (epct*(EIc*GJ)^(1/2))/L;
KW(3,5) = -(epbt*(EIb*GJ)^(1/2))/L;
KW(3,8) = - GJ/L - (L*a*q*(5*croot*e + 5*ctip*e + 5*croot*wexd
+ 5*ctip*wexd))/60 - (L*a*q*(2*L*croot*snlw
+ 3*L*ctip*snlw))/(60*cslw);
KW(3,9) = -(epct*(EIc*GJ)^(1/2))/L;
KW(3,10) = (epbt*(EIb*GJ)^(1/2))/L;
KW(4,2) = (6*EIc*R)/L^2;
KW(4,3) = (epct*(EIc*GJ)^(1/2))/L;
KW(4,4) = (4*EIc)/L;
KW(4,7) = -(6*EIc*R)/L^2;
KW(4,8) = -(epct*(EIc*GJ)^(1/2))/L;
KW(4,9) = (2*EIc)/L;
KW(5,1) = -(6*EIb*R)/L^2;
KW(5,3) = (L^2*a*q*(2*croot + ctip))/60 -
 (epbt*(EIb*GJ)^(1/2))/L;
KW(5,5) = (4*EIb)/L;
KW(5,6) = (6*EIb*R)/L^2;
KW(5,8) = (epbt*(EIb*GJ)^(1/2))/L +
(L^2*a*q*(croot + ctip))/60;
KW(5,10) = (2*EIb)/L;
KW(6,1) = -(12*EIb*R^2)/L^3;
KW(6,3) = -(L*R*a*q*(4*croot + 5*ctip))/60;
KW(6,5) = (6*EIb*R)/L^2;
KW(6,6) = (12*EIb*R^2)/L^3;
KW(6,8) = -(L*R*a*q*(5*croot + 16*ctip))/60;
KW(6,10) = (6*EIb*R)/L^2;
KW(7,2) = -(12*EIc*R^2)/L^3;
KW(7,4) = -(6*EIc*R)/L^2;
KW(7,7) = (12*EIc*R^2)/L^3;
KW(7,9) = -(6*EIc*R)/L^2;
KW(8,3) = - GJ/L - (L*a*q*(5*croot*e + 5*ctip*e +
```

```
   5*croot*wexd + 5*ctip*wexd))/60 - (L*a*q*(2*L*croot*snlw +
   3*L*ctip*snlw))/(60*cslw);
KW(8,4) = -(epct*(EIc*GJ)^(1/2))/L;
KW(8,5) = (epbt*(EIb*GJ)^(1/2))/L;
KW(8,8) = GJ/L - (L*a*q*(5*croot*e + 15*ctip*e +
5*croot*wexd + 15*ctip*wexd))/60 -
(L*a*q*(3*L*croot*snlw + 12*L*ctip*snlw))/(60*cslw);
KW(8,9) = (epct*(EIc*GJ)^(1/2))/L;
KW(8,10) = -(epbt*(EIb*GJ)^(1/2))/L;
KW(9,2) = (6*EIc*R)/L^2;
KW(9,3) = -(epct*(EIc*GJ)^(1/2))/L;
KW(9,4) = (2*EIc)/L;
KW(9,7) = -(6*EIc*R)/L^2;
KW(9,8) = (epct*(EIc*GJ)^(1/2))/L;
KW(9,9) = (4*EIc)/L;
KW(10,1) = -(6*EIb*R)/L^2;
KW(10,3) = (epbt*(EIb*GJ)^(1/2))/L - (L^2*a*q*(croot + ctip))/60;
KW(10,5) = (2*EIb)/L;
KW(10,6) = (6*EIb*R)/L^2;
KW(10,8) = - (epbt*(EIb*GJ)^(1/2))/L - (L^2*a*q*(croot + 2*ctip))/60;
KW(10,10) = (4*EIb)/L;
```

where

EIb	=	EI_b
EIc	=	EI_c
epbt	=	ϵ_{bt}
epct	=	ϵ_{ct}
croot	=	root chord of element
ctip	=	tip chord of element
snlw	=	$\sin \Lambda$
cslw	=	$\cos \Lambda$
wexd	=	d_{ex}

and the remaining terms can be understood from the above examples.

References

[1] Hathaway, E. L., "Active and Passive Techniques for Tiltrotor Aeroelastic Stability Augmentation," Ph.D. Thesis, The Pennsylvania State University, 2005.

[2] Costa, G. J., "Design, Fabrication, Test, and Evaluation of Small-Scale Tiltrotor Whirl Flutter Wind Tunnel Models," Master's Thesis, The Pennsylvania State Unviersity, 2015.

[3] Gaffey, T., Yen, J., and Kvaternik, R., "Analysis and Model Tests of the Proprotor Dynamics of a Tilt-Proprotor VTOL Aircraft," Air Force V/STOL Technology and Planning Conference, Las Vegas, Nevada, 1969.

[4] Acree Jr, C., Peyran, R., and Johnson, W., "Rotor Design Options for Improving XV-15 Whirl-Flutter Stability Margins," NASA/TP-2004-212262, 2004.

[5] Popelka, D., Lindsay, D., Parham, T., Berry, V., and Baker, D. J., "Results of an Aeroelastic Tailoring Study for a Composite Tiltrotor Wing," *Journal of the American Helicopter Society*, Vol. 42, (2), 1997, pp. 126–136.

[6] Cole, J. A., Maughmer, M. D., and Bramesfeld, G., "Aerodynamic Design Considerations for Tiltrotor Wing Extensions and Winglets," Proceedings of the 51st AIAA Aerospace Sciences Meeting including the New Horizons Forum and Aerospace Exposition, AIAA 2013-1088, Grapevine, TX, 2013.

[7] Zhang, J. and Smith, E., "Influence of Aeroelastically Tailored Wing Extensions and Winglets on Whirl Flutter Stability," 2nd Asian/Australian Rotorcraft Forum and 4th International Basic Research Conference on Rotorcraft Technology, Tianjin, China, 2013.

[8] Ning, A. and Kroo, I., "Multidisciplinary Considerations in the Design of Wings and Wing Tip Devices," *Journal of Aircraft*, Vol. 47, (2), 2010, pp. 534–543.

[9] Taylor, E. and Browne, K. A., "Vibration Isolation of Aircraft Power Plants," *Journal of the Aeronautical Sciences*, Vol. 6, (2), 1938, pp. 43–49.

[10] Donham, R. and Watts, G., "Lessons Learned from Fixed and Rotary Wing Dynamic and Aeroelastic Encounters," 41st Structures, Structural Dynamics, and Materials Conference and Exhibit, Atlanta, GA, 2000.

[11] Houbolt, J. C. and Reed, W. H., III, "Propeller-Nacelle Whirl Flutter," Aeroelasticity Session, IAS 29th Annual Meeting, New York, 1961.

[12] Johnson, W., *Helicopter Theory*, Princeton University Press, Princeton, NJ, 1980, pp. 808–813.

[13] Hall, W. E., "Prop-Rotor Stability at High Advance Ratios," *Journal of the American Helicopter Society*, Vol. 11, (2), 1966, pp. 11–26.

[14] Edenborough, H. K., "Investigation of Tilt-Rotor VTOL Aircraft Rotorpylon Stability," *Journal of Aircraft*, Vol. 5, (2), 1968, pp. 97–105.

[15] Gaffey, T. M., "The Effect of Positive Pitch-flap Coupling (Negative $\delta 3$) on Rotor Blade Motion Stability and Flapping," *Journal of the American Helicopter Society*, Vol. 14, (2), 1969, pp. 49–67.

[16] Maisel, M. D., Giulianetti, D. J., and Dugan, D. C., "The History of the XV-15 Tilt Rotor Research Aircraft from Concept to Flight," NASA SP-2000-4517, January 2000.

[17] Johnson, W., "Analytical Model for Tilting Proprotor Aircraft Dynamics, Including Blade Torsion and Coupled Bending Modes, and Conversion Mode Operation," NASA-TM-X-62369, August 1974.

[18] Jonhson, W., "Analytical Modeling Requirements for Tilting Proprotor Aircraft Dynamics," NASA TN D-8013, July 1975.

[19] Johnson, W., "CAMRAD II Comprehensive Analytical Model of Rotorcraft Aerodynamics and Dynamics – Theory Manual," Johnson Aeronautics, Palo Alto, California, 1993.

[20] Nixon, M. W., "Aeroelastic Response and Stability of Tiltrotors with Elastically-Coupled Composite Rotor Blades," Ph.D. Thesis, The University of Maryland, 1994.

[21] Corso, L. M., Popelka, D. A., and Nixon, M. W., "Design, Analysis, and Test of a Composite Tailored Tiltrotor Wing," *Journal of the American Helicopter Society*, Vol. 45, (3), 2000, pp. 207–215.

[22] Piatak, D. J., Kvaternik, R. G., Nixon, M. W., Langston, C. W., Singleton, J. D., Bennett, R. L., and Brown, R. K., "A Wind-Tunnel Parametric Investigation of Tiltrotor Whirl-Flutter Stability Boundaries," The American Helicopter Society 57th Annual Forum, Washington, DC, 2001.

[23] Nixon, M. W., Langston, C. W., Singleton, J. D., Piatak, D. J., Kvaternik, R. G., Corso, L. M., and Brown, R. K., "Aeroelastic Stability of a Four-Bladed Semi-Articulated Soft-Inplane Tiltrotor Model," Proceedings of the 59th Annual AHS Forum, Phoenix, Arizona, 2003.

[24] Newman, J., Parham, T., Johnson, C., and Popelka, D., "Wind Tunnel Test Results for a 0.2 Scale 4-Bladed Tiltrotor Aeroelastic Model," 70th AHS Annual Forum, Montreal, Quebec, Canada, 2014.

[25] Rademacher, P. R., "Winglet Performance Evaluation Through the Vortex Lattice Method," Ph.D. Thesis, Embry-Riddle Aeronautical University, 2014.

[26] Whitcomb, R. T., "A Design Approach and Selected Wind Tunnel Results at High Subsonic Speeds for Wing-Tip Mounted Winglets," NASA TN D-8260, July 1976.

[27] Acree Jr, C., "Aerodynamic Limits on Large Civil Tiltrotor Sizing and Efficiency," Fifth Decennial AHS Aeromechanics Specialists' Conference, San Francisco, CA, San Francisco, CA, 2014.

[28] Farmer, M. G., "Preliminary Study of Effects of Winglets on Wing Flutter," NASA TM X-3433, December 1976.

[29] Ruhlin, C. L., Bhatia, K. G., and Nagaraja, K., "Effects of Winglet on Transonic Flutter Characteristics of a Cantilevered Twin-Engine-Transport Wing Model," NASA-TP-2627, 1986.

[30] Ruhlin, C. L., Rauch, F., and Waters, C., "Transonic Flutter Model Study of a Supercritical Wing and Winglet," *Journal of Aircraft*, Vol. 20, (8), 1983, pp. 711–716.

[31] Ricci, S., Castellani, M., and Romanelli, G., "Multi-Fidelity Design of Aeroelastic Wing Tip Devices," *Proceedings of the Institution of Mechanical Engineers, Part G: Journal of Aerospace Engineering*, 2012.

[32] Miller, S., Vio, G., Cooper, J., and Sensburg, O., "Optimisation of a Scaled Sensorcraft Model with Passive Gust Alleviation," Proceedings of the 12th AIAA/ISSMO Multidisciplinary Analysis and Optimization Conference, MAO, Victoria, BC, Canada, Vol. 1012, 2008.

[33] Paik, J., "The Aeroelastic Stability Improvements of Soft-Inplane Tiltrotors by Active and Passive Approaches," Ph.D. Thesis, The Pennsylvania State University, 2009.

[34] Clements, T. M. and Rais-Rohani, M., "Design Optimization of a Composite Tiltrotor Wing with Stability Approximations," Proc. of 41st AIAA/SME/ASEC/AHS/ASC Structures, Structural Dynamics and Materials Conference, Atlanta, GA, 2000.

[35] Soykasap, O. and Hodges, D. H., "Performance Enhancement of a Composite Tilt-Rotor using Aeroelastic Tailoring," *Journal of Aircraft*, Vol. 37, (5), 2000, pp. 850–858.

[36] Soykasap, O., "Inverse Method in Tiltrotor Optimization," *Aerospace Science and Technology*, Vol. 5, (7), 2001, pp. 437–444.

[37] Ozbay, S., Bauchau, O., Dancila, D. S., and Armanios, E. A., "Extension-Twist Coupling Optimization in Composite Rotor Blades," Proceedings of the 46th AIAA/ASME/ASCE/AHS/ASC Structures, Structural Dynamics and Materials Conference, 2005.

[38] Acree Jr, C. W., Yeo, H., and Sinsay, J. D., "Performance Optimization of the NASA Large Civil Tiltrotor," International Powered Lift Conference, London, UK, 2008.

[39] Acree Jr, C., "Integration of Rotor Aerodynamic Optimization with the Conceptual Design of a Large Civil Tiltrotor," AHS Aeromechanics Conference, San Francisco, CA, 2010.

[40] McCarthy, T. R. and Chattopadhyay, A., "A Coupled Rotor/Wing Optimization Procedure for High Speed Tilt-Rotor Aircraft," *Journal of the American Helicopter Society*, Vol. 41, (4), 1996, pp. 360–369.

[41] Chattopadhyay, A. and McCarthy, T. R., "An Integrated Optimum Design Approach for High Speed Prop Rotors," NASA-CR-199389, 1995.

[42] He, C. J. and Peters, D. A., "Optimum Rotor Interdisciplinary Design with a Finite State Aeroelastic System," *Mathematical and Computer Modelling*, Vol. 18, (3), 1993, pp. 37–51.

[43] Zhang, J. and Smith, E., "Parametric Studies of Wing Extensions and Winglets on Whirl Flutter Stability," Fifth Decennial AHS Aeromechanics Specialists Conference, San Francisco, CA, 2014.

[44] Johnson, S. C., "Design and Testing of a Small, Semi-span, Prop-rotor Model for Whirl Flutter Stability," Master's Thesis, The Pennsylvania State University, 2014.

[45] Hoover, T., "Tiltrotor Performance Improvements Through The Use Of Span Extensions And Winglets," Master's Thesis, The Pennsylvania State University, 2015.

[46] Acree Jr, C. and Johnson, W., "Aeroelastic Stability of the LCTR2 Civil Tiltrotor," AHS Technical Specialists Meeting, Dallas, Texas, October, 2008.

[47] Yang, C. and Xia, P., "Aeroelastic Stability of Wing/Pylon/Rotor Coupled System for Tiltrotor Aircraft in Forward Flight," *Science China Technological Sciences*, Vol. 54, (10), 2011, pp. 2708–2715.

[48] Conn, A., Gould, N., and Toint, P., "A Globally Convergent Lagrangian Barrier Algorithm for Optimization with General Inequality Constraints and Simple Bounds," *Mathematics of Computation of the American Mathematical Society*, Vol. 66, (217), 1997, pp. 261–288.

[49] "RCAS Theory Manual, Version 2.0," USAAMCOM/AFDD TR 02-A-005, 2002.

[50] Gibson, R. F., *Principles of Composite Material Mechanics*, CRC Press, 2011.

[51] Peyran, R. and Rand, O., "Effect of Design Requirements on Conceptual Tiltrotor Wing Weight," 55th AHS Annual Forum, Vol. 2, 1999.

[52] Zhang, J. and Smith, E., "Structural Design and Optimization of Composite Blades for a Low Weight Rotor," 2nd International Basic Research Conference on Rotorcraft Technology, Nanjing, China, 2005.

[53] Chandra, R. and Chopra, I., "Structural Behavior of Two-Cell Composite Rotor Blades with Elastic Couplings," *AIAA Journal*, Vol. 30, (12), 1992, pp. 2914–2921.

[54] Reddy, J. N., *Mechanics of Laminated Composite Plates and Shells: Theory and Analysis*, CRC press, 2004.

[55] Kunz, P. J., "Development of a Software Package for the Assessment of High-Performance Sailplanes," Master's Thesis, The Pennsylvania State University, 1997.

[56] Somers, D. M. and Martin, P. B., "Airfoils for a High-Efficiency Tiltrotor Aircraft," Airfoils Incorporated Report, June 2010.

[57] Eppler, R., "Airfoil Program System 'PROFIL07' User's Guide," Richard Eppler, c (2007).

[58] Drela, M., "Design and Optimization Method for Multi-Element Airfoils," AIAA Paper 93–0969, 1993.

[59] Torenbeek, E., *Synthesis of Subsonic Airplane Design*, Delft University Press, 1982.

[60] McCormick, B. W., *Aerodynamics, Aeronautics, and Flight Mechanics*, Vol. 2, Wiley New York, 1995.

[61] Leishman, J. G., *The Helicopter: Thinking Forward, Looking Back*, College Park Press College Park, MD, 2007.

[62] Theodore, C. R., Willink, G. C., Russell, C. R., Pete, A. E., and Amy, A. R., "Wind Tunnel Testing of a 6%-Scale Large Civil Tilt Rotor Model in Airplane and Helicopter Modes," AHS Fifth Decennial Aeromechanics Specialists' Conference, San Francisco, California, January 22-24, 2014.

[63] Chappel, D. P. and Peyran, R. J., "Methodology for Estimating Wing Weights for Conceptual Tilt-Rotor and Tilt-Wing Aircraft," 51st Annual Conference of Society of Allied Weight Engineers, Inc., Hartford, Connecticut, May 18-20 1992.

Sandilya Kambampati

CONTACT INFORMATION	229 Hammond Department of Aerospace Engineering The Pennsylvania State University University Park PA 16082 USA

Email: suk263@psu.edu
sandilya.kambampati@gmail.com
Phone: +1-848-565-5648

NATIONALITY   Indian

CAREER
OBJECTIVE
To establish myself as a competent researcher – in industry or academia – in engineering and applied mathematics

EDUCATION

The Pennsylvania State University

PhD Candidate in Aerospace Engineering (August 2013 – August 2016 (expected))

Master of Arts in Mathematics (May 2015 – August 2016 (expected))

Indian Institute of Science (IISc)

Master of Science in Aerospace Engineering, January 2013

Indian Institute of Technology (IIT) Kanpur

Bachelor of Technology in Aerospace Engineering, July 2010

JOURNAL
PUBLICATIONS

- **S. Kambampati**, R. Ganguli, "Nonrotating Beams Isospectral to Tapered Rotating Beams", *AIAA Journal*, (Accepted).
- **S. Kambampati**, R. Ganguli, " Non-Uniform Beams and Stiff Strings Isospectral to Axially Loaded Uniform Beams and Piano Strings", *Acta Mechanica*, 2014.
- **S. Kambampati**, R. Ganguli, V. Mani, "Rotating Beams Isospectral to Axially Loaded Non-Rotating Uniform Beams", *AIAA Journal,* 2013.
- **S. Kambampati**, R. Ganguli, V. Mani, "Determination of Isospectral Non-Uniform Rotating Beams", *ASME Journal of Applied Mechanics,* 2012.

RESEARCH PAPERS
IN PREPARATION

- **S. Kambampati**, and E. Smith, "Aeroelastic Optimization for High-Speed, High-Efficiency Tiltrotors with Winglets", (to be submitted to the AIAA Journal).
- **S. Kambampati**, T. Hoover, E. Smith, and M. Maughmer, "Multi-Disciplinary Optimization for High-Speed, High-Efficiency Tiltrotors with Wing Extensions and Winglets", (to be submitted to the AHS Journal).
- **S. Kambampati**, M. Potomkin, and L. Berlyand, "Applications of Rough Polyharmonic Splines to the p-Laplacian with Dirichlet Boundary Conditions", (in progress).